Observability-Based Guidance and Sensor Placement

Brian T. Hinson

A dissertation
submitted in partial fulfillment of the
requirements for the degree of

Doctor of Philosophy

University of Washington

2014

Reading Committee:

Kristi Morgansen Hill, Chair

Juris Vagners

Maryam Fazel Sarjoui

Brian C. Fabien

Program Authorized to Offer Degree:
Aeronautics and Astronautics

University of Washington

Abstract

Observability-Based Guidance and Sensor Placement

Brian T. Hinson

Chair of the Supervisory Committee:
Associate Professor Kristi Morgansen Hill
Aeronautics and Astronautics

Control system performance is highly dependent on the quality of sensor information available. In a growing number of applications, however, the control task must be accomplished with limited sensing capabilities. This thesis addresses these types of problems from a control-theoretic point-of-view, leveraging system nonlinearities to improve sensing performance. Using measures of observability as an information quality metric, guidance trajectories and sensor distributions are designed to improve the quality of sensor information. An observability-based sensor placement algorithm is developed to compute optimal sensor configurations for a general nonlinear system. The algorithm utilizes a simulation of the nonlinear system as the source of input data, and convex optimization provides a scalable solution method. The sensor placement algorithm is applied to a study of gyroscopic sensing in insect wings. The sensor placement algorithm reveals information-rich areas on flexible insect wings, and a comparison to biological data suggests that insect wings are capable of acting as gyroscopic sensors. An observability-based guidance framework is developed for robotic navigation with limited inertial sensing. Guidance trajectories and algorithms are developed for range-only and bearing-only navigation that improve navigation accuracy. Simulations and experiments with an underwater vehicle demonstrate that the observability measure allows tuning of the navigation uncertainty.

TABLE OF CONTENTS

LIST OF FIGURES

LIST OF TABLES

ACKNOWLEDGMENTS

This thesis represents four years of research that was influenced by countless individuals. I would like to acknowledge the guidance of my advisor, Kristi Morgansen, who shaped my ideas while allowing me freedom in my research endeavors. My supervisory committee provided useful comments throughout the research process that sparked new ideas and refined my results. In particular, Tom Daniel was an invaluable reference, as were his students Annika Eberle and Brad Dickerson.

I appreciate the camaraderie of my fellow labmates in the Nonlinear Dynamics and Controls Lab, who made my PhD an enjoyable and memorable learning experience. In particular, I want to thank Nathan Powel, Caleb Woodruff, Atiye Alaeddini, Jake Quenzer, Laszlo Techy, Natalie Brace, Josue Calderon, Cody Deacon, and Jared Becker for their numerous insightful conversations.

I also would like to acknowledge the National Science Foundation for the investment that they have made in my education.

I want to thank my parents, who instilled in me the drive to succeed and supported me in all my endeavors. Finally, I am indebted to my wife, Kimber, who supported me in uncountably many ways. Her love and support made this possible.

DEDICATION

to my wife, Kimberly Ann

Chapter 1

INTRODUCTION

The crux of many guidance, navigation, and control problems is the ability to estimate the state of the system (*e.g.*, position and velocity) from a time history of sensor measurements (*e.g.*, from a localization solution such as GPS). Observability analysis provides engineers with a tool to determine if the system states can be identified and to what degree each state can be observed. For linear systems, the observability analysis results are independent of the actuation provided to the system, thus if the system has poor observability characteristics, the only avenues for improvement are to modify the outputs (*i.e.*, add more sensors) or modify the dynamics (*i.e.*, redesign the system). For nonlinear systems, however, the sensing and actuation may be coupled, therefore the choice of input can directly impact the ability to observe system states. This coupling can be exploited in many cases to actively control the system to shape the observability characteristics.

One large area of research that utilizes this coupling is in the control of under-sensed systems — systems with insufficient sensors to directly measure the state of the system, but where active control can be used to recover additional sensory information. Simultaneous localization and mapping (SLAM), for example, requires active vehicle motion to track and observe landmarks [1, 2], and motion planning can be used to improve navigation quality [3, 4]. Underwater vehicle localization using a single ranging beacon also requires careful path planning to ensure observability [5, 6]. Mobile sensor networks and parameter identification fall into this category as well. Solutions to these problems all require vehicle motion to observe all system states, a process known as *active sensing*.

Active sensing appears not only in engineering problems, but is also found in the natural motions of many biological systems. One example of active sensing in biology is the halteres in flies [7]. The halteres are a pair of small organs evolved from hindwings. Similar to the forewings, the halteres beat during flight, which makes them sensitive to Coriolis forces and allow them to actively measure inertial rotations. These measurements would not be possible without the active beating. Active sensing is also observed in the vibrissa system (whiskers) in rodents [8, 9]. Rodents actively move their whiskers to detect objects in their environment through tactile sensing. The morphology of the rat vibrissa system allows for multiple spatial frequencies to be scanned in one motion, thus improving the resolution of sensing available through active motion. Yet another use of active sensing by biological systems is the active head motion in insects, birds, and mammals [10, 11]. Head saccades in birds and other animals have been shown to provide depth perception in animals without appreciable stereoscopic vision (*i.e.*, little or no overlap in the field of view of the eyes). These head motions are used solely to provide this extra sensory information. In fact, pigeons walking on treadmills have been observed to not use the head bobbing motion [12]. Active sensing can also be considered on a larger scale, where the path of the animal is chosen to achieve a sensory goal. Mosquitoes and other insects have been observed utilizing a "surge-and-cast" type maneuver to track plumes of carbon dioxide and odors [13]. This maneuver consists of surging upwind when a concentration of the gas or odor is detected, followed by casting back-and-forth crosswind to relocate the plume when the odor is lost. This problem is strongly related to the adaptive sampling problem in engineering, and heuristics based on the surge-and-cast behavior have been analyzed for engineered systems [14].

These four examples of active sensing in biology encompass problems where the sensory goals are independent of the control objectives. That is, the actuation utilized for improved sensing does not affect the locomotion of the animal (consider the pigeon on the treadmill, for example). Another interesting problem is when active sensing

is combined with the motion of the system. An example of this phenomenon is the abdomen in the hawkmoth *Manduca sexta*. The abdomen has been shown to support flight control as a pitch control mechanism [15], and strain sensing on the abdomen has been hypothesized to be used to estimate body rotations during periodic motions of the abdomen through Coriolis forces [16]. Therefore, the actuation used for sensing is also the actuation used to stabilize and control the pitch attitude of the animal. This inseparable coexistence of sensing and control is motivation for studying the coupling of sensing and control inherit in nonlinear systems. This thesis aims to answer questions about active sensing from an engineering perspective. How can active sensing motions be designed for engineered systems? How does the spatial distribution of sensors impact the ability to observe system behavior, as measured by the ability to accurately reconstruct the system state?

1.1 Literature Review

The active sensing observed in nature manifests itself in a wide range of engineering applications — from power grid monitoring to robotic navigation. These sensing problems are solved by fusing ideas from information theory, optimal control, systems theory, and combinatorial optimization. The array of applications can be classified into two problem types: static sensor placement and mobile sensor planning. In this section, the current state-of-the-art in these areas is discussed, and the open research problems are enumerated.

1.1.1 Static sensor placement

The static sensor placement problem considers where to place sensors to optimally observe a static or dynamic process. Applications are numerous in civil structure health monitoring [17, 18, 19], power grid monitoring [20, 21], environmental monitoring [22, 23], and robotic navigation [24, 25, 26]. The diversity of applications has driven solution approaches from several different angles.

One common metric for sensor placement optimality is the determinant of the Fisher information matrix (FIM). The FIM encodes the expected information available in a stochastic measurement. The utility of the FIM is revealed by the celebrated Cramér-Rao inequality, which gives a lower bound to the expected estimator variance [27]

$$P \equiv E\left\{(\hat{\mathbf{x}} - \mathbf{x})(\hat{\mathbf{x}} - \mathbf{x})^T\right\} \geq F^{-1}, \tag{1.1}$$

where P is the estimation covariance matrix, E is the expectation operator, $\mathbf{x}$ is the unknown state, $\hat{\mathbf{x}}$ is the state estimate, and F is the FIM. When equality in (1.1) is achieved, the estimator is said to be an efficient, unbiased estimator. In the case of an efficient estimator, the FIM is exactly the inverse of the estimation covariance, therefore, maximizing the determinant of F is equivalent to minimizing the determinant of P, which measures the volume of the estimation uncertainty ellipsoid. Other common information measures based on the FIM include the minimum eigenvalue (*i.e.*, the maximum estimation variance) and the trace of F^{-1} (*i.e.*, the average estimation variance).

The FIM measures also appear in the closely related field of optimal design of experiments [28], where regressor vectors (sensor locations) are chosen to optimize some metric of the regressor moment matrix. Regressors that optimize the determinant, minimum eigenvalue, or the average variance criteria are known in the optimal design of experiments literature as D-optimal, E-optimal, and A-optimal, respectively. D-, E-, and A-Optimal experiment designs for linear measurement models can be approximately solved using semidefinite programming [29]. For nonlinear measurement models, alternating convex optimization and sequential greedy searches have been employed to find optimal experiment designs [30].

One drawback of the FIM is that nonlinear process dynamics are difficult to incorporate. Because the calculation of the FIM requires an explicit model of the output probability distribution, only linear dynamics with Gaussian process noise are

amenable to the FIM framework. For this reason, many researchers have utilized the observability Gramian to measure sensor fitness. The observability Gramian is the deterministic analog to the FIM, measuring the relative observability of system modes. Early work on observability-based sensor placement used the observability Gramian for systems with linear dynamics [31, 32]. Nonlinear dynamics were incorporated into the sensor placement problem using the transient observability function (*i.e.*, the output energy) [31], and later, using the independence of measurement functions via the Gram determinant [33] as measures of observability. The advent of the empirical observability Gramian allowed numerical computation of the observability Gramian about a nominal trajectory of the nonlinear system [34, 35]. The empirical observability Gramian was first developed for balancing and model reduction in nonlinear systems [34, 35] and later adapted for observability analysis [36], measuring sensor fitness [37], and computing optimal sensor placement [38, 39].

One of the difficulties of the sensor placement problem is the combinatorial nature of the problem. In its most general form, the sensor placement problem can be written as a mixed integer nonlinear optimization problem, which consists of a nonlinear cost function (typically convex) in continuous and integer variables. The presence of the integer variables causes the problem to scale poorly to higher-dimensional problems (*e.g.*, large number of states or sensors). Several approaches have been taken to mediate the "curse of dimensionality" and allow solution of reasonably-sized problems. For small numbers of sensors, the optimal solution may be found by brute force by sampling each combination of sensors [33, 38, 40]. For more general problems, branch-and-bound techniques have been used with Lagrangian relaxation to prune portions of the search space that do not lead to an optimal solution [31]. Other approaches to carry out global optimization include successive linearization and relaxation of the mixed integer nonlinear program [39] or an iterative solution with exponential smoothing [24].

In all cases, the goal of the optimization procedure is to find the optimal (or

near-optimal) sensor set with reasonable computation time. Current state-of-the-art mixed integer programming solvers (such as CPLEX) can solve linear sensor placement problems with on the order of 10,000 sensor nodes in less than an hour [41]. However, "robust" sensor placement problems — maximizing the worst-case sensor performance or minimizing the covariance of sensor performance — require considerably more computational effort. Simulations in [42] demonstrated that the robust sensor placement problem could be solved for a system with about 400 sensor nodes in reasonable time (less than 10 minutes), but a system with approximately 3,000 sensor nodes could not be solved in less than a 24 hours. Conversely, a convex optimization approach developed in [43] can find near-optimal sensor sets for systems with on the order of 1,000 sensor nodes in a few seconds.

The current state-of-the art in sensor placement techniques requires improvement in three main areas. First, the most general observability-based sensor placement methods consider sensors that directly measure individual states [38, 39]. In many interesting applications, however, the measurement function may be some nonlinear function of the states. Second, problems involving heterogeneous sensor sets are not adequately addressed in the literature. Finally, more solution methods are needed to allow the sensor placement problem to scale to large systems.

1.1.2 Mobile sensor planning

The mobile sensor planning problem encompasses the largest area of research in optimal sensing. These problems can be thought of as an extension of the static sensor problem, where the sensors are allowed to move dynamically in time to optimally observe a spatially (and possibly temporally) varying process. A classic problem in this class is the target tracking problem, where a vehicle with either range or bearing measurements to a moving target is controlled to obtain an optimal estimate of the target's location and velocity. This problem has been studied with single [44] and multiple sensors [45, 46], as well as with varying fidelities of target motion mod-

els [47]. Similar to the static sensor scenario, most formulations of optimal target tracking utilize the FIM in the cost functional.

One subclass of mobile sensor problems that has received much attention is adaptive sampling using sensor networks. Adaptive sampling is a data-driven method that utilizes past measurements to actively decide where to sample next. One common problem formulation is the gradient climb (descent) problem, where vehicles detect the gradient of a scalar field and adaptively change heading to climb (descend) along the gradient to find a local maximum (minimum) [48]. For a single vehicle, estimating the local gradient requires some form of control excitation [49]. Other methods include minimizing uncertainty of a statistical model of the scalar field [50], minimizing the covariance of a particular estimation scheme [51], or maximizing the measurements of areas with high uncertainty [52]. Adaptive sampling has seen success in application to autonomous underwater vehicle (AUV) motion planning, where the AUV's mission is to actively sample the ocean environment. However, as is evidenced by the variety of approaches listed here, the appropriate metric for sampling is still an open question, and issues related to navigation and compensation for currents are yet to be effectively solved [50].

Information-based algorithmic approaches to the mobile sensor planning problem have recently grown in usage. These algorithms, under the name of *information gathering*, consider the spatial distribution of the quality of information as a scalar field that the vehicle must traverse to collect the most information under limited path length budget, where the measure of information is typically derived from the FIM. Generic, sampling-based algorithms have been successfully applied to the information gathering problem using rapidly-exploring random trees (RRT) [53, 54]. These algorithms can handle nonholonomic vehicle motion constraints and non-convex domain constraints using branch-and-bound techniques on trajectories generated from the RRT algorithm.

Another class of mobile sensor planning problems is planning sensor motion for

optimal online parameter estimation. Here, there is a fixed set of sensors, and the goal is to find control inputs that optimize the ability of the sensors to measure unknown parameters. This problem is often found in the literature of system identification, where "exciting" trajectories are desired to facilitate structured parameter identification [55]. The controls are chosen to minimize the condition number of the linear regressor matrix, which then optimally conditions a least-squares estimation of system parameters. This solution method has been successful in identification of robotic base parameters [55, 56], where the high-order (but linear in the parameters) dynamics demand specific trajectories to extract the desired parameters.

1.1.3 Robotic navigation

In all of the classes of mobile sensor planning problems listed here, the trajectory planning problem is solved to optimize a single objective — maximize a measure of information obtained by the mobile sensor. Thus, only sensory goals are considered. In the case of mobile robot motion planning, however, higher-level mission goals will likely need to be balanced with information quality. One particularly interesting example is motion planning for vehicles with limited navigation information (*e.g.*, range-only or bearing-only navigation), where vehicle motion is used not only to improve navigation information, but also to achieve higher-level mission objectives. Therefore, an algorithm is required that can balance the sensory goals with higher-level control objectives.

The range-only and bearing-only navigation problems have been studied in the literature from an observability perspective to derive informative trajectories — trajectories that improve navigation accuracy or uncertainty. In the context of single range-aided navigation, observability measures have been implemented to measure and improve estimation performance. An observability metric based upon the minimum singular value and condition number of the observability matrix were introduced in [57] to measure the relative observability of vehicle trajectories. Experimental re-

sults indicated that trajectory segments passing closer to the ranging beacon reduce estimation error. Another observability metric based upon linearization about a trajectory was presented by the author of this thesis in [58], and an optimization strategy showed that circular trajectories centered at the ranging beacon maximize vehicle position observability. This metric was then used in [59] to plan trajectories for a mobile navigation aid to maximize observability of an underwater vehicle using range-only localization. A numerical trajectory optimization technique was employed in [46] to coordinate multiple mobile sensors to track a single target using range measurements. The optimal heading to minimize covariance of an extended Kalman filter was found to be perpendicular to the bearing to the target.

Observability-based trajectory planning has also been applied to bearing-only navigation. In [44], the FIM was used in a cost function to derive observer maneuvers to optimally track a moving target. The first-order necessary conditions for a minimum to the proposed optimal control problem required the vehicle heading to be perpendicular to the target at the end of the optimization time horizon. The optimization problem was solved using direct numerical optimization to arrive at vehicle trajectories that minimize range uncertainty under bearing-only tracking. An observability measure based upon the determinant of the observability matrix was used in [60] to plan trajectories that optimize observability of time-to-contact with static obstacles in the environment. Simulation results showed that the observability-based path planning improved obstacle estimation and allowed the vehicle to navigate through obstacle fields.

Although observability-based path planning has been used to improve range-only and bearing-only navigation, some additional work is needed to make these guidance strategies viable for autonomous vehicle operation. The most in-depth analysis of these navigation problems comes from the target tracking community, where the only goal is to accurately track the target. However, in autonomous vehicle navigation, a framework is needed that can plan paths such that the vehicle can accomplish

some mission (*e.g.*, sensor coverage, search pattern, waypoint following) while maintaining sufficient navigation system performance. Sampling-based solution methods have shown promise for solving information-based path planning problems when non-convex path and environment constraints are imposed. In this work, however, a path planning solution is desired that can be implemented using a convex optimization framework with minimal computational requirements. By implementing a problem-specific path planner, better performance can be achieved compared to the more general sampling-based approaches.

1.2 Contributions of this Thesis

This thesis addresses the open problems discussed above and improves the state-of-the art in optimal active sensing through the following contributions:

- Development of an observability-based sensor placement procedure that incorporates nonlinear dynamics, nonlinear measurement models, and heterogeneous sensors.

- Convex optimization solution methods for the sensor placement problem that are scalable to large systems.

- Extension of the sensor placement problem to an observability-based sensor data compression algorithm.

- Application of the sensor placement procedure to discover sensor configurations for gyroscopic sensing in insect wings, with comparison to biological data.

- Observability-based optimal trajectory generation procedure for robotic navigation with limited sensors.

- Observability-based guidance algorithm for range-only and bearing-only navigation that allows balancing of sensing objectives and higher-level mission objectives.

- Experimental validation of the observability-based guidance algorithm.

1.3 Organization of the Report

The remainder of the report is organized as follows. Methods for observability analysis and measures of observability for nonlinear systems are discussed in Chapter 2. Formulation of the observability-based sensor placement problem and solution methods are provided in Chapter 3. In Chapter 4, the sensor placement procedure is applied to an example system representing the dynamics of flexible, flapping insect wings. The wing flapping dynamics are derived and the observability-based optimal sensor configuration is compared to biological data. observability-based guidance for robotic navigation with limited sensors is described in Chapters 5 and 6. In Chapter 5, analytical solutions to the observability-based guidance problem are derived for range-only navigation, bearing-only navigation, and navigation in currents. An observability-based guidance algorithm for range-only and bearing-only navigation is developed in Chapter 6 with experimental results demonstrating its effectiveness. Finally, a discussion of the results and directions for future work are described in Chapter 7.

Chapter 2

OBSERVABILITY MEASURES

In this chapter, a review of nonlinear observability is provided using differential geometric methods. Quantitative measures of observability are introduced that utilize the nonlinear observability matrix and the observability Gramian for linear time-varying systems. A connection between the nonlinear observability matrix, the observability Gramian, and estimation uncertainty is established, which motivates the use of observability as a measure of estimation performance.

2.1 Nonlinear Observability

Observability of nonlinear systems is analyzed following the work of Anguelova [61], which builds upon foundational works by Hermann and Krener [62] and Sontag and Wang [63], among others. The standard control-affine class of nonlinear systems is considered, which represents a wide array of physical systems. Specifically,

$$\begin{aligned} \dot{\mathbf{x}} &= \mathbf{f}_0(\mathbf{x}) + \sum_{i=1}^{m} \mathbf{f}_i(\mathbf{x}) u_i \\ \mathbf{y} &= \mathbf{h}(\mathbf{x}), \end{aligned} \tag{2.1}$$

where $\mathbf{x} \in \mathbb{R}^n$ are the states, $\mathbf{u} \in \mathbb{R}^m$ are the controls, $\mathbf{y} \in \mathbb{R}^p$ are the measurements, $\mathbf{f}_0(\mathbf{x}) \in \mathbb{R}^n$ is the drift vector field, and $\mathbf{f}_i(\mathbf{x}) \in \mathbb{R}^n$ $i \in \{1, \ldots, m\}$ are the control vector fields.

2.1.1 Observability rank condition

Observability is determined by considering the time derivatives of the system measurements. Define the Lie derivative operator as

$$L_{\mathbf{f}_i}\mathbf{h} = \left(\frac{\partial}{\partial \mathbf{x}}\mathbf{h}\right)\mathbf{f}_i(\mathbf{x}), \quad i \in \{0, \ldots, m\}, \tag{2.2}$$

with subsequent derivatives computed by

$$L_{\mathbf{f}_j}L_{\mathbf{f}_i}\mathbf{h} = \left(\frac{\partial}{\partial \mathbf{x}}L_{\mathbf{f}_i}\mathbf{h}\right)\mathbf{f}_j(\mathbf{x}), \quad i, j \in \{0, \ldots, m\}. \tag{2.3}$$

The time derivatives of the system measurements are composed of the Lie derivatives with respect to the drift and control vector fields. For example, the first time derivative of the output is given by

$$\frac{\mathrm{d}}{\mathrm{d}t}\mathbf{y} = \left(\frac{\partial}{\partial \mathbf{x}}\mathbf{h}(\mathbf{x})\right)\dot{\mathbf{x}} = L_{\mathbf{f}_0}\mathbf{h}(\mathbf{x}) + \sum_{i=1}^{m} L_{\mathbf{f}_i}\mathbf{h}(\mathbf{x})u_i. \tag{2.4}$$

For systems where $\mathbf{f}_i(\mathbf{x})$ and $\mathbf{h}(\mathbf{x})$ are analytic functions, the output derivatives are a polynomial function of the control input $\mathbf{u}$ and its time derivatives, with coefficients that are analytic functions of $\mathbf{x}$. In this case, the Lie derivatives form the observation space defined by

$$\mathcal{O} = \mathrm{span}\{L_{\mathbf{X}_1}\cdots L_{\mathbf{X}_k}\mathbf{h},\ k = 0, 1, \ldots n-1,\ \mathbf{X}_k \in \{\mathbf{f}_0, \ldots, \mathbf{f}_m\}\}, \tag{2.5}$$

where derivatives up to order $n-1$ are considered for analytic systems [61]. The Jacobian of the observation space gives the nonlinear observability matrix

$$\mathrm{d}\mathcal{O} = \left\{\frac{\partial}{\partial \mathbf{x}}\phi \;\middle|\; \phi \in \mathcal{O}\right\}, \tag{2.6}$$

which leads to a necessary and sufficient condition for local observability.

Definition 1 (Observability rank condition [62])**.** *The control affine system (2.1) is locally weakly observable if and only if it satisfies the observability rank condition*

$$\text{rank}(\text{d}\mathcal{O}(\mathbf{x})) = n. \tag{2.7}$$

The observability rank condition states that $\text{d}\mathcal{O}(\mathbf{x})$ must contain n independent covector fields. Because the system is analytic, the rank of $\text{d}\mathcal{O}$ is constant, except at singular points where the matrix drops rank [61]. The observability rank condition considers the *generic* rank of the matrix $\text{d}\mathcal{O}(\mathbf{x})$, which is the maximal rank over the manifold of admissible states. Therefore, if $\text{d}\mathcal{O}$ is full rank everywhere except at isolated singular points, the system is locally weakly observable.

The presence of the control vector fields in the observability space is counter-intuitive to what is known from observability of linear systems, where studying the uncontrolled system is sufficient to establish observability. In nonlinear systems, however, the sensing and actuation may be *coupled*, and the choice of control input can affect the system observability. If the observability matrix $\text{d}\mathcal{O}$ is full rank, but loses rank when the Lie derivatives with respect to the control vector field $\mathbf{f}_i(\mathbf{x})$ $i \in \{1, \ldots, m\}$ are removed, then actuation in the control input u_i is *required* for system observability. Therefore, in some cases excitation via control input may be necessary to observe all system states. The benefit of the observability rank condition is that it explicitly accounts for this coupling and provides information about what, if any, control actuation is required to obtain system observability. The drawback, however, is that the observability rank condition gives only a binary answer to the observability question, not a continuous measure of observability.

2.1.2 Relationship between nonlinear observability and estimation uncertainty

The observability matrix also has implications in the estimation problem. Consider the time derivatives of the output of (2.1) up to order $n-1$,

$$\mathbf{Y} = \begin{bmatrix} \mathbf{y} \\ \mathbf{y}^{(1)} \\ \vdots \\ \mathbf{y}^{(n-1)} \end{bmatrix} = \mathbf{g}(\mathbf{x}, \mathbf{u}, \ldots, \mathbf{u}^{(n-r-1)}), \tag{2.8}$$

where $\mathbf{u}^{(\cdot)}$ represents the derivative with respect to time, and r is the relative degree of system (2.1). The observability rank condition emerges from the implicit function theorem to prove existence of a unique inverse mapping $\mathbf{w}(\mathbf{Y})$ such that

$$\mathbf{g}(\mathbf{w}(\mathbf{Y}), \mathbf{u}, \ldots, \mathbf{u}^{(n-r-1)}) - \mathbf{Y} = 0 \tag{2.9}$$

for $\mathbf{Y}$ in some neighborhood of $\mathbf{g}(\mathbf{x}_0, \mathbf{u}, \cdots)$.

Computing a first-order Taylor series expansion of the output derivatives (2.8) gives a linear approximation to the input-output mapping,

$$\mathbf{Y} \approx \mathbf{g}(\mathbf{x}_0, \mathbf{u}_0) + \mathrm{d}\mathbf{Y}(\mathbf{x}_0)\Delta\mathbf{x}, \tag{2.10}$$

where $\mathbf{x}_0$ and $\mathbf{u}_0$ are the linearization point, and $\Delta\mathbf{x}$ is the deviation from the linearization. Assuming that the measurements $\mathbf{Y}$ are corrupted by zero mean Gaussian noise with covariance, R, an approximate solution for $\Delta\mathbf{x}$ can be obtained from a least-squares estimator [27]:

$$\Delta\mathbf{x} = \left(\mathrm{d}\mathbf{Y}^T R^{-1} \mathrm{d}\mathbf{Y}\right)^{-1} \mathrm{d}\mathbf{Y}^T R^{-1} \left(\mathbf{Y} - \mathbf{g}\right), \tag{2.11}$$

with covariance [27]

$$P = \left(\mathrm{d}\mathbf{Y}^T R^{-1} \mathrm{d}\mathbf{Y}\right)^{-1}. \tag{2.12}$$

For independent and identically distributed (i.i.d.) noise, $R = \sigma I$, and the covariance simplifies to $P = \sigma \left(\mathrm{d}\mathbf{Y}^T \mathrm{d}\mathbf{Y}\right)^{-1}$. Therefore, the covariance, P, is inversely proportional to the product $\mathrm{d}\mathbf{Y}^T \mathrm{d}\mathbf{Y}$. If the properties of $\mathrm{d}\mathbf{Y}$ can be manipulated, then the estimation covariance is manipulated as a result. As a note, the measurement Jacobian, $\mathrm{d}\mathbf{Y}$, is equivalent to the observability matrix, $\mathrm{d}\mathcal{O}$, evaluated at a nominal state, $\mathbf{x}_0$. Thus, the nonlinear observability matrix provides a connection to estimation uncertainty and can be used to select control and state trajectories to tune estimation performance.

2.1.3 Observability measures using the nonlinear observability matrix

The connection between the nonlinear observability matrix and estimation uncertainty for a least squares estimator motivates the use of the nonlinear observability matrix to compute measures of system observability. The singular values of the observability matrix (eigenvalues of $\mathrm{d}\mathbf{Y}^T \mathrm{d}\mathbf{Y}$) provide a good measure of observability due to their relation to the estimation covariance. The minimum singular value, $\sigma_{\min}(\mathrm{d}\mathbf{Y})$, gives a measure of the nearness to a singular matrix (unobservable system), which is inversely related to the maximum estimation covariance. The maximum singular value, $\sigma_{\max}(\mathrm{d}\mathbf{Y})$, measures the energy in the most observable mode, which is inversely related to the minimum estimation covariance. The condition number, $\kappa(\mathrm{d}\mathbf{Y}) = \sigma_{\max}(\mathrm{d}\mathbf{Y})/\sigma_{\min}(\mathrm{d}\mathbf{Y})$, measures the ratio of energy between the most observable mode and the least observable mode, which gives the shape of the estimation uncertainty ellipsoid. A large condition number produces an elongated uncertainty ellipsoid, while a condition number of unity produces uniform estimation uncertainty. The determinant of $\mathrm{d}\mathbf{Y}^T \mathrm{d}\mathbf{Y}$ gives the volume of the observation ellipsoid, $\mathcal{B} = \{\mathrm{d}\mathbf{Y}\mathbf{x} \mid \|\mathbf{x}\| \leq 1\}$ [29], which is inversely related to the volume of the estimation

Table 2.1: Singular value measures of the nonlinear observability matrix

measure	significance
$\sigma_{\min}^{-1}(\mathrm{d}\mathbf{Y})$	maximum estimation uncertainty
$\sigma_{\max}^{-1}(\mathrm{d}\mathbf{Y})$	minimum estimation uncertainty
$\kappa(\mathrm{d}\mathbf{Y})$	shape of estimation uncertainty ellipsoid
$\det\left[(\mathrm{d}\mathbf{Y}^T\mathrm{d}\mathbf{Y})^{-1}\right]$	volume of estimation uncertainty ellipsoid
$\mathrm{Tr}\left[(\mathrm{d}\mathbf{Y}^T\mathrm{d}\mathbf{Y})^{-1}\right]$	average estimation uncertainty

uncertainty ellipsoid. A summary of the singular value measures of observability is provided in Table 2.1.

2.1.4 Observability radius

Although the least squares estimate provides a nice connection between estimation uncertainty and the nonlinear observability matrix, the relationship considers a single step of a linearized estimator. In practice, an iterative or dynamic estimator (*e.g.*, nonlinear least squares) will provide a better estimate of the unknown state $\mathbf{x}$, but general relationships between observability and estimation uncertainty are difficult to establish for most iterative estimators. One interesting connection that can be drawn is the relationship between the observability matrix and the region of convergence of Newton's method. Using Kantorovitch's theorem and the inverse function theorem, a lower bound to the radius of the region of attraction of Newton's method can be computed using the methods of [64]. The radius of the region of attraction is denoted here as the *observability radius*, which is described in the following theorem.

Theorem 1 (Observability Radius)**.** *Let* $\mathrm{d}\mathbf{Y}_n(\mathbf{x})$ *be a set of* n *independent rows of* $\mathrm{d}\mathbf{Y}(\mathbf{x})$ *with corresponding continuously differentiable mapping* $\mathbf{g}_n : \mathbb{R}^n \to \mathbb{R}^n$ *that maps states to the* n *independent elements of* $\mathbf{Y}$*, denoted by* $\mathbf{Y}_n$*. Let* $\mathcal{B}_x \subset \mathbb{R}^n$ *be a ball of radius* $2R\|\mathrm{d}\mathbf{Y}_n^{-1}(\mathbf{x}_0)\|_F$ *centered at state* $\mathbf{x}_0$ *with corresponding output*

$\mathbf{Y}_0 = \mathbf{g}_n(\mathbf{x}_0)$. *If the matrix* $\mathrm{d}\mathbf{Y}_n(\mathbf{x})$ *satisfies the Lipschitz condition*

$$\|\mathrm{d}\mathbf{Y}_n(\mathbf{u}) - \mathrm{d}\mathbf{Y}_n(\mathbf{v})\|_F \leq M\|\mathbf{u} - \mathbf{v}\|_2 \quad \forall\ \mathbf{u}, \mathbf{v} \in \mathcal{B}_x \tag{2.13}$$

with Lipschitz constant M*, then there exists a ball* $\mathcal{B}_y \subset \mathbb{R}^n$ *centered at* $\mathbf{Y}_0$ *with radius*

$$R = \frac{1}{2M\|\mathrm{d}\mathbf{Y}_n^{-1}(\mathbf{x}_0)\|_F^2} \tag{2.14}$$

and a unique, continuously differentiable inverse mapping

$$\mathbf{w}_n : \mathcal{B}_y \to \mathcal{B}_x \tag{2.15}$$

such that

$$\mathbf{g}_n(\mathbf{w}_n(\mathbf{Y}_n)) = \mathbf{Y}_n \quad \textit{and} \quad \mathrm{d}\mathbf{w}_n(\mathbf{Y}_n) = \mathrm{d}\mathbf{g}_n(\mathbf{w}_n(\mathbf{Y}_n))^{-1}. \tag{2.16}$$

Proof. The proof follows directly from the inverse function theorem [64, Theorem 2.9.4]. □

The radius, R, defines the size of the ball, $\mathcal{B}_y$, in which the inverse mapping, $\mathbf{w}_n$, is guaranteed to exist. The corresponding set of states in the ball, $\mathcal{B}_x$, is the set of initial guesses that are guaranteed to converge to the unknown true state, $\mathbf{x}_0$, using Newton's method. Therefore, the radius of $\mathcal{B}_x$ is a measure of the tolerable uncertainty in the unknown state, $\mathbf{x}_0$ (*i.e.*, the estimation covariance). The radius of $\mathcal{B}_x$ is denoted the observability radius, given by

$$R_o = 2R\|\mathrm{d}\mathbf{Y}_n^{-1}(\mathbf{x}_0)\|_F = \frac{1}{M\|\mathrm{d}\mathbf{Y}_n^{-1}(\mathbf{x}_0)\|_F}, \tag{2.17}$$

where the Frobenius norm operator is defined for a square matrix, $A \in \mathbb{R}^{n\times n}$, by

$$\|A\|_F = \left(\sum_{i,j\leq n} A_{ij}^2\right)^{\frac{1}{2}}. \tag{2.18}$$

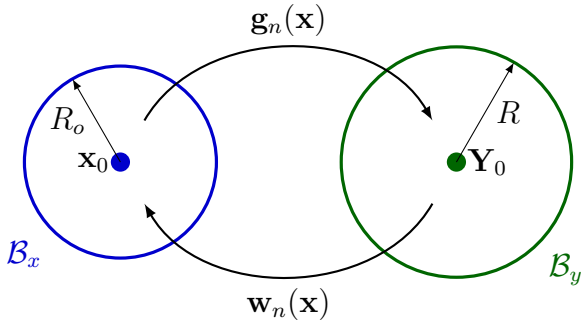

Figure 2.1: Depiction of the region of attraction of Newton's method. Initial guesses for the unknown state $\mathbf{x}_0$ that fall inside the ball $\mathcal{B}_x$ are guaranteed to converge to the true state $\mathbf{x}_0$ given the measurement vector $\mathbf{Y}_0$. The size of this ball is given by the observability radius R_o.

The relationship between these regions is depicted in Fig. 2.1.

One challenge in computing the observability radius is finding a suitable Lipschitz constant. For many nonlinear systems the observability matrix $\mathrm{d}\mathbf{Y}_n$ will likely be only *locally* Lipschitz, therefore the Lipschitz constant M will depend on the size of the ball $\mathcal{B}_x$ over which the Lipschitz condition must hold. If, however, the observability matrix is uniformly Lipschitz, then the observability radius serves as a measure of system observability as a function of the unknown state $\mathbf{x}_0$.

2.2 Observability Gramian

Another useful observability analysis tool is the observability Gramian for linear time-varying systems. The observability Gramian is constructed by linearizing the nonlinear dynamics (2.1) about a trajectory $(\mathbf{x}^0(t), \mathbf{u}^0(t))$ to obtain a linear time-varying system

$$\begin{aligned} \dot{\tilde{\mathbf{x}}}(t) &= A(\mathbf{x}^0(t), \mathbf{u}^0(t))\tilde{\mathbf{x}}(t) + B(\mathbf{x}^0(t))\tilde{\mathbf{u}}(t) \\ \tilde{\mathbf{z}}(t) &= C(\mathbf{x}^0(t))\tilde{\mathbf{x}}(t), \end{aligned} \tag{2.19}$$

where $\tilde{\mathbf{x}}(t) = \mathbf{x}(t) - \mathbf{x}^0(t)$ and $\tilde{\mathbf{u}}(t) = \mathbf{u}(t) - \mathbf{u}^0(t)$ are the deviations from the nominal trajectory and $\tilde{\mathbf{z}}(t)$ is the measurement deviation. The linearized dynamics matrices are computed using the Jacobian of the nonlinear dynamics,

$$\begin{aligned} A(\mathbf{x}^0(t), \mathbf{u}^0(t)) &= \frac{\partial}{\partial \mathbf{x}} \left[\mathbf{f}_0(\mathbf{x}) + \sum_{i=1}^{m} \mathbf{f}_i(\mathbf{x}) u_i \right] \Bigg|_{\mathbf{x}=\mathbf{x}^0, \mathbf{u}=\mathbf{u}^0} \\ B(\mathbf{x}^0(t)) &= \frac{\partial}{\partial \mathbf{u}} \left[\mathbf{f}_0(\mathbf{x}) + \sum_{i=1}^{m} \mathbf{f}_i(\mathbf{x}) u_i \right] \Bigg|_{\mathbf{x}=\mathbf{x}^0} \\ C(\mathbf{x}^0(t)) &= \frac{\partial}{\partial \mathbf{x}} \mathbf{h}(\mathbf{x}) \Big|_{\mathbf{x}=\mathbf{x}^0}, \end{aligned} \tag{2.20}$$

where it should be noted that for control affine systems, the input matrix, B, is not a function of the nominal control, $\mathbf{u}^0(t)$, because the dynamics are linear in the control variables. The input matrix is, however, an explicit function of the nominal state trajectory.

The observability of a linear time varying system is measured by the observability Gramian [65, ch. 6]:

$$W(t_0, t_f) = \int_{t_0}^{t_f} \Phi^T(t, t_0) C^T(\mathbf{x}^0(t)) C(\mathbf{x}^0(t)) \Phi(t, t_0) \mathrm{d}t, \tag{2.21}$$

where $\Phi(t, t_0) \in \mathbb{R}^{n \times n}$ is the state transition matrix defined by

$$\dot{\Phi}(t, t_0) = A(\mathbf{x}^0(t), \mathbf{u}^0(t)) \Phi(t, t_0). \tag{2.22}$$

If $W(t_0, t_f)$ is rank n for some t_f, then the linear time-varying system (2.19) is observable. Interestingly, the observability Gramian also provides information about the observability of the original nonlinear system (2.1). If the linear time-varying system is observable, then the nonlinear system (2.1) is locally observable about the nominal trajectory $(\mathbf{x}^0(t), \mathbf{u}^0(t))$ [37].

The observability Gramian thus provides an alternative to the nonlinear observability tools discussed in Section 2.1. Although the linear time-varying observability analysis considers the unactuated system (*i.e.*, the control deviation $\tilde{\mathbf{u}}$ is zero), the coupling between sensing and actuation is still explicitly considered through the choice of the linearization trajectory $(\mathbf{x}^0(t), \mathbf{u}^0(t))$. When choosing a nominal trajectory for analysis, care must be taken to utilize the control inputs that are required to excite the system dynamics. Insight gleaned from nonlinear observability analysis of the system provides these necessary control inputs (if any are required).

One disadvantage to the linearization approach is that the Gramian is difficult to compute analytically for a given nonlinear system and trajectory. Only for particularly simple nonlinear systems can the Gramian be computed in closed-form for an arbitrary linearization trajectory. For this reason, the Gramian is frequently computed numerically, which can be achieved using the empirical observability Gramian.

2.2.1 Empirical observability Gramian

The empirical observability Gramian provides a numerical procedure for approximating the linear time-varying observability Gramian (2.21) by simulating the nonlinear dynamics (2.1). The procedure for computing the Gramian from simulation output follows the development of [37]. The Gramian is computed by simulating the nonlinear system dynamics with perturbed initial conditions in each state and comparing the output time history for each perturbation. Each state initial condition is independently perturbed by $\pm\epsilon$ and simulated using the nominal input sequence $\mathbf{u}^0(t)$. Let $\mathbf{y}^{+i}$ be the simulation output with a positive perturbation in the initial condition for state x_i, and $\mathbf{y}^{-i}$ be the output with a negative perturbation in the initial condition for state x_i. Define the change in output $\Delta\mathbf{y}_i = \mathbf{y}^{+i} - \mathbf{y}^{-i}$, then the empirical

observability Gramian is calculated by

$$\tilde{W} = \frac{1}{4\epsilon^2} \int_{t_0}^{t_f} \begin{bmatrix} \Delta \mathbf{y}_1^T(t) \\ \vdots \\ \Delta \mathbf{y}_n^T(t) \end{bmatrix} \begin{bmatrix} \Delta \mathbf{y}_1(t) & \cdots & \Delta \mathbf{y}_n(t) \end{bmatrix} \mathrm{d}t. \tag{2.23}$$

Therefore, the Gramian can be computed by simulating the system $2n$ times. It can be shown that the empirical observability Gramian converges to the observability Gramian (2.21) in the limit $\epsilon \to 0$ [37]. In practice a value of ϵ on the order of 10^{-3} is sufficient to compute the empirical Gramian.

2.2.2 Relationship between the observability Gramian and estimation uncertainty

Like the nonlinear observability matrix, the observability Gramian is closely related to the estimation uncertainty and the FIM. For a discrete set of measurements in time, the output of the linear time-varying system (2.19) can be written as

$$\mathbf{Z} = \begin{bmatrix} \tilde{\mathbf{z}}(t_1) \\ \vdots \\ \tilde{\mathbf{z}}(t_N) \end{bmatrix} = \begin{bmatrix} C_1 \Phi_1 \\ \vdots \\ C_N \Phi_N \end{bmatrix} \mathbf{x}_0 = H \mathbf{x}_0, \tag{2.24}$$

where $C_k = C(\mathbf{x}^0(k\Delta t))$ and $\Phi_k = \Phi(t_0 + k\Delta t, t_0)$ are the discrete-time measurement and transition matrices, and $\mathbf{x}_0 = \mathbf{x}(t_0)$ is the state initial condition. Assuming again that the measurements are corrupted by zero-mean Gaussian noise with normal distribution $\mathcal{N}(0, R)$, and using a weighted least squares formulation, the minimum variance estimate is given by [27]

$$\hat{\mathbf{x}}_0^\star = (H^T R^{-1} H)^{-1} H^T R^{-1} \mathbf{Z}. \tag{2.25}$$

Computing the estimate covariance gives

$$P = E\left\{(\hat{\mathbf{x}}_0^\star - \mathbf{x}_0)(\hat{\mathbf{x}}_0^\star - \mathbf{x}_0)^T\right\} = \left(H^T R^{-1} H\right)^{-1}. \tag{2.26}$$

The least squares estimator is known to be efficient (*i.e.*, the Cramér-Rao lower bound is achieved) [27], therefore the FIM is exactly the inverse of the estimation covariance, $F = H^T R^{-1} H$. If the measurement noise variables are i.i.d., then $R = \sigma I$, where σ is the variance of each measurement, and the FIM simplifies to $F = \sigma^{-1} H^T H$. Expanding the FIM gives

$$H^T H = \sum_{k=1}^{N} \Phi_k^T C_k^T C_k \Phi_k = W_d(1, N), \tag{2.27}$$

which is the discrete-time observability Gramian. Therefore, the observability Gramian is proportional to the FIM in the case of i.i.d. measurements and inversely proportional to the estimate covariance. If the observability Gramian eigenvalues are manipulated (or even specified), then the estimation covariance is directly manipulated as a result.

2.2.3 Observability measures using the observability Gramian

Because the observability Gramian is closely related to the estimation uncertainty and the FIM, the eigenvalues of the observability Gramian directly control the Fisher information and inversely control the estimation covariance. The eigenvalues of the observability Gramian represent the relative observability of each system mode. The minimum eigenvalue, $\lambda_{\min}(W)$, is a measure of the output energy for the least observable mode, while the maximum eigenvalue is the measure of the output energy for the most observable mode,

$$\lambda_{\min}(W)\|\tilde{\mathbf{x}}(0)\| \leq \int_{t_0}^{t_f} \tilde{\mathbf{z}}^T \tilde{\mathbf{z}} \mathrm{d}t \leq \lambda_{\max}(W)\|\tilde{\mathbf{x}}(0)\|. \tag{2.28}$$

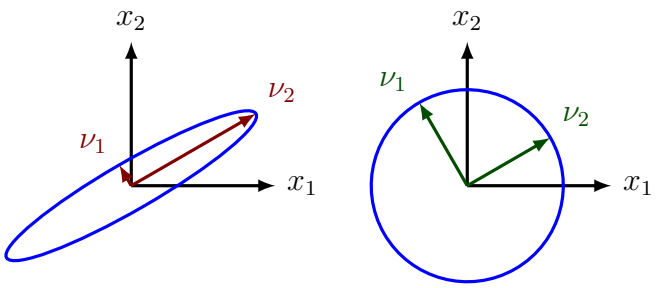

Figure 2.2: Output energy level sets for different observability condition numbers.

Table 2.2: Eigenvalue measures of the observability Gramian

measure	significance
$\lambda_{\min}^{-1}(W)$	maximum estimation uncertainty
$\lambda_{\max}^{-1}(W)$	minimum estimation uncertainty
$\kappa(W)$	shape of estimation uncertainty ellipsoid
$\det[W^{-1}]$	volume of estimation uncertainty ellipsoid
$\mathrm{Tr}[W^{-1}]$	average estimation uncertainty

The minimum eigenvalue is also the Euclidean distance to the set of singular matrices (*i.e.*, the distance to an unobservable system) [66].

The condition number, $\kappa(W) = \lambda_{\max}(W)/\lambda_{\min}(W)$, is another important property of the observability Gramian. The condition number can be visualized graphically by looking at the level sets of the output energy function, $\|\tilde{\mathbf{z}}(t)\|$. Fig. 2.2 shows ellipsoid level sets of the output energy for two example observability Gramians — one with a poorly-conditioned Gramian (left) and one with a well-conditioned Gramian (right). The radii of these ellipsoids are equal to the inverse of the eigenvalues of W. The eigenvector corresponding to the maximum eigenvalue, ν_1, is the direction with the largest gain (and thus most observable mode), therefore a small perturbation in that direction yields an output energy equivalent to that of a larger perturbation in the

direction of the eigenvector corresponding to the minimum eigenvalue, ν_2 (direction of the least observable mode). Because the condition number measures the ratio of maximum eigenvalue to minimum eigenvalue, an observability Gramian with a large condition number indicates that the output energy is dominated by some modes, while others are difficult to observe. A summary of the observability measures for the observability Gramian is provided in Table 2.2.

Chapter 3

OBSERVABILITY-BASED SENSOR PLACEMENT

Using the measures of observability introduced in Chapter 2, the first main contribution of this thesis is presented in this chapter — an observability-based sensor placement procedure. First, the sensor placement problem is formally defined in Section 3.1. Next, solution methods are proposed using convex optimization and mixed-integer programming in Section 3.2. Finally, the sensor compression problem is described as an extension to the sensor placement problem in Section 3.3.

3.1 Problem Statement

The observability-based sensor placement problem considers a nonlinear control affine system

$$\begin{aligned} \dot{\mathbf{x}} &= \mathbf{f}_0(\mathbf{x}) + \sum_{i=1}^{m} \mathbf{f}_i(\mathbf{x}) u_i \\ \mathbf{y}_i &= \mathbf{h}_i(\mathbf{x}, \mathbf{s}_i) \quad i = 1, \cdots, p, \end{aligned} \tag{3.1}$$

where $\mathbf{s}_i$ is the sensor location for sensor i with measurement model $\mathbf{h}_i(\mathbf{x}, \mathbf{s}_i)$. The sensor location $\mathbf{s}_i$ is constrained to a known finite set of feasible sensor locations $\mathbf{s}_i \in \mathcal{S}$. Similarly, the sensor model is constrained to a known set of models, $\mathbf{h}_i \in \mathcal{H}$, where $\mathcal{H}$ may contain a single element for homogeneous sensor placement, or multiple for heterogeneous sensors.

The goal of the sensor placement procedure is to choose sensor locations $\mathbf{s}_i$ to optimize a measure of observability (*c.f.*, Chapter 2). Because observability in nonlinear systems is inherently a local concept, observability-based sensor placement optimizes

system observability *locally* about a trajectory. Therefore, the nominal trajectory $(\mathbf{x}^0(t), \mathbf{u}^0(t))$ is assumed to be known, and the sensors are placed to optimize observability about the nominal trajectory. In terms of the observability Gramian, the observability-based sensor placement problem can be formally written as

$$\begin{aligned} \min_{\mathbf{s},\mathbf{h}} \quad & J[W(\mathbf{s},\mathbf{h})] \\ \text{subject to} \quad & \mathbf{s}_i \in \mathcal{S} \\ & \mathbf{h}_i \in \mathcal{H} \end{aligned} \tag{3.2}$$

where $J[\cdot]$ is a convex scalar measure of the observability Gramian (*e.g.*, condition number). The solution to the observability-based optimal sensor placement problem is a set of p sensor locations, $\mathbf{s}$, and sensor types, $\mathbf{h}$, that optimize system observability about the nominal trajectory. Because the observability measures are closely related to estimation uncertainty, optimally placed sensors will improved estimator performance.

3.2 Solution Methods

The observability-based sensor placement problem is developed in this section as a tractable optimization problem to solve for sensor locations and types. First, the nonlinear dynamics (3.1) are linearized about the nominal trajectory $(\mathbf{x}^0(t), \mathbf{u}^0(t))$ and converted to discrete time with N time steps of length Δt to obtain

$$\begin{aligned} A(k) &= \Phi(k\Delta t, 0) \\ C_i^j(k) &= C_i^j(\mathbf{x}^0(k\Delta t)) = \frac{\partial}{\partial \mathbf{x}} \mathbf{h}_j(\mathbf{x}, \mathbf{s}_i)\bigg|_{\mathbf{x}=\mathbf{x}^0(k\Delta t)} . \end{aligned} \tag{3.3}$$

The observability Gramian is constructed by noting that each sensor is *additive* to the Gramian (*i.e.*, the total Gramian is the sum of the Gramians for each sensor). Let the dimension of $\mathcal{S}$ be $n_s > p$ and the dimension of $\mathcal{H}$ be $n_h \geq 1$. Define the

sensor activation function $\beta_i^j \in \{0,1\}$, where $\beta_i^j = 1$ indicates that a sensor of type $\mathbf{h}_j$ is located at sensor location $\mathbf{s}_i$. Then the observability Gramian is written as

$$W(\beta) = \sum_{i \leq n_s, j \leq n_h} \beta_i^j \sum_{k=1}^{N} A(k)^T C_i^j(k)^T C_i^j(k) A(k) = \sum_{i \leq n_s, j \leq n_h} \beta_i^j W_i^j. \tag{3.4}$$

Alternatively, the observability Gramian for each sensor location/type combination, W_i^j, can be computed using the empirical observability Gramian, $\tilde{W}_i^j$. Therefore, the input data to the optimal sensor placement problem consist of the set of possible sensor locations $\mathcal{S}$, the set of sensor types $\mathcal{H}$, and a simulation that can be used to compute the empirical observability Gramian.

3.2.1 Mixed integer programming

The observability-based sensor placement problem can be posed as a mixed integer/convex optimization problem, which consists of convex objective and constraints, with integer constraints on a subset of the variables. All of the observability measures listed in Table 2.2 can be written as convex functions of W (concave measures such as $\lambda_{\min}$ are simply negated). Because composition with affine mappings preserves convexity, each measure is also a convex function of the sensor activation variable β_i^j [29]. Thus, the sensor placement problem can be written as a mixed-integer/convex problem

$$\begin{aligned} \min_{\beta} \quad & J[W(\beta)] \\ \text{subject to} \quad & \sum_{j=1}^{n_h} \beta_i^j \leq 1 \\ & \sum_{i=1}^{n_s} \sum_{j=1}^{n_h} \beta_i^j = p \\ & \beta_i^j \in \{0,1\} \end{aligned} \tag{3.5}$$

where the sum over j enforces that each sensor may only assume one type, and the sum over i and j enforces that p sensor locations must be selected.

Because mixed-integer programs scale exponentially in the number of binary variables, minimizing the number of binary variables in the problem formulation is of paramount importance. For n_s possible sensor locations and n_h sensor types, the number of binary variables is equal to $n_s n_h$. For most problems, n_h will be small. However, n_s may be large due to a large number of possible sensor locations. To reduce the number of sensor locations, a coarser discretization can be used while allowing the sensor location to be *continuous* and approximating the observability Gramian at any sensor location through linear interpolation between the discrete sensor nodes. In the case of homogeneous sensors (*i.e.*, $n_h = 1$), this piecewise linear approximation procedure is achieved through the use of special ordered sets of type two (SOS2, see [67, p. 177 - 182] and [52] for details). SOS2 are tools from mixed-integer programming that allow a vector of continuous variables to contain only two adjacent nonzero entries, with all other entries identically zero.

To illustrate how these tools can be used for piecewise linear approximation, consider approximating the function $f(x) = x^2$ with a piecewise linear function $g(x) = \sum w_i(x) f(x_i)$ as depicted in Fig. 3.1. Here, w_i are interpolation weights, which must contain only two adjacent nonzero entries for $g(x)$ to lie on the piecewise linear approximation to $f(x)$. Introducing $n-1$ binary variables δ_i, the SOS2 constraint is written as a series of linear inequalities

$$\begin{aligned} w_1 - \delta_1 &\leq 0 \\ w_2 - \delta_1 - \delta_2 &\leq 0 \\ &\vdots \\ w_{n-1} - \delta_{n-2} - \delta_{n-1} &\leq 0 \\ w_n - \delta_{n-1} &\leq 0, \end{aligned} \tag{3.6}$$

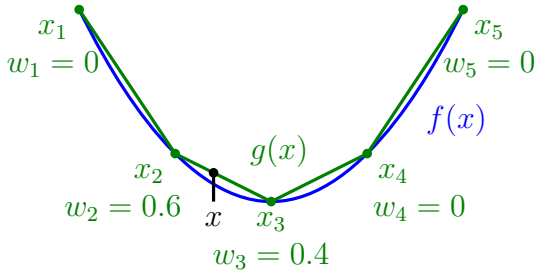

Figure 3.1: Example of piecewise linear approximation using special ordered sets of type two.

combined with the constraints $x = \sum w_i x_i$, $0 \leq w_i \leq 1$, and $\sum \delta_i = 1$. Thus, the sensor space discretization is made coarse, with piecewise linear interpolation used to approximate the Gramians between each sensor node. By examining the entries of the observability Gramians, the sensor discretization locations can be judiciously chosen so as to minimize the error introduced by the interpolation.

The piecewise linear interpolation is applied to the sensor placement problem by first sampling the observability Gramian at each of the n_i sensor interpolation nodes, denoted by W_i, $i \in 1, \ldots, n_i$. Define the vector of interpolation weights for each of p desired sensors as $\mathbf{w}^k \in \mathbb{R}^{n_i}$, $k \in 1, \ldots, p$. Then the interpolated observability Gramian is given by

$$\hat{W}(\mathbf{w}) = \sum_{i \leq n_i, k \leq p} \mathbf{w}_i^k W_i, \tag{3.7}$$

where $\mathbf{w}_i^k$ denotes the i^{th} element of the the $\mathbf{w}^k$ interpolation weight vector. Applying the piecewise linear interpolation to the mixed-integer program (3.5) gives

$$\begin{aligned} \min_{\mathbf{w}} \quad & J[\hat{W}(\mathbf{w})] \\ \text{subject to} \quad & \mathbf{w}^k \in \text{SOS2}, \end{aligned} \tag{3.8}$$

where $\mathbf{w}^k \in$ SOS2 indicates that the SOS2 constraints (3.6) are applied for the n_i

elements of each of the p interpolation weight vectors. The piecewise linear interpolation solution utilizes $(n_i - 1)p$ binary variables, compared to n_s binary variables for the original mixed-integer program. If the number of desired sensors p and number of interpolation nodes n_i are small compared to the size of the sensor space n_s, then piecewise linear interpolation allows fewer binary variables and faster solution times.

In an example application detailed in [68], the piecewise linear interpolation approach allowed the size of the sensor space to be reduced by more than 95%. The original problem contained on the order of 1,000 sensor nodes, which rendered the problem unsolvable in reasonable time (greater than 12 hours). However, application of the interpolation procedure allowed the sensor placement problem to be solved in less than a minute, while the error introduced in approximating the observability Gramian was less than 2%.

3.2.2 Convex relaxation

Because mixed-integer programming does not scale well to large problems, a convex relaxation to (3.5) provides a useful solution alternative. The binary constraint on the activation function is relaxed to the interval $[0, 1]$ to obtain the convex program,

$$\begin{aligned} \min_{\beta} \quad & J[W(\beta)] \\ \text{subject to} \quad & \sum_{j=1}^{n_h} \beta_i^j \leq 1 \\ & \sum_{i=1}^{n_s} \sum_{j=1}^{n_h} \beta_i^j = p \\ & 0 \leq \beta_i^j \leq 1. \end{aligned} \tag{3.9}$$

The advantage of the relaxation is that it can be solved in time that is polynomial in the number of variables $n_s n_h$ using efficient interior point methods [29]. Furthermore, if the solution to the relaxed problem is such that $\beta \in \{0, 1\}$ (within numerical toler-

ance), then the original mixed-integer problem has been solved. The relaxation serves two roles — an approximate (suboptimal) solution to the mixed-integer problem, and, in some cases, a fast optimal solution to the mixed-integer problem. In simulation studies, the convex relaxation could solve much larger problems (on the order of 1,000 sensor nodes) than the mixed integer programming approach [68].

3.2.3 ℓ_1-regularization

In both the mixed-integer problem (3.5) and the convex relaxation (3.9), the desired number of sensors was explicitly constrained to p. Another approach is to allow the number of sensors to be a free variable. In the sensor placement problem, a sparse solution is desired, where only a few of the sensor activation functions β_i^j are one, while the rest are zero. This solution property permits the construction of a convex relaxation of problem (3.5) that promotes a sparse solution using the ℓ_1 regularization technique (see, *e.g.*, [29, p. 304]). This approach is common in sparse sensing problems, where the binary constraint on β is relaxed to linear inequality constraints and a penalty on the ℓ_1-norm of β is added to the cost function to promote a sparse solution vector. Applying this relaxation to problem (3.5) yields a convex problem with ℓ_1 penalty,

$$\begin{aligned} \min_{\beta} \quad & J[W(\beta)] + c\|\beta\|_1 \\ \text{subject to} \quad & \sum_{j=1}^{n_h} \beta_i^j \leq 1 \\ & 0 \leq \beta_i^j \leq 1. \end{aligned} \tag{3.10}$$

where the constant $c \geq 0$ is the weighting on the ℓ_1-norm penalty. By varying the weight c, the number of sensors in the solution set will change to balance the sparsity penalty with the observability measure, tracing the Pareto tradeoff curve between sparsity and observability. The ℓ_1-regularization provides insight into how few sensors

can be used to achieve a particular level of observability.

Interestingly, the ℓ_1-regularization method frequently selects sensor locations very near the global optimal solution found by the mixed integer program. In simulation studies detailed in [68], the ℓ_1-regularization approach selected sensor locations near the optimal (within 1% of the length scale in the problem), but with less than a third of the required solution time. Similar to the convex relaxation, the ℓ_1-regularization problem can be solved in a few seconds for sensor spaces with on the order of 1,000 sensor nodes.

3.2.4 Exploiting submodularity in the sensor placement problem

Although the sensor placement problem is combinatorial in nature, some sensor placement objectives are *submodular* functions, which admit a simple greedy algorithm to find sensor sets that achieve suboptimality within a guaranteed bound. Submodular functions exhibit a diminishing returns feature that enable the success of greedy approximations, which is described in the following definition.

Definition 2 (Submodularity)**.** *Given a set Ω, a function $f : 2^{\Omega} \to \mathbb{R}$, is submodular if and only if*

$$f(X \cup \{x\}) - f(X) \geq f(Y \cup \{x\}) - f(Y)$$

for all subsets $X \subseteq Y \subseteq \Omega$ and $x \in \Omega \setminus Y$.

In essence, the submodular function increases more from the addition of a new set member when the current size of the set is smaller. In the context of the sensor placement problem, the set members are the sensor locations and types. The sensor placement problem can be placed in a set function framework as the following

Algorithm 1 Greedy Maximization of Submodular Functions

Require: sensor space, $\mathcal{S}$
Require: desired sensor count, p
  $X_0 \leftarrow \emptyset$
  $i \leftarrow 0$
  while $i < p$ **do**
    $X_{i+1} \leftarrow X_i \cup \left\{ \arg\max_x \left(f(X_i \cup x) - f(X_i) \mid x \in X_i \setminus \mathcal{S} \right) \right\}$
    $i \leftarrow i + 1$
  end while
  return X_p

optimization problem

$$\begin{aligned} \max_{X} \quad & f(X) \\ \text{subject to} \quad & X \subseteq \mathcal{S} \\ & |X| \leq p, \end{aligned} \tag{3.11}$$

where X is the set of selected sensors and $|X|$ gives the cardinality of the set of selected sensors. If the sensor placement objective, $f(X)$, is a submodular function, then the greedy algorithm described in Algorithm 1 can be used to compute a suboptimal sensor set. This algorithm was proven to result in an objective value with at least a factor of $1 - 1/e \approx 0.63$ of the optimal objective [69]. Therefore, the greedy algorithm achieves an objective that measures at least 63% of the optimal solution, and requires on the order of $p|\mathcal{S}|$ number of function evaluations. Thus, exploitation of submodularity allows very large problems to be approximately solved.

Several researchers have utilized submodularity to solve sensor placement problems. A review of a probabilistic framework for sensor placement is provided in [70], where the authors list several submodular objectives and constraints, including maximizing the "mutual information" of sensor locations (*i.e.*, maximizing the decrease in entropy of the state probability distribution). More recently, the submodularity of controllability and observability Gramian measures has been addressed for optimal

actuator and sensor placement [71]. The authors demonstrated that for a Gramian matrix, the functions $-\text{tr}(W^{-1})$, logdet(W), and rank(W) are submodular functions. The authors also proved by counter example that the minimum eigenvalue, $\lambda_{\min}(W)$, is not a submodular function. Therefore, if the observability-based sensor placement objective is to maximize $J(W) = -\text{tr}(W^{-1})$ (*i.e.*, minimize the average estimation uncertainty), or $J(W) = \text{logdet}(W)$ (*i.e.*, minimize the estimation uncertainty volume), or $J(W) = \text{rank}(W)$ (*i.e.*, maximize the number of observable states), then the greedy heuristic can be used to approximately solve the problem within a factor of 63% of optimal.

3.3 Sensor Data Compression

Frequently, the sensor placement problem is solved to find a sparse set of sensors that will provide the most information about a temporally and spatially varying process. In this sense, the goal of the sensor placement is to find a sensor configuration that provides the highest information density — the most information with the fewest sensors. The sensor placement procedure developed in Section 3.2 provides a solution for the spatial configuration of sensors that produces the highest information density, yielding the spatial positions where the most informative measurements can be made. The concept of information density is extended in this section to the *temporal* filtering of sensors.

The goal of temporal filtering is to optimally design a time-weighting of the sensor output $\mathbf{y}_i(t)$, thus revealing the temporal distribution of information in the sensor signal. The mechanics of the observability-based sensor placement procedure are easily adapted to solve for the sensor compression function. Consider the output of a sensor with known location and type, filtered by a scalar sensor compression function $\xi(t) \geq 0$

$$y_i(t) = \xi_i(t) h(\mathbf{x}). \tag{3.12}$$

Linearizing the measurement about the nominal trajectory $(\mathbf{x}^0(t), \mathbf{u}^0(t))$ and converting to discrete time gives the linear output matrix weighted by the sensor compression function

$$C_i(k) = \xi_i(k\Delta t)\frac{\partial}{\partial \mathbf{x}}h(\mathbf{x})\bigg|_{\mathbf{x}=\mathbf{x}^0(k\Delta t)}. \tag{3.13}$$

Therefore, the discrete time observability Gramian over the length of the trajectory is given by

$$W(\xi) = \sum_{i=1}^{p}\sum_{k=1}^{N}\xi_i^2(k)A(k)^T C_i(k)^T C_i(k)A(k), \tag{3.14}$$

which is a linear function of ξ_i^2. Alternatively, the output of the empirical observability Gramian can be used to compute the weighted Gramian via

$$W(\xi) = \frac{1}{4\epsilon^2}\sum_{i=1}^{p}\sum_{k=1}^{N}\xi_i^2(k)\begin{bmatrix}\Delta\mathbf{y}_1^T(k\Delta t)\\ \vdots \\ \Delta\mathbf{y}_n^T(k\Delta t)\end{bmatrix}\begin{bmatrix}\Delta\mathbf{y}_1(k\Delta t) & \cdots & \Delta\mathbf{y}_n(k\Delta t)\end{bmatrix}\Delta t. \tag{3.15}$$

Similar to the sensor placement problem, the sensor compression problem can be written as a convex optimization problem.

$$\begin{aligned}\min_{\tilde{\xi}} \quad & J\left[W\left(\tilde{\xi}^{1/2}\right)\right] \\ \text{subject to} \quad & \|\tilde{\xi}_i\|_1 \leq \delta \\ & \tilde{\xi}_i \geq 0,\end{aligned} \tag{3.16}$$

where $\tilde{\xi}_i = \xi_i^2$ and $J[\cdot]$ is any convex observability measure. As a note, $W(\tilde{\xi}^{1/2})$ is a linear function of $\tilde{\xi}$, which makes $J[W(\tilde{\xi}^{1/2})]$ a convex function of $\tilde{\xi}$. The non-negativity constraint on $\tilde{\xi}$ ensures that a feasible reconstruction of $\xi = \tilde{\xi}^{1/2}$ can be performed after the problem is solved. The norm constraint on $\tilde{\xi}$ limits the energy that can be added to the sensor signal to prevent an unbounded solution. The bound δ on

the norm is arbitrary and does not affect the shape of the solution for the compression function.

In the context of distributed sensing applications, the sensor compression function $\xi(t)$ represents sensor processing performed before the sensor data are sent back to a central location to be fused with data from other sensors. In many cases, the solution for the compression function will be sparse, thus minimizing the amount of data that is sent back to and processed by the central server. The solution provides not only a means for compressing the sensor data, but also insight into when and where the most informative bits of information occur in the process. In the context of biological systems, the sensor compression function represents neural filtering performed by individual sensors, which reduces the amount of information that must be processed by a central unit. Using only a simulation of a nonlinear system, the sensor compression function can be computed using the empirical observability Gramian as input data to the optimization problem (3.16).

Chapter 4

SENSOR PLACEMENT APPLICATION: GYROSCOPIC SENSING IN INSECT WINGS

The sensor placement procedure detailed in Chapter 3 can be applied to a wide range of engineering problems due to its generality — from positioning of navigation aids for planetary landing [72] to health monitoring of civil structures [17]. In this chapter, the optimal sensor placement procedure is used to characterize the gyroscopic sensing capabilities of the wings of the hawkmoth *Manduca sexta*. This application is relevant not only to the biological community, but also has important engineering implications. Because the hawkmoth demonstrates flight agility above the capabilities of modern engineered flight systems, insight gleaned from the hawkmoth sensory systems may be used to develop new design principles for biologically-inspired flight vehicles. This chapter begins with background information about the hawkmoth in Section 4.1. A low-order model of wing flapping dynamics is developed in Section 4.2, and details of the wing flapping simulation are provided in Section 4.3. The results of the observability-based sensor placement procedure are presented in Section 4.4 and a discussion of the results is provided in Section 4.5.

4.1 Background

The wings of hawkmoths contain mechanoreceptors, campaniform sensilla, that provide sensory information about wing deformation during flight [73]. Wing deformation arises from both aerodynamic loads and a variety of inertial forces, with the latter dominating [74]. An intriguing property of these sensory structures lies in their similarity to those found in halteres, the gyroscopic organ of flies. Halteres are known

to respond to Coriolis forces and are critically involved in flight control. They contain patches of campaniform sensilla that respond with incredible sensitivity to subtle loads and deflections. Importantly, halteres are evolutionarily derived from the insect wings, suggesting that wings themselves may serve a similar control function. Indeed, recent experimental results [73, 75] indicate that the campaniform sensilla embedded in the hawkmoth wing serve to detect inertial rotations. Like the halteres, the wings are actuated, flexible structures, and they deform in response to inertial rotations due to Coriolis forces. The deformations induce a spatial and temporal strain pattern on the wing that encodes the rotation rates. Thus, as suggested previously, the strain-sensitive campaniform sensilla may allow the wings to serve as gyroscopic organs in addition to their roles as actuators. Because the wing deforms in response to several stimuli — inertial-elastic loads due to normal flapping motion, aerodynamic loads, and other exogenous forces — the strain sensing must disambiguate these various influences to effectively act as a gyroscopic sensor. However, the ability to isolate strain patterns due to body rotations during typical flapping and aerodynamic loads has yet to be demonstrated.

Additionally, the role of sensillum strain directional sensitivity in detecting inertial rotations is not well-understood in wings. Experimental evidence has shown that the campaniform sensilla in *Drosophila* wings developed into two classes: one set tuned for slower excitation and another for faster excitation [76], which suggests that the sensitivity of campaniform sensilla may be heterogeneously distributed. Experiments on locust wings indicate that campaniform sensillum sensitivity to shear strain is important for detecting wing supination [77], though the details of how shear strain is locally encoded remains unclear. Early studies on campaniform sensilla on the legs of cockroaches demonstrated that the campaniform geometry may predict strain directional sensitivity. Oval-shaped campaniform sensilla were found in groups with aligned major axes [78], with the maximum sensory response corresponding to compression along the short axis of the oval [79]. To complement physiological char-

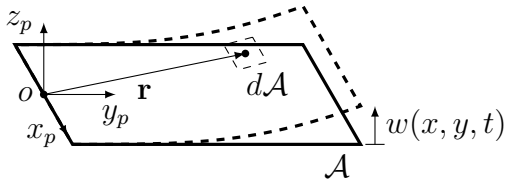

Figure 4.1: Free body diagram of a thin plate with out-of-plane bending in a rotating, accelerating reference frame.

acterization of wing campaniform sensilla, mathematical models are developed in this chapter that reveal sensor configurations that are theoretically best suited for gyroscopic sensing.

4.2 Flexible Wing Flapping Dynamics

In this section, a low-order model of flexible wing flapping dynamics is derived that is suitable for analysis and simulation. The model is developed by considering the motion of a thin, flexible plate in a rotating, accelerating reference frame. Using the finite element method and Lagrange's equations, the dynamics take the form of a set of second-order nonlinear ordinary differential equations. In the following subsections, the structural dynamics, kinematics, and aerodynamics models are derived, noting the assumptions that form the basis for the model.

4.2.1 Structural dynamics

The structural dynamics are derived using a plate model of the deformation and Lagrange's equations to incorporate inertial loads due to plate rotations and accelerations. The plate is assumed to deform out-of-plane with no in-plane stretching or extension. This section draws from the structural dynamics derivations in [80]. Expressions for the kinetic and potential energy of the plate system are developed by considering the free body diagram shown in Fig. 4.1.

The solution for the motion of the plate $w(x, y, t)$ is desired when the plate is subjected to flapping motion through rotations and accelerations of the root (edge along x_p axis). The infinite-dimensional governing partial differential equation is reduced into a finite-dimensional ordinary differential equation in time by allowing the plate to have a finite number of spatial degrees of freedom. The deformation of the plate will be described by a finite number of orthonormal spatial modes with mode shapes $\phi_i(x, y)$ and modal coordinates $\eta_i(t)$. The out-of-plane plate deformation is thus approximated by the relationship

$$w(x, y, t) = \sum_{i=1}^{n} \phi_i(x, y)\eta_i(t), \tag{4.1}$$

where n is the number of modes chosen to represent the spatial deformation. These modes will be derived from a finite element model representing the wing structure.

Using these mode shape functions and modal degrees of freedom, the position of a mass element on the plate in the plate reference frame is described by

$$\mathbf{r}(x, y, t) = x\hat{\mathbf{i}}_p + y\hat{\mathbf{j}}_p + w(x, y, t)\hat{\mathbf{k}}_p. \tag{4.2}$$

Taking the total derivative, the velocity of the point mass is (dropping the (x, y, t) notation for compactness)

$$\begin{aligned} \mathbf{v} &= \mathbf{v}_o + \frac{\partial}{\partial \mathrm{t}}\mathbf{r} + \omega_o \times \mathbf{r} \\ &= (U + Qw - Ry)\hat{\mathbf{i}}_p + (V + Rx - Pw)\hat{\mathbf{j}}_p + (W + \dot{w} + Py - Qx)\hat{\mathbf{k}}_p \end{aligned} \tag{4.3}$$

where $\mathbf{v}_o(t) = U(t)\hat{\mathbf{i}}_p + V(t)\hat{\mathbf{j}}_p + W(t)\hat{\mathbf{k}}_p$ is the velocity of the plate coordinate system origin, and $\omega_o(t) = P(t)\hat{\mathbf{i}}_p + Q(t)\hat{\mathbf{j}}_p + R(t)\hat{\mathbf{k}}_p$ is the angular velocity of the plate coordinate system. Let the mass density of the plate be given by $\rho(x, y)$ and the thickness by $h(x, y)$, then the kinetic energy of the plate can be found by integrating

over the area of the plate $\mathcal{A}$,

$$T_e(t) = \frac{1}{2} \int_{\mathcal{A}} \rho(x,y) h(x,y) \mathbf{v}(x,y,t) \cdot \mathbf{v}(x,y,t) \mathrm{d}\mathcal{A}. \tag{4.4}$$

To compute the potential energy of the plate, define the strain vector as

$$\chi = \begin{bmatrix} \partial^2 w/\partial x^2 \\ \partial^2 w/\partial y^2 \\ 2\partial^2 w/\partial x \partial y \end{bmatrix}, \tag{4.5}$$

and the matrix of material constants, D, which gives the potential energy ([80] p. 35)

$$U_e(t) = \frac{1}{2} \int_{\mathcal{A}} \frac{h(x,y)^3}{12} \chi(x,y,t)^T D \chi(x,y,t) \mathrm{d}\mathcal{A}. \tag{4.6}$$

The generalized coordinates describing the structural configuration are the modal coordinates η. Lagrange's equations are applied to the expressions for kinetic and potential energy via

$$\frac{\mathrm{d}}{\mathrm{d}t}\left(\frac{\partial T_e}{\partial \dot{\eta}_i}\right) - \frac{\partial T_e}{\partial \eta_i} + \frac{\partial U_e}{\partial \eta_i} = Q_i, \quad i = 1, \ldots, n, \tag{4.7}$$

where Q_i are the exogenous non-conservative generalized forces.

Substituting the assumed modal form of the displacement w (4.1) into the expressions for kinetic energy T_e (4.4), the first term of Lagrange's equations is

$$\begin{aligned} \frac{\mathrm{d}}{\mathrm{d}t}\left(\frac{\partial T_e}{\partial \dot{\eta}_i}\right) &= \frac{\mathrm{d}}{\mathrm{d}t} \int_{\mathcal{A}} \rho h \phi_i \left(W + Py - Qx + \sum_{j=1}^{n} \phi_j \dot{\eta}_j \right) \mathrm{d}\mathcal{A} \\ &= \int_{\mathcal{A}} \rho h \phi_i \left(\dot{W} + \dot{P}y - \dot{Q}x + \sum_{j=1}^{n} \phi_j \ddot{\eta}_j \right) \mathrm{d}\mathcal{A}. \end{aligned} \tag{4.8}$$

Because the mode shapes are assumed to be orthonormal, the integral of the product

of two modes, $\phi_i(x,y)\phi_j(x,y)$, is unity for $i=j$ and zero otherwise. The remaining terms can be organized into a mass matrix multiplying the applied accelerations:

$$\frac{\mathrm{d}}{\mathrm{d}t}\left(\frac{\partial T_e}{\partial \dot{\eta}}\right) = \ddot{\eta} + M_a \begin{bmatrix} \dot{W} \\ \dot{P} \\ \dot{Q} \end{bmatrix}, \tag{4.9}$$

where the i^{th} row of the applied acceleration mass matrix M_a is

$$M_{a_i} = \int_{\mathcal{A}} \begin{bmatrix} \rho h \phi_i & \rho h \phi_i y & -\rho h \phi_i x \end{bmatrix} \mathrm{d}\mathcal{A}. \tag{4.10}$$

The second term of Lagrange's equations includes centripetal and Coriolis terms:

$$\begin{aligned} \frac{\partial T_e}{\partial \eta_i} &= \int_{\mathcal{A}} \rho h \phi_i \left[Q\left(U - Ry\right) - P\left(V + Rx\right) + \left(Q^2 + P^2\right) \sum_{j=1}^{n} \phi_j \eta_j \right] \mathrm{d}\mathcal{A} \\ \Rightarrow \frac{\partial T_e}{\partial \eta} &= (Q^2 + P^2)\eta + M_a \mathbf{C}_a(\mathbf{v}_o, \omega_o), \end{aligned} \tag{4.11}$$

where the Coriolis force $\mathbf{C}_a$ is

$$\mathbf{C}_a(\mathbf{v}_o, \omega_o) = \begin{bmatrix} QU - PV \\ -QR \\ PR \end{bmatrix}. \tag{4.12}$$

The final term in Lagrange's equations is the stiffness term due to strain energy. This final term can be computed by assembling the expression for χ in terms of the generalized coordinates

$$\chi = \sum_{j=1}^{n} \begin{bmatrix} (\partial^2 \phi_j / \partial x^2) \\ (\partial^2 \phi_j / \partial y^2) \\ (\partial^2 \phi_j / \partial x \partial y) \end{bmatrix} \eta_j. \tag{4.13}$$

Substituting χ into the expression for potential energy U_e (4.6) yields the third term

in Lagrange's equations,

$$\frac{\partial U_e}{\partial \eta_i} = \int_{\mathcal{A}} \frac{h^3}{12} (\partial \chi / \partial \eta_i)^T D \chi \mathrm{d}\mathcal{A}. \tag{4.14}$$

By definition, the orthonormal free-vibration modes satisfy the homogeneous differential equation

$$\ddot{\eta} + \Omega \eta = 0, \tag{4.15}$$

where Ω is the diagonal modal frequency matrix with entries defined by

$$\Omega_{ij} = \int_{\mathcal{A}} \frac{h^3}{12} \begin{bmatrix} \partial^2 \phi_i / \partial x^2 \\ \partial^2 \phi_i / \partial y^2 \\ \partial^2 \phi_i / \partial x \partial y \end{bmatrix}^T D \begin{bmatrix} \partial^2 \phi_j / \partial x^2 \\ \partial^2 \phi_j / \partial y^2 \\ \partial^2 \phi_j / \partial x \partial y \end{bmatrix} \mathrm{d}\mathcal{A}, \tag{4.16}$$

with $\Omega_{ij} = \omega_i^2$ for $i = j$ and $\Omega_{ij} = 0$ for $i \neq j$. Thus, the final term in Lagrange's equations reduces to a diagonal mode frequency matrix multiplying the modal generalized coordinates,

$$\frac{\partial U_e}{\partial \eta} = \Omega \eta. \tag{4.17}$$

Finally, assembling the equations of motion for the flexible plate in a rotating, accelerating reference frame yields

$$\ddot{\eta} + (\Omega - \underbrace{(Q^2 + P^2)}_{\text{centripetal}})\eta + M_a \underbrace{\left(\begin{bmatrix} \dot{W} \\ \dot{P} \\ \dot{Q} \end{bmatrix} - \mathbf{C}_a(\mathbf{v}_o, \omega_o) \right)}_{\text{acceleration + Coriolis}} = \mathbf{Q}. \tag{4.18}$$

These equations of motion contain terms familiar to structural dynamics problems with some additional terms due to the inertial loads. The effective stiffness is reduced by the centripetal forces acting on the rotating plate. This behavior is intuitive

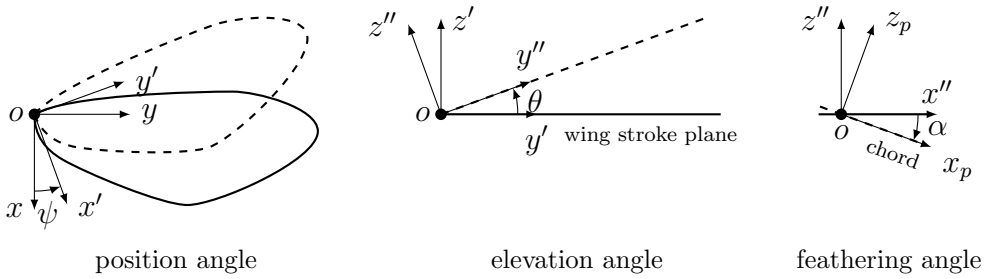

Figure 4.2: Wing coordinate system showing the positional angle ψ, feathering angle α, and elevation angle θ that control the wing stroke kinematics.

because large pitch or roll angular velocities will tend to drive large out-of-plane deflections. Additionally, the inertial loads due to applied accelerations and Coriolis forces appear explicitly through the M_a and $\mathbf{C}_a$ terms.

4.2.2 Wing stroke kinematics

The wing stroke kinematics define the applied motion of the wing. Nomenclature similar to [81] is used to define the three angles that parameterize the wing kinematics — the positional angle ψ, the feathering angle α, and the elevation angle θ. The positional angle parameterizes the position in the stroke sequence, where negative ψ indicates that the wing tip is posterior to the root, and positive ψ positions the wing tip anterior to the root. The feathering angle controls the wing section pitch relative to the wing stroke plane, where positive α yields inclination with the leading edge above the trailing edge. The elevation angle controls the wing elevation relative to the wing stroke plane, where positive θ yields a wing tip position above the wing stroke plane. These three angles control the orientation of the wing coordinate system, as depicted in Fig. 4.2.

The kinematic equations relate the applied wing rotation rates (P, Q, R) to the orientation of the wing reference frame $(\hat{\mathbf{i}}_p, \hat{\mathbf{j}}_p, \hat{\mathbf{k}}_p)$ relative to the inertial frame. The

orientation of the wing reference frame is represented via the three Euler angles (ψ, θ, and α) and a 3-1-2 rotation sequence (*i.e.*, rotate about the 3-axis, then the 2-axis, then the 1-axis [82]). First, the inertial frame is rotated about the 3-axis by the positional angle ψ

$$R_3(\phi) = \begin{bmatrix} \cos\psi & \sin\psi & 0 \\ -\sin\psi & \cos\psi & 0 \\ 0 & 0 & 1 \end{bmatrix}. \tag{4.19}$$

Next, the resulting frame is rotated about the 1-axis by the elevation angle θ

$$R_1(\theta) = \begin{bmatrix} 1 & 0 & 0 \\ 0 & \cos\theta & \sin\theta \\ 0 & -\sin\theta & \cos\theta \end{bmatrix}. \tag{4.20}$$

Finally, the resulting frame is rotated about the 2-axis by the feathering angle α

$$R_2(\alpha) = \begin{bmatrix} \cos\alpha & 0 & -\sin\alpha \\ 0 & 1 & 0 \\ \sin\alpha & 0 & \cos\alpha \end{bmatrix}. \tag{4.21}$$

Combining all the rotations yields the rotation matrix from inertial frame to wing frame

$$R(\psi, \theta, \alpha) = R_2(\alpha)R_1(\theta)R_3(\psi). \tag{4.22}$$

The kinematic equations that relate the Euler angle rates to the wing-fixed angular velocities are derived by successively rotating the Euler angle rates into the wing-fixed axis system. Let the Euler angles be represented by a vector $\mathbf{u} = \begin{bmatrix} \theta & \alpha & \psi \end{bmatrix}^T$, let the wing axis angular rates be represented by $\omega_o = \begin{bmatrix} P & Q & R \end{bmatrix}^T$. Defining the unit

vectors in each axis direction as $\hat{\mathbf{e}}_1$, $\hat{\mathbf{e}}_2$, and $\hat{\mathbf{e}}_3$, the inverse kinematics are given by

$$\begin{aligned}\omega_o &= \left[\begin{array}{ccc} R_2(\alpha)\hat{\mathbf{e}}_1 & \hat{\mathbf{e}}_2 & R_2(\alpha)R_1(\theta)\hat{\mathbf{e}}_3 \end{array}\right]\dot{\mathbf{u}} \\ &= \left[\begin{array}{ccc} \cos\alpha & 0 & -\sin\alpha\cos\theta \\ 0 & 1 & 0 \\ \sin\alpha & 0 & \cos\alpha\cos\theta \end{array}\right]\left[\begin{array}{c} \dot{\theta} \\ \dot{\alpha} \\ \dot{\phi} \end{array}\right].\end{aligned} \tag{4.23}$$

Inverting this relationship gives the forward kinematics

$$\left[\begin{array}{c} \dot{\theta} \\ \dot{\alpha} \\ \dot{\psi} \end{array}\right] = \frac{1}{\cos\theta}\left[\begin{array}{ccc} \cos\alpha\cos\theta & 0 & \sin\alpha\cos\theta \\ \sin\alpha\sin\theta & \cos\theta & -\cos\alpha\sin\theta \\ -\sin\alpha & 0 & \cos\alpha \end{array}\right]\omega_o. \tag{4.24}$$

As with all Euler angle parameterizations, these kinematic equations have a singularity. Here, the singularity occurs when the elevation angle reaches $\theta = \pm\pi/2$. Because the elevation angle is typically small in insect wing kinematics (*e.g.*, maximum amplitude of 25 deg used in [83]), the Euler angle singularity does not pose a problem in describing the wing stroke kinematics.

4.2.3 Aerodynamics

The aerodynamic forces on a flapping wing arise from a complex interaction of the wing with the surrounding fluid. Three primary mechanisms are responsible for aerodynamic force generation [84] — delayed stall during translational motion of the wing due to an attached leading edge vortex, rotational motion during wing stroke reversal, and wake capture when the wing rotates back upon the trailing wake of the previous downstroke/upstroke. Although these effects result from unsteady aerodynamics, they do not rely on the time history of motion during cyclic flapping and, thus, can be effectively modeled using quasi-steady aerodynamics. Several researchers have taken this approach by modeling the aerodynamic forces using blade element theory and

experimentally determined lift and drag coefficients [84, 83, 85, 86, 87, 88].

The aerodynamic model employed here is based off the work in [85], which is modified for flexible wings in this work. In this model, the aerodynamic force is due to two components,

$$F_{aero} = F_t + F_a, \tag{4.25}$$

where F_t is the force due to translational (sweeping) motion and F_a is the force due to the added mass of accelerated fluid. Each force component is computed by dividing the wing into an infinite number of span-wise elements and integrating the contribution of each element using the local wing geometry, as depicted in Fig. 4.3. These forces are a function of the effective feathering angle α_e — the prescribed feathering angle α, plus the feathering angle due to deformation of the wing, δ. Although wing deformation angles may indeed be significant [89], the twist angle, δ, is assumed to be small as a first step in a fluid-structure interaction model. Thus, using a small angle approximation, the feathering angle is given by

$$\begin{aligned} \alpha_e(y,t) &= \alpha(t) + \delta \\ &\approx \alpha(t) + \left(\frac{w_{le}(y,t) - w_{te}(y,t)}{c(y)} \right), \end{aligned} \tag{4.26}$$

where $c(y)$ is the local chord length, $w_{le}(y,t)$ is the leading edge deformation, and $w_{te}(y,t)$ is the trailing edge deformation. In terms of the wing mode shapes, the effective feathering angle is

$$\begin{aligned} \alpha_e(y,t) &= \alpha(t) + \frac{1}{c(y)} \sum_{i=1}^{n} \left[\phi_i(-c/2, y) - \phi_i(c/2, y) \right] \eta_i(t) \\ &= \alpha(t) + \frac{1}{c(y)} \sum_{i=1}^{n} \phi_{\delta_i}(y) \eta_i(t). \end{aligned} \tag{4.27}$$

The translational force component at each span-wise station is composed of lift and drag forces, where the lift and drag coefficients are generated from data obtained

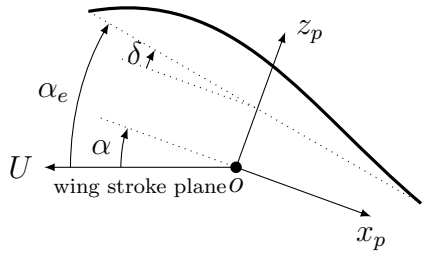

Figure 4.3: A span-wise deformed wing element depicting the feathering angle, α, wing twist angle, δ, and effective feathering angle, α_e, relative to the wing stroke motion with local speed, U.

in dynamically scaled wing flapping experiments [84]. The empirically-derived aerodynamic coefficients are modified from [84] to match the geometry of the plate model, which has no resting camber and thus produces zero lift at zero angle-of-attack. The wing elevation angle, θ, is assumed to be zero, which is consistent with simplified wing stroke kinematics obtained from experimental data [81]. Therefore, the local wing section angle-of-attack is equal to the feathering angle, with a change in sign during the upstroke. In terms of the effective feathering angle α_e, the lift and drag coefficients are

$$\begin{aligned} C_L &= 1.8\sin(2\alpha_e) \\ C_D &= 1.92 - 1.55\cos(2\alpha_e). \end{aligned} \tag{4.28}$$

Because the structural model assumes only out-of-plane deformation, only aerodynamic forces normal to the wing plane enter the structural dynamics. Resolving the lift and drag forces into a force normal to the wing gives a normal force coefficient,

$$C_N = C_L\cos\alpha_e + C_D\sin\alpha_e = 0.13\sin(3\alpha_e) + 3.6\sin\alpha_e. \tag{4.29}$$

The resulting lift, drag, and normal force coefficients are shown in Fig. 4.4.

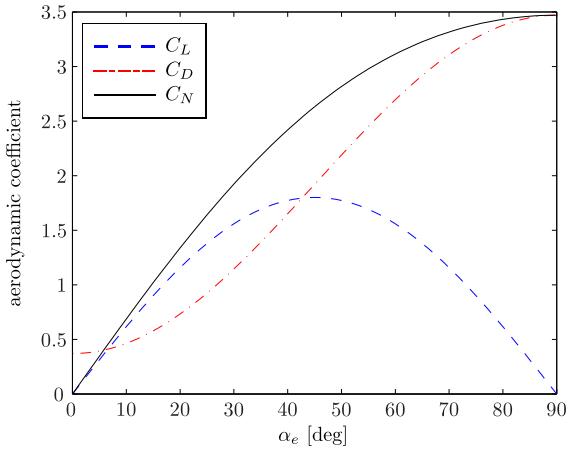

Figure 4.4: Aerodynamic coefficients due to translational motion of the wing, adapted from experimental data obtained from dynamically-scaled wing flapping experiments in [84].

The normal force per unit span due to translational motion at span-wise station y is computed using the local wing station speed and chord

$$F_t(y) = \frac{1}{2}\rho_f U^2(y) C_N(\alpha_e(y)) c(y), \tag{4.30}$$

where ρ_f is the fluid density, $U(y)$ is the local wing speed, and $\alpha_e(y)$ is the local effective feathering angle, and $c(y)$ is the local chord length. Continuing with the assumption that the wing twist angle, δ, is small, the following small angle approximation can be used

$$\sin(\alpha + \delta) \approx \sin\alpha + \delta\cos\alpha. \tag{4.31}$$

Therefore, the normal force coefficient is expanded in terms of the effective feathering

angle, α_e, defined by (4.27) to get

$$C_N(\alpha_e(y)) \approx (0.13\sin(3\alpha) + 3.6\sin\alpha) + (0.39\cos(3\alpha) + 3.6\cos\alpha)\frac{1}{c(y)}\sum_{i=1}^{n}\phi_{\delta_i}(y)\eta_i. \tag{4.32}$$

The translational force enters the structural equations of motion as a generalized force, which is computed via the principle of virtual work. Assuming that the normal force acts at the quarter chord, the i^{th} element of the generalized translational force is given by

$$Q_{t_i} = \int_0^b F_t(y)\phi_i(-c/4, y)\mathrm{d}y, \tag{4.33}$$

where b is the span of one wing, and $\phi_i(-c/4, y)$ is the mode shape along the quarter chord line. The translational generalized force is composed of a deformation-independent term and a stiffness matrix multiplying the structural generalized coordinates, $\mathbf{Q}_t = \mathbf{Q}_{t_0} + Q_{t_\eta}\eta$. Using the definition of the translational force (4.30), the normal aerodynamic coefficient (4.32), and the local wing section velocity $U(t, y) = \dot{\psi}(t)y$, the i^{th} element of the translational generalized force vector is

$$Q_{t_{0_i}}(t) = \frac{1}{2}\rho_f\dot{\psi}^2(t)\left[0.13\sin(3\alpha(t)) + 3.6\sin(\alpha(t))\right]\int_0^b \phi_i(-c/4, y)c(y)y^2\mathrm{d}y. \tag{4.34}$$

Similarly, the (i, j) element of the translational force stiffness matrix is

$$Q_{t_{\eta_{ij}}}(t) = \frac{1}{2}\rho_f\dot{\psi}^2(t)\left[0.39\cos(3\alpha(t)) + 3.6\cos(\alpha(t))\right]\int_0^b \phi_i(-c/4, y)\phi_{\delta_j}(y)y^2\mathrm{d}y. \tag{4.35}$$

The second component of the aerodynamic force is due to the added mass of accelerated fluid. The added mass force arises from the fact that the wing accelerates a volume of fluid as it moves. Here, the classic results of Theodorsen for a small-

amplitude pitching and plunging plate are used to approximate the added mass force (see [90] for a good description). If the axis of feathering rotation relative to the wing coordinate system origin is denoted by x_r, then the added mass force per unit span is given by

$$F_a(y) = \frac{\pi\rho_f c(y)^2}{4}\left[U(y)\dot{\alpha}_e(y) - \ddot{h}(y) - x_r\ddot{\alpha}_e\right], \tag{4.36}$$

where $h(y,t) = \sum \phi_i(x_r, y)\eta_i(t)$ is the out-of-plane wing deformation at the axis of rotation. Using again the principle of virtual work, the i^{th} element of the generalized force due to added mass is given by

$$Q_{a_i}(t) = \int_0^b F_a(y,t)\phi_i(-c/4, y)\mathrm{d}y, \tag{4.37}$$

which is composed of a deformation-independent term, a damping matrix multiplying the structural generalized velocities, and a mass matrix multiplying the structural generalized accelerations, $\mathbf{Q}_a = \mathbf{Q}_{a_0} + Q_{a_{\dot{\eta}}}\dot{\eta} + Q_{a_{\ddot{\eta}}}\ddot{\eta}$. Substituting the expression for α_e (4.27), the i^{th} element of the added mass force vector is

$$Q_{a_{0_i}}(t) = \frac{\pi\rho_f}{4}\int_0^b \phi_i(-c/4, y)c(y)^2\left[\dot{\psi}(t)\dot{\alpha}(t)y - x_r\ddot{\alpha}(t)\right]\mathrm{d}y. \tag{4.38}$$

The (i,j) element of the added mass damping matrix is

$$Q_{a_{\dot{\eta}_{ij}}}(t) = \frac{\pi\rho_f\dot{\psi}(t)}{4}\int_0^b \phi_i(-c/4, y)c(y)y\phi_{\delta_j}(y)\mathrm{d}y. \tag{4.39}$$

The (i,j) element of the added mass acceleration matrix is

$$Q_{a_{\ddot{\eta}_{ij}}} = -\frac{\pi\rho_f}{4}\int_0^b \phi_i(-c/4, y)\left[x_r c(y)\phi_{\delta_j}(y) + c(y)^2\phi_j(x_r, y)\right]\mathrm{d}y. \tag{4.40}$$

Assembling all the generalized aerodynamic forces, the total aerodynamic force on the structural degrees of freedom is

$$\mathbf{Q} = \mathbf{Q}_{t_0} + \mathbf{Q}_{a_0} + Q_{t_\eta}\eta + Q_{a_{\dot\eta}}\dot\eta + Q_{a_{\ddot\eta}}\ddot\eta, \tag{4.41}$$

which is used in (4.18) to describe the coupled fluid-structure interaction of the wing flapping dynamics. The key advantage of the blade element aerodynamic model is that the aerodynamic forces are spatially and temporally resolved for a given set of stroke kinematics *before* a simulation is integrated. Thus, given the stroke kinematics and structural mode shapes, the flapping wing equations of motion take the form of a linear time-varying system

$$M\ddot\eta + C(t)\dot\eta + K(t)\dot\eta = \mathbf{F}(t) \tag{4.42}$$

where the mass, damping, stiffness, and applied forces are given by

$$M = (I - Q_{a_{\ddot\eta}}) \tag{4.43}$$

$$C(t) = -Q_{a_{\dot\eta}}(t) \tag{4.44}$$

$$K(t) = \Omega - (Q^2(t) + P^2(t)) - Q_{t_\eta}(t) \tag{4.45}$$

$$\mathbf{F}(t) = \mathbf{Q}_{t_0}(t) + \mathbf{Q}_{a_0}(t) + M_a \left(\mathbf{C}_a(\mathbf{v}_o(t), \omega_o(t)) - \begin{bmatrix} \dot W(t) \\ \dot P(t) \\ \dot Q(t) \end{bmatrix} \right). \tag{4.46}$$

4.3 Simulation Methods

A simulation environment was developed in MATLAB using the `ode45` numerical integration routine to integrate the linear time-varying flapping-wing dynamics (4.42). The inputs to the simulation are the wing stroke kinematics ($\theta(t)$, $\alpha(t)$, and $\psi(t)$), the wing structural mode shapes, $\phi_i(x, y)$, and frequencies, ω_i, and the wing mass

density, $\rho(x, y)$, and thickness, $h(x, y)$.

The simulation begins by pre-processing the input data to calculate the time-varying forces, stiffness, and damping on the structural modes. First, the prescribed wing stroke angles are used to compute the wing frame angular velocities, ω_o, via the inverse kinematics (4.23). Next, the wing frame velocities and accelerations are computed using the relationship

$$\begin{aligned} \mathbf{v}_o(t) &= -\omega_o \times \mathbf{r}_r \\ \dot{\mathbf{v}}_o(t) &= -\dot{\omega}_o \times \mathbf{r}_r - \omega_o \times (\omega_o \times \mathbf{r}_r)\,, \end{aligned} \tag{4.47}$$

where $\mathbf{r}_r$ is the position of the rotation axis relative to the wing frame origin. Using the structural mode shapes and wing kinematics, the applied acceleration mass matrix M_a and the aerodynamic generalized forces are computed through spatial integration of the mode shapes. Finally, the mass matrix and time-varying forces, stiffness, and damping matrices are assembled according to (4.43) – (4.46), and the dynamics are integrated to obtain the wing shape throughout the flapping cycle.

4.3.1 Simulation parameters for a Manduca sexta wing

Kinematic and structural parameters for a representative *Manduca sexta* wing were obtained using published data from a variety of sources. The wing stroke kinematics are derived from experimental measurement of hawkmoth wing kinematics in [91] and sinusoidal models employed in [87]. The wing stroke position and feathering angles are prescribed for a symmetric wing flapping cycle given by

$$\begin{aligned} \psi(t) &= -A_\psi \cos(2\pi t/T) \\ \alpha(t) &= \frac{\pi}{2} - A_\alpha \tanh\left(\frac{\pi}{2}\sin(2\pi t/T)\right), \end{aligned} \tag{4.48}$$

where A_ψ is the stroke position amplitude, A_α is the feathering angle amplitude, and T is the wing-beat period. We used a nominal wing-beat frequency of 25 Hz,

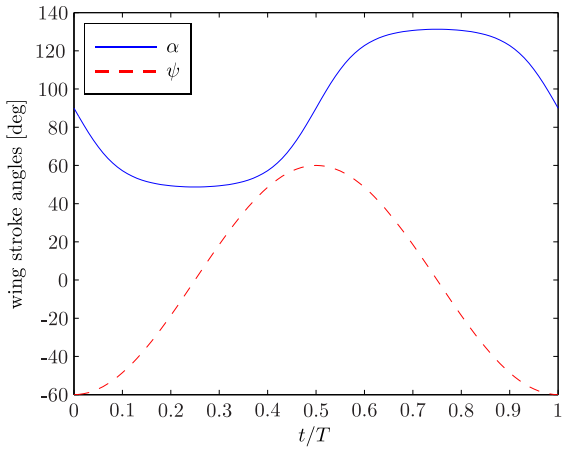

Figure 4.5: Wing stroke angles for a nominal symmetric flapping cycle, showing the wing position angle ψ and wing feathering angle α.

stroke position amplitude of $A_\psi = 60$ deg, and feathering amplitude of $A_\alpha = 45$ deg, all values consistent with previous measurements of *Manduca sexta* wing kinematics (Figure 4.5). An elevation angle, θ, of zero was maintained during the simulation, which approximately models the small elevation changes shown in experimental data [91].

Wing planform geometry was measured from photographs of a hawkmoth forewing from [73], scaled for a 50 mm wing span. Wing thickness was modeled as an exponential decrease in thickness from root to tip and from leading edge to trailing edge, similar to the model employed in [92]. The wing material density was uniform, with a value of $\rho(x, y) = 220$ kg/m^3 to give a forewing mass of approximately 36 mg, consistent with measurements of hawkmoth wing mass in [87].

Structural modes for the simulation can be derived from a finite element model of the wing. However, because the wing is composed of anisotropic vein and membrane structures of variable stiffness and thickness, development of an accurate finite element model can be a substantial effort (see, *e.g.*, [92]). An alternative method is to

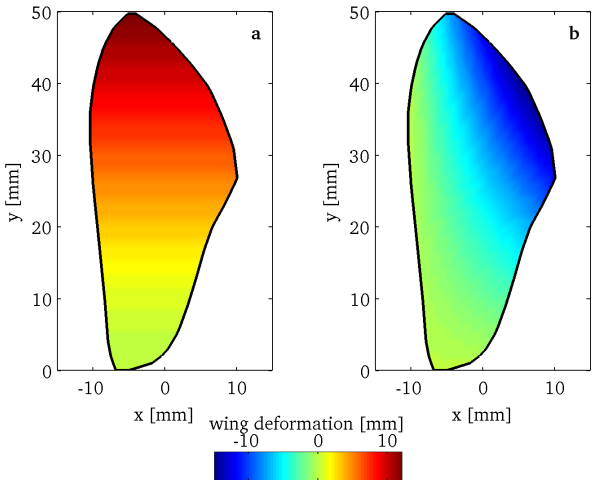

Figure 4.6: Prescribed wing mode shapes showing the out-of-plane deformation in mm. (a) The first bending mode. (b) The first torsion mode.

prescribe assumed wing mode shapes and frequencies. Here, two wing mode shapes were prescribed using the first bending mode and first torsion mode of a cantilevered plate to capture the dominant wing bending effects, as shown in Fig. 4.6. Using the simulation environment, the wing mode frequencies were tuned to achieve reasonable deformation during a flapping cycle, where 95 Hz frequency for the torsion mode and 90 Hz frequency for the bending mode were found to produce realistic wing deformation.

4.3.2 Simulation validation

The wing flapping simulation was validated through comparison to *Manduca* wing flapping experiments in [74], similar to the comparison performed in [81]. These experiments measured the deflection of the wing relative to rigid motion at three locations — the forward-most point on the leading edge, the wing tip, and the aft-most point on the trailing edge. Wing deformation was defined by the angle between the plane of a rotating rigid wing and a line connecting the wing root to the deformed

point (see Fig. 1 in [74]).

The conditions for these experiments were simulated using a wing stroke amplitude of $A_\phi = 54$ deg at a frequency of 26 Hz (adjusted from 25 Hz in order to match the experiment), with a constant wing feathering angle of $\alpha = 90$ deg. The structural generalized coordinates, η, and velocities, $\dot{\eta}$, were initialized to zero and the dynamics were integrated for four wing stroke cycles. The structural dynamics settled into a limit cycle after the second wing stroke cycle, and the fourth wing stroke cycle was used to compute wing deformation at the trailing edge and wing tip for comparison to experimental data collected in [74]. One wing stroke cycle was sampled from the data presented in [74] for the wing tip and trailing edge positions. The simulated results that were obtained are compared to the sampled data, along with second-order Fourier fits of the experimental and simulation data using the first two Fourier coefficients (26 Hz and 72 Hz), shown in Fig. 4.7. Despite the fact that the simulation only integrates four state variables (two modal coordinates and two modal velocities), the simulation captures the overall wing motion well, as evidenced by the similarity between the second-order Fourier fits of each data set (shown in dashed curves). The root mean square (RMS) error between the second-order Fourier fits of the simulation and experiment were computed as 2.5 deg for the wing tip deformation and 2.0 deg for the trailing edge deformation, confirming that the simulation captures the wing motion up to second-order harmonics.

4.3.3 Nominal flapping trajectory

The nominal flapping trajectory defined by the stroke kinematics shown in Fig. 4.5 was simulated to analyze wing deformation during a flapping cycle. The structural generalized coordinates and velocities were initialized to zero, and the dynamics were integrated for four flapping cycles. The wing shape for the deformed wing was compared to the rigid motion of the wing (*i.e.*, the wing position and feathering angles defined by the kinematics). The stroke sequence for the deformed wing shape and

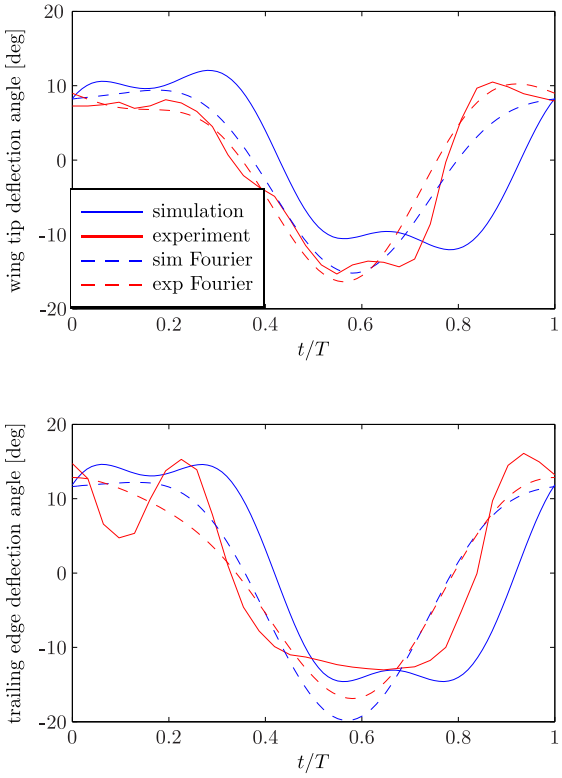

Figure 4.7: Comparison of wing deformation computed from a simulated wing flapping model with experimental data from [74]. Second-order Fourier fits of the the simulation and experimental data are shown in dashed curves.

the rigid wing shape is shown in Fig. 4.8 for the wing section located at 70% span. This span-wise location was chosen to demonstrate the pronounced wing twisting that occurs near the wing tip during stroke reversal. Wing stations closer to the wing root exhibited similar patterns, but with smaller wing twist angles.

The simulation results exhibit pronounced pronation at the beginning of the downstroke and supination at the beginning of the upstroke, which is consistent with observations of moth wing motion [91]. Additionally, wing flexibility creates a slight elevation in the wing tip at stroke reversal, which generates a figure-eight trajectory for the wing tip. As a note, the maximum angle of wing twist δ (angle between the

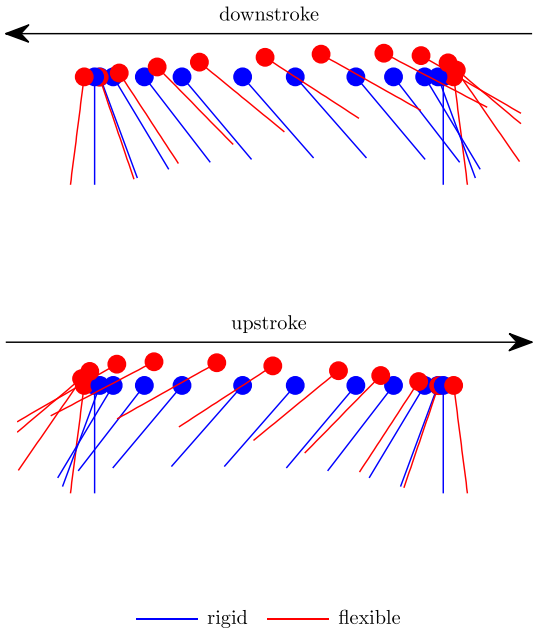

Figure 4.8: The nominal wing stroke sequence showing the deformed (flexible) wing shape compared to the rigid wing motion for the wing section located at 70% span. The filled circle on each wing section indicates the wing leading edge. Each wing section is drawn to scale with its position drawn from the side view of the wing flapping (the body y-axis) and its orientation drawn as viewed down the span-wise axis of the wing (the wing y-axis). Wing sections are sampled uniformly in time.

rigid and elastic chord lines) is approximately 25 deg and varies in magnitude between 0 and 25 deg during the stroke cycle. In the development of the aerodynamic model, the wing twist angle was assumed to be small. An angle of 25 deg results in less than 10% error due to the small angle approximation of the cosine function and less than 4% error due to the approximation of the sine functions. Thus, the small angle assumption is reasonable in this case.

Wing twist at stroke reversals generates large lift transients through the increased wing acceleration due to the release of elastic energy at the end of each stroke (note the

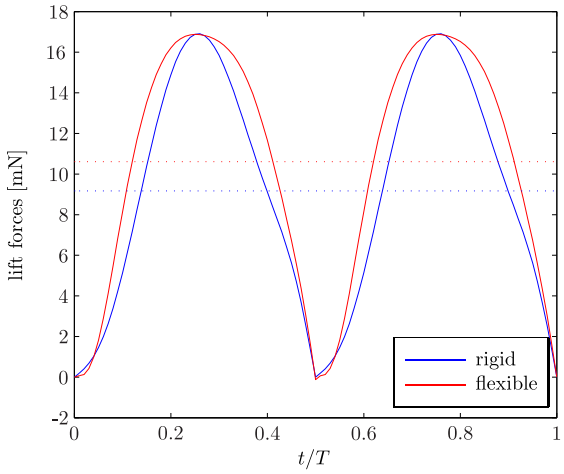

Figure 4.9: Total lift force over one flapping cycle for a rigid and flexible wing, with the mean force shown as a dotted line. The increased force at the beginning and end of each half stroke is due to increased acceleration from the release of elastic energy of the flexible wing (*c.f.* Fig. 4.8).

acceleration at the end of the strokes in Fig. 4.8). These lift transients arising from increased angular velocity were also observed in a computational study performed in [93]. The time history of lift force on a single forewing is shown in Fig. 4.9 to compare the lift acting on the flexible wing with lift generated by a rigid wing. The mean lift force generated by the rigid wing is 9.2 mN, while the flexible wing generates 10.6 mN of lift, a 15% increase in lift. When the lift force is scaled to account for two wings, the lift generated by the nominal flapping sequence is enough for hovering for a 2.15 g hawkmoth, which is within the range of measured mass values in [87].

The nominal flapping trajectory was also simulated in the absence of aerodynamic forces by setting the fluid density ρ_f to zero. This modified simulation isolated the influences of inertial-elastic loads from aerodynamic loads to determine their relative importance in predicting wing shape. Wing deformation angles for the wing tip and wing trailing edge are compared with and without aerodynamic loading in Fig. 4.10. The absence of aerodynamic loading has two effects. First, the deformation amplitude

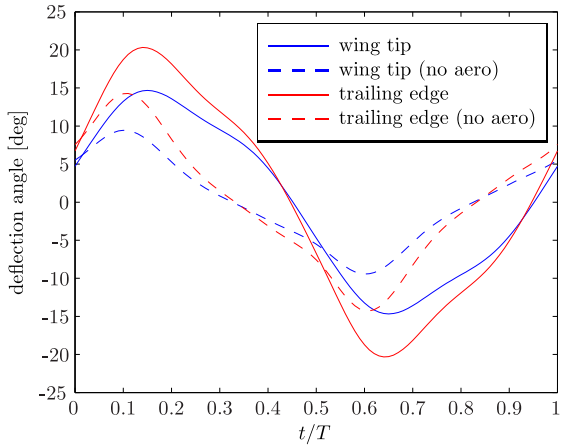

Figure 4.10: Comparison of wing deformation at the wing tip and trailing edge with and without aerodynamic forces. The absence of aerodynamic forces reduces the deformation during mid-stroke and advances the phase of the structural modes.

is reduced primarily during mid-stroke, where the inertial loads are minimum (zero acceleration of position angle ψ), and where the translational aerodynamic loads are maximum (maximum translational velocity). The motion during stroke reversal, however, is very similar due to the dominance of inertial-elastic loads during this portion of the stroke. Second, the deformation in the absence of aerodynamic forces is phase advanced by $\sim$30 deg due to the absence of aerodynamic damping. The maximum deflection is reduced by 35% for the wing tip and 30% for the trailing edge in the absence of aerodynamic loads, indicating that the inertial loads play a larger role in predicting wing shape. These results are supported by the wing flapping experiments performed in [74], where inertial loads were shown to dominate the aerodynamic loads.

4.4 Sensor Placement Results

In this section, strain measurements on a flapping wing are demonstrated to be sufficient to reconstruct perturbations in wing rotation rates arising from, *e.g.*, body

rotations due to external disturbances. Three methods of analysis are employed to demonstrate the results. First, nonlinear observability tools are applied to a slightly simplified model to analytically determine the conditions required for observability of rotation rates. Second, a numerical study is performed using the empirical observability Gramian in conjunction with the simulation environment. The numerical study yields quantitative measures of observability and probes questions regarding favorable sensor locations and types. Finally, the observability-based optimal sensor placement problem is solved to predict favorable sensor locations, and a comparison to mapped sensor locations on a hawkmoth wing is performed.

4.4.1 Rotation rates are observable from wing strain measurements

Motivated by the experimental evidence that inertial loads play a much larger role than aerodynamic loads in determining wing deformation [74], observability of rotation rates is analyzed under no aerodynamic loading. The absence of aerodynamics simplifies the dynamics, which allows the observability analysis to be analytically tractable. This simplification is removed for numerical observability studies in the next section. Additionally, the wing velocities and accelerations are rewritten in terms of the applied angular rates, ω, and the point of rotation, $\mathbf{r}_r$, as described in (4.47). For the nominal trajectory studied here, the point of rotation is located on the wing root chord, which gives $y_r = z_r = 0$. Substituting the computed values for the wing velocities into (4.42) and removing the aerodynamic terms, the wing flapping dynamics reduce to

$$\ddot{\eta} + \left(\Omega - (P^2 + Q^2)\right)\eta = M_a \begin{bmatrix} x_r\left(2PR - \dot{Q}\right) \\ -QR - \dot{P} \\ PR - \dot{Q} \end{bmatrix}. \tag{4.49}$$

The measurements obtained by campaniform sensilla distributed across the wing

are modeled using the local wing strain. Experimental evidence has suggested that these mechanoreceptors can measure both tension and compression [94], therefore the sensor information is modeled using the wing strain at the sensor location. Linear elastic theory states that strain measurements are proportional to the local curvature of the wing. For a strain sensor located at $\mathbf{r}_s = x_s\hat{\mathbf{i}}_p + y_s\hat{\mathbf{j}}_p + z_s\hat{\mathbf{k}}_p$, the strain measurement vector is given in by [80]

$$\epsilon = -z_s \begin{bmatrix} \partial^2 w(x_s, y_s)/\partial x^2 \\ \partial^2 w(x_s, y_s)/\partial y^2 \\ 2\partial^2 w(x_s, y_s)/\partial x \partial y \end{bmatrix}, \tag{4.50}$$

which gives the chord-wise bending strain, span-wise bending strain, and shear strain. In terms of the modal coordinates, the strain measurement is

$$\epsilon = -\sum_{i=1}^{n} z_s \begin{bmatrix} \partial^2 \phi_i(x_s, y_s)/\partial x^2 \\ \partial^2 \phi_i(x_s, y_s)/\partial y^2 \\ 2\partial^2 \phi_i(x_s, y_s)/\partial x \partial y \end{bmatrix} \eta_i. \tag{4.51}$$

In this analysis, the strain sensors are assumed to report a scalar value as a linear combination of the strain vector components (*e.g.*, only bending or shear strain or some combination). Therefore, the measurement model is a linear combination of the modal coordinates:

$$y = H\eta, \tag{4.52}$$

where H is a function of the sensor locations, which (for now) are assumed to be known.

The observability rank condition is applied to the wing flapping dynamics to test if wing rotation rates (P, Q, R) are observable using strain measurements on the wing. The wing flapping system is modeled with the control input variable $u = \begin{bmatrix} \dot{P} & \dot{Q} & \dot{R} \end{bmatrix}^T$ (*i.e.*, the wing rotational accelerations are known inputs), and

state vector $\mathbf{x} = \begin{bmatrix} \eta^T & \dot{\eta}^T & P & Q & R \end{bmatrix}^T$. Rewriting the dynamics (4.49) in control-affine form gives

$$\begin{aligned} \dot{\mathbf{x}} &= \begin{bmatrix} \dot{\eta} \\ K(\omega_o)\eta + (2\mathbf{M}_1 x_r + \mathbf{M}_3)\, PR - \mathbf{M}_2 QR \\ 0 \\ 0 \\ 0 \end{bmatrix} + \begin{bmatrix} \mathbf{0} & \mathbf{0} & \mathbf{0} \\ -\mathbf{M}_2 & -\mathbf{M}_1 x_r - \mathbf{M}_3 & \mathbf{0} \\ 1 & 0 & 0 \\ 0 & 1 & 0 \\ 0 & 0 & 1 \end{bmatrix} \mathbf{u} \\ \mathbf{y} &= H\eta, \end{aligned} \tag{4.53}$$

where $K(\omega_o) = P^2 + Q^2 - \Omega$ is the stiffness matrix, and $\mathbf{M}_j$ denotes the j^{th} column of the M_a matrix. We consider the case of r structural modes, with r linearly independent strain measurements (*i.e.*, $H \in \mathbb{R}^{r \times r}$ is full rank). Because H is full rank, we can equivalently consider the output $y = \eta$. Using this output, the Lie derivatives with respect to the drift vector field, $\mathbf{f}_o(\mathbf{x})$, are considered. Computing the Lie derivatives, the rank of the matrix

$$\mathrm{d}\mathcal{O} = \frac{\partial}{\partial \mathbf{x}} \begin{bmatrix} \mathbf{h} \\ L_{\mathbf{f}_o}\mathbf{h} \\ L^2_{\mathbf{f}_o}\mathbf{h} \\ L^3_{\mathbf{f}_o}\mathbf{h} \end{bmatrix} \tag{4.54}$$

is found to be deficient by one, and the fourth-order Lie derivative $L^4_{\mathbf{f}_o}\mathbf{h}$ is linearly dependent on the lower-order derivatives. Thus, the system is unobservable without

active control input. If control input is applied along any of the axes, the matrix

$$\mathrm{d}\mathcal{O} = \frac{\partial}{\partial \mathbf{x}} \begin{bmatrix} \mathbf{h} \\ L_{\mathbf{f}_o}\mathbf{h} \\ L^2_{\mathbf{f}_o}\mathbf{h} \\ L^3_{\mathbf{f}_o}\mathbf{h} \\ L_{\mathbf{f}_i}L^2_{\mathbf{f}_o}\mathbf{h} \end{bmatrix} \tag{4.55}$$

is full rank for any input vector field $\mathbf{f}_i$, $i = 1, \ldots, 3$. Therefore, the system is locally weakly observable if rotational acceleration is applied in any axis. Thus, strain measurements can be used to reconstruct wing rotation rates, whether they arise from the normal prescribed wing motion or from external disturbances. Furthermore, the condition of $\mathrm{d}\mathcal{O}$ is improved by application of actuation in multiple axes. For the case of the nominal wing flapping trajectory, all axes have variable angular acceleration over time, which improves system observability.

The presence of the control vector fields $\mathbf{f}_i(\mathbf{x})$ in the observability matrix $\mathrm{d}\mathcal{O}$ indicates that angular acceleration in at least one axis is required for angular rate observability. This is due to the fact that the angular rates induce wing deformation via Coriolis forces, which are orthogonal to the angular velocity vector. If no angular acceleration is applied, the angular velocity vector is constant in time, and the space of angular velocities that induce Coriolis forces is a plane, which does not span the three-dimensional space of wing angular velocities. This necessity for angular acceleration is depicted in Fig. 4.11. Because the flapping motion continuously changes angular velocity, the full space of angular rates is sampled, satisfying the observability conditions. For the nominal flapping sequence, the angular velocity vector sweeps through the space of angular rates, as shown in Fig. 4.12, which allows detection of rotations in any direction.

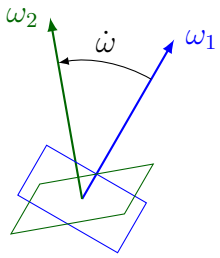

Figure 4.11: Pictorial representation of the necessity for angular acceleration to observe body and wing rotation rates using strain sensing. Angular rates are encoded through Coriolis forces on the wing that induce strain patterns. For a constant angular rate ω_1, the space of Coriolis-inducing angular velocities is the plane orthogonal to the constant angular velocity vector, which does not span the three-dimensional space of angular velocities. If angular acceleration is applied, the direction of the angular velocity vector changes, which allows the full space to be spanned using the two planes.

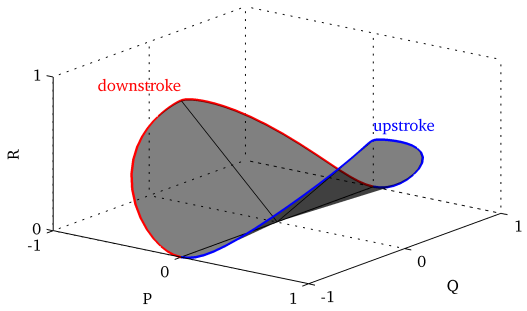

Figure 4.12: The surface swept out by the wing angular velocity unit vector during the nominal flapping sequence. Because the angular velocity vector direction changes in time, the wing and body rotation rates are observable. The time history of the angular velocity vector forms a well-conditioned basis for observing the Coriolis-inducing rotation rates, making the wing and body rotation rates easier to detect.

4.4.2 Effect of strain sensor location and type

The previous section demonstrated that wing angular rates can be reconstructed from a time history of strain measurements on the wing. In this section, an investigation

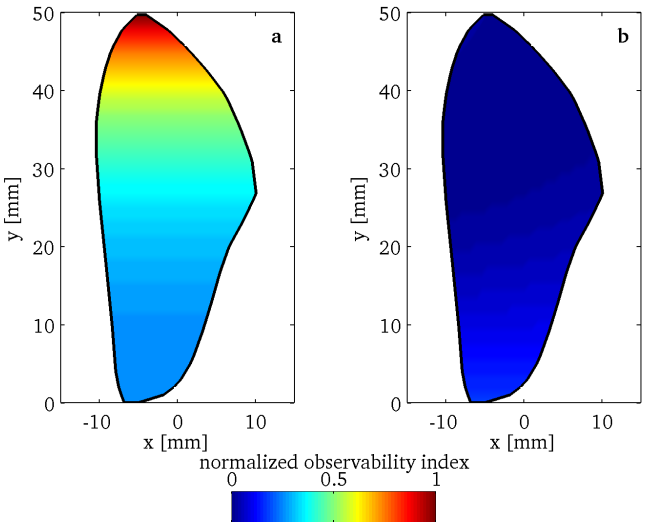

Figure 4.13: Observability indices for varying sensor location and type, normalized by the maximum index. (a) The observability index for sensors measuring shear strain, which is maximum at the wing tip where wing twist is maximum. (b) The observability index for sensors measuring span-wise bending strain, which is maximum at the wing root.

is performed to discover the role of sensor location and type (bending or shear strain) in wing rotation sensing. Sensor fitness is measured by the empirical observability Gramian (see Chapter 2), which gives a quantitative measure of system observability for a given sensor configuration.

The empirical observability Gramian was computed over the nominal flapping cycle for varying sensor location and type by perturbing the angular rate initial conditions in each of the three wing axes, simulating a disturbance to the wing kinematics. Strain measurements were sampled in a grid of 51 span-wise stations, with 21 chord-wise samples per station, resulting in a minimum grid spacing of 1mm. The empirical observability Gramian was computed for each sensor location for sensors measuring bending strain, ϵ_{yy}, and shear strain, ϵ_{xy} (note that the assumed structural modes used here do not have chord-wise bending, so ϵ_{xx} is identically zero).

The observability index for each sensor location and type is shown in Fig. 4.13. The observability indices indicate that the angular rates are encoded primarily through shear strain (left side of Fig. 4.13), with the maximum information gained at the wing tip, where wing twist is dominant during pronation and supination. Bending strain (right side of Fig. 4.13) is largest at the wing root and encodes more information about wing rotation rates than shear strain near the wing root. These results provide hypotheses regarding favorable sensor type as a function of location on the wing — sensors near the wing tip provide more information when sensitive to shear strain, while sensors near the wing root provide more information when sensitive to bending strain.

A second set of Gramian computations were performed to assess the relative observability of angular rate perturbations to the *body* axis system, which is fixed to the moth body with x axis pointing aft along the wing stroke plane, y right in the wing stroke plane, and z normal to the wing stroke plane, as shown in Fig. 4.14. Angular rate perturbations were applied in each of the three axis directions: roll (x), pitch (y), and yaw (z). Because the nominal wing stroke is symmetric between the left and right wing, only the right wing was simulated to compute the empirical observability Gramians. The Gramian for the left wing is computed from the Gramian for the right wing by noting that the perturbations in the x and z axes are opposite for the left wing,

$$\tilde{W}_l = \begin{bmatrix} \tilde{W}_r(1,1) & -\tilde{W}_r(1,2) & \tilde{W}_r(1,3) \\ -\tilde{W}_r(2,1) & \tilde{W}_r(2,2) & -\tilde{W}_r(2,3) \\ \tilde{W}_r(3,1) & -\tilde{W}_r(3,2) & \tilde{W}_r(3,3) \end{bmatrix}, \tag{4.56}$$

where $\tilde{W}_r(i,j)$ is the (i,j) element of the empirical observability Gramian computed from the simulation of the right wing. This complementary nature of the information encoded by sensors on the two wings improves the observability index when summed together. Thus, information fused between sensors on both wings provides a better estimate of the body rotation rates.

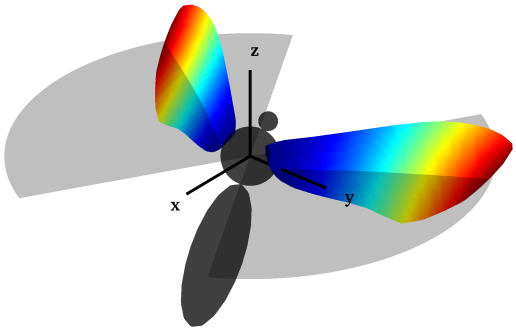

Figure 4.14: Simulation of the nominal flapping trajectory showing the body axis system, wing stroke plane, and wings at 75% downstroke.

The eigenvalues and eigenvectors of the observability Gramians for shear strain and bending strain sensors were computed and averaged over all sensors spatially distributed across the wing, as shown in Fig. 4.15. The mean eigenvectors for the computed observability Gramians are aligned with the body axis system, due to the alignment of the wing stroke plane with the body axis system. The minimum observability Gramian eigenvalue corresponds to rotation about the body z axis (the axis normal to the wing stroke plane), which is the least observable rotation mode. The largest two eigenvalues correspond to rotation about the body x and y axes, with the y rotational mode having a slightly higher eigenvalue on average. For the case of shear strain sensors, the eigenvalues for x and y rotation are approximately 35% larger than the eigenvalue for z rotation, which indicates that roll and pitch rotations are more easily detected than yaw rotations. However, bending strain measurements yield a more well-conditioned observability Gramian (smaller observability condition number), with the maximum eigenvalue 10% larger than the minimum, thus providing more uniform sensing capabilities in the three axes of rotation.

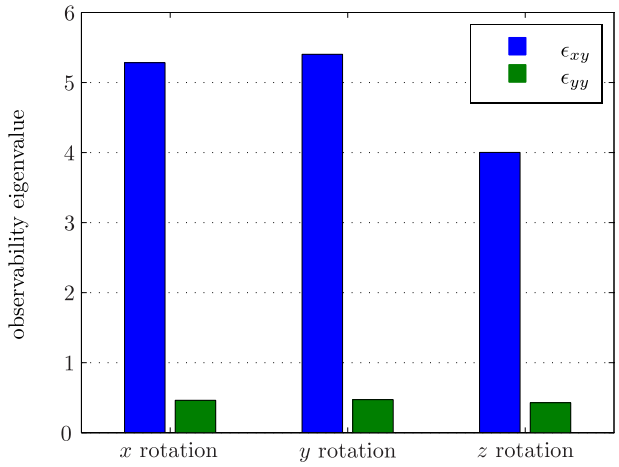

Figure 4.15: Comparison of spatially averaged observability Gramian eigenvalues for rotation about the body x, y, and z axes using either shear strain (ϵ_{xy}) or bending strain sensing (ϵ_{yy}). In both types of sensing, rotation about the z axis is the least observable mode, while rotation about x and y are the most observable modes. Bending strain sensing provides a smaller observability condition number with more uniform eigenvalues.

The observability Gramian eigenvalues give a measure of the rotational rate encoded in strain energy. Body rotation induces a change in the strain pattern from a nominal flapping sequence that allows the rotations to be observable. This change in strain pattern over the nominal flapping cycle is shown in Figure 4.16 for perturbations in the rotation rate for each of the three body axes. The changes in the strain patterns are particularly distinguishable during the upstroke, where the change in wing stroke kinematics has had sufficient time to induce noticeable change in deformation.

4.4.3 Optimal sensor configuration for body rate estimation

It is apparent that the spatial distribution of strain sensors can affect the measure of body rotation rate observability and, thus, the accuracy to which the body rotation rates can be reconstructed from instantaneous strain measurements (*c.f.*, Fig. 4.13).

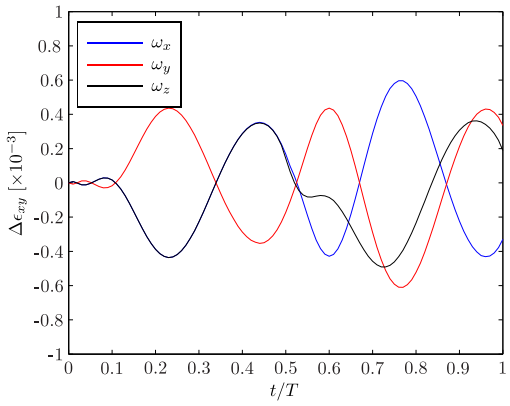

Figure 4.16: Change in the mean shear strain over one flapping cycle due to rotations in each of the three body axes.

In this section, the sensor locations and types (shear or bending strain) that optimize observability of body rotation rates are computed based upon the empirical observability Gramian. The optimal sensor sets are compared to locations of campaniform sensilla found on Hawkmoth wings [73], and hypotheses for sensor type distribution are developed for the known campaniform locations.

The optimal sensor placement problem (3.9) is formed to compute the optimal sensor configuration for rotation rate observability. In the interest of finding a sensor set that provides both a large observability index and a small observability condition number, the cost function is formed as a weighted sum of the condition number and the inverse of the observability index (the unobservability index), both of which are convex functions of the Gramian, $\tilde{W}$ [29]. Defining the condition number as $\kappa(\tilde{W})$, the inverse of the minimum eigenvalue as $\nu(\tilde{W})$, and the weight $w_\nu \geq 0$, the observability-based sensor placement cost function is

$$J[\tilde{W}] = \kappa(\tilde{W}) + w_\nu \nu(\tilde{W}). \tag{4.57}$$

The input data to the optimization problem are computed using the empirical observability Gramian [37] and the nominal flapping sequence, where the Gramians are computed for each allowed sensor location. The sensors are constrained to be located on one of the wing veins to be consistent with the campaniform locations found in [73]. The wing veins serve as a wing support structure as well as a nerve pathway for the sensory information. A map of the wing venation pattern and locations of wing campaniform sensors were measured from data presented in [73]. The set of possible sensor locations was constructed by discretizing the measured wing veins using a 2 mm spacing of sensors along each vein, for a total of 123 possible sensor locations.

The optimal sensor placement problem (3.9) was solved for the placement of $r = 20$ sensors with a cost function weight $w_\nu = 0.4$ using the `cvx` convex optimization modeling language toolbox for MATLAB [95, 96]. The resulting sensor locations and types are shown in Fig. 4.17 compared to the the locations of campaniform sensors measured from [73]. The computed sensor locations form into two clusters: one located near the wing root composed of bending strain sensors, and one located near the wing tip composed of shear strain sensors. These two clusters yield a sensor set with desirable observability characteristics — the bending strain sensors provide more equal sensing in each rotational axis through a low observability condition number, while the shear strain sensors provide more sensitivity to body rotations through a large observability index. Although the computed pattern does not identically match the measured locations of campaniform sensilla, both sensor sets show a similar trend. The campaniforms form into three clusters: one near the root, one mid-wing, and one at the tip. Not shown in Fig. 4.17 are an additional $\sim$200 campaniforms clustered very near the root at the wing hinge. The campaniforms cover the areas that the computations show to be most informative of body rotation rates near the root and tip.

Although the computed sensor sets are heterogeneously composed of bending strain and shear strain sensors, the variation in information that each campaniform

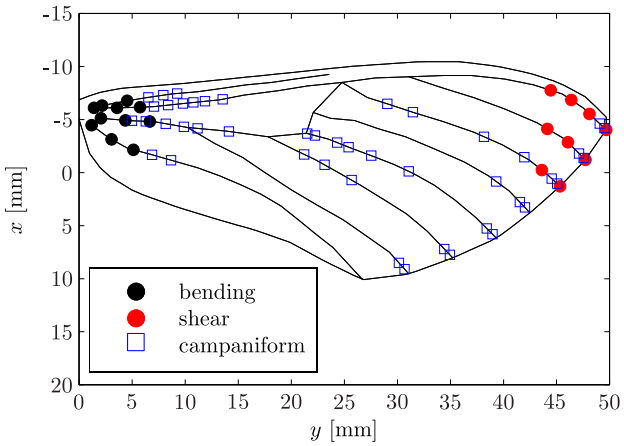

Figure 4.17: Optimal set of $r = 20$ sensors compared to locations of campaniform sensilla found on a hawkmoth forewing in [73]. The computed sensor locations combine bending strain sensors clustered at the wing root with shear strain sensors clustered at the wing tip. Not shown are the clusters of campaniform sensilla located at the wing root near the wing hinge, which account for ∼200 of the ∼250 campaniform sensors.

sensillum encodes is not well-understood. Given the measured locations of campaniform sensilla on the hawkmoth forewing, the sensor type (bending or shear strain) that optimizes body rate observability was computed for each location according to the cost function (4.57) with a weight $w_\nu = 0.4$. The resulting sensor types are shown in Fig. 4.18, where the sensilla divide into a group of bending sensors near the root and a group of shear sensors near the tip. This provides a hypothesis for how the heterogeneity could be distributed across the wing for optimal observability of body rotation rates.

4.5 Discussion

Through modeling and observability analysis, it has been shown that strain sensing on insect wings is sufficient to reconstruct wing and body rotation rates, supporting the hypothesis that the wings of *Manduca* (and other species of flying insects) serve

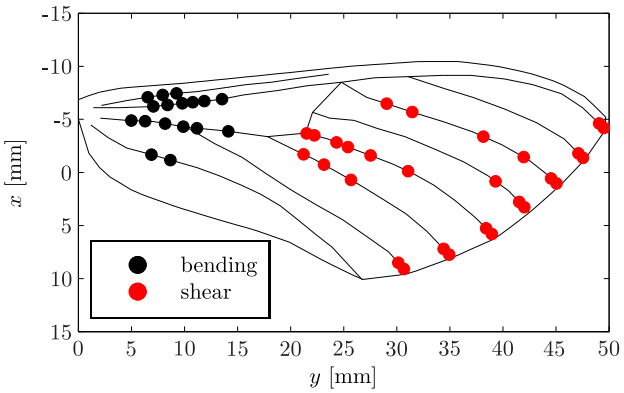

Figure 4.18: Optimal sensor type selection for campaniform sensilla mapped from a hawkmoth forewing (campaniform sensilla locations from [73]). The sensors are divided into two groups: bending strain sensors near the root where bending strain is maximum, and shear strain sensors near the tip where shear strain is maximum.

not only as actuators, but also as mechanosensors. The continuously changing wing kinematic angles produce inertial loads on the wing in the form of linear and angular acceleration, and centripetal and Coriolis forces, which induce spatial and temporal strain patterns that encode the applied rates and accelerations. This active motion of the wing was shown to be necessary for angular rate observability in all axes, where the change in angular rate vector in time allows the direction of sensitivity to the Coriolis force to change in time. Thus, the wing flapping motion allows the wing to be sensitive to rotation-induced Coriolis forces in any direction. This inherit coupling between sensing and actuation highlights the role of nonlinear observability analysis and sensor placement in analysis of complex systems. Furthermore, it was demonstrated that body rate information encoded by strain sensors on one wing is complementary to the information encoded on the opposite wing, indicating that if sensory data are fused from both wings, more accurate measurement of body rates is possible.

The effects of strain sensor location and type on rotation rate observability were

analyzed via the empirical observability Gramian. The most information about body rotation rates was found to be encoded as shear strain due to wing twisting, and sensors near the wing tip were found to be best positioned to measure the shear strain. The shear strain energy is dominant due to the pronounced twisting during wing pronation and supination. The timing and magnitude of the wing twist are perturbed by body rotation disturbances, which allows these disturbances to be easily detected from a time history of shear strain. Although wing bending strain provides less information about body rotation rates, these sensors are more equally sensitive to rotations in each of the three body axes. A well-balanced combination of shear strain and bending strain sensors provides large amounts of information about body rotation rates that is not directionally sensitive.

The observability-based optimal sensor placement problem was solved for strain sensor locations and types along the *Manduca* forewing. The optimal sensor set consisted of two clusters of sensors — one cluster of shear strain sensors near the wing tip and one cluster of bending strain sensors near the wing root. The campaniform sensilla mapped from a hawkmoth forewing also contain a large cluster of sensors near the wing root, and pairs of sensors on each wing vein at the wing tip, suggesting that these sensor sets could be used for measuring body rotation rates. The fact that the true campaniform locations are not predicted by the observability-based sensor placement is not surprising due to the fact that strain measurements likely serve multiple sensory roles. Here, sensor location and type were optimized for observing rotation rates, but the same strain information is useful for proprioceptive sensing for, *e.g.*, wing-beat timing [77, 97]. Nevertheless, the campaniform sensilla on the hawkmoth forewing cover the areas with the most information about body rotation rates and, thus, are well-placed for the wings to serve as gyroscopic sensors. The relative composition of shear and bending sensors is dependent on the weighting in the observability-based cost function. A high weighting on the unobservability index results in larger portion of shear strain sensors due to more body rotation rate

information encoded through wing twisting. A low weight results in a more bending strain sensors that more evenly measure rotation rates in each axis.

The directional sensitivity of strain sensors is an interesting component to the sensor placement results. The campaniform sensilla found on insect wings and halteres have two levels of signal filtering — a biomechanical filter due to the geometry and material makeup of the campaniform structure, and neural filtering on the strain-induced signals [98]. The observability tools utilized in this work may be a useful complement to a neural study to hypothesize campaniform directional sensitivity and interpret sensing capabilities for discovered campaniform biomechanical and neural properties. Properties of the neural filtering may be discovered by the sensor compression problem detailed in Chapter 3, which is an interesting avenue for future work.

Chapter 5

ROBOTIC NAVIGATION WITH LIMITED SENSORS: OBSERVABILITY-BASED GUIDANCE TRAJECTORIES

It is apparent from the observability measures detailed in Chapter 2 that the system nominal trajectory $(\mathbf{x}^0(t), \mathbf{u}^0(t))$ has an impact on the observability measure and, thus, the estimation performance. In some cases, the proper choice of trajectory changes the system from unobservable to observable (*e.g.*, when control actuation is required due to the presence of $L_{\mathbf{f}_i}\mathbf{h}$ in the observation space $\mathcal{O}$). In this chapter, the observability measures are used to develop guidance trajectories for robot navigation. In particular, the focus is centered on robotic navigation with limited inertial sensors, where active vehicle motion is used to improve navigation capabilities. First, the observability-based guidance problem is formally stated in Section 5.1. Analytical solutions to the observability-based guidance problem for four different robot navigation scenarios are presented. Trajectories for uniform flow field identification are developed in Section 5.2, followed by range-only and bearing-only guidance trajectories in Sections 5.3 and 5.4. The guidance trajectories are generalized to higher-dimensional nonholonomic models of robot motion in Section 5.5. Finally, the optimal trajectories are demonstrated in simulation to improve estimation performance in Section 5.6.

5.1 Problem Statement

Many vehicles are forced to operate with limited inertial sensing due to environmental restrictions or economic infeasibility. In the underwater environment, for example, a common form of navigation is through the use of a single ranging beacon. Vehicles operating in GPS-denied or GPS-degraded environments, such as indoors, urban ar-

eas, or in the presence of GPS jamming must resort to other sensors for localization such as vision-based bearing measurements. In all of these cases, complete inertial position and orientation data are unavailable and must be reconstructed using an estimator. Because the vehicle path affects the quality of information collected by the limited set of sensors, an observability-based guidance scheme can be used to improve navigation capabilities. In this section, the observability-based guidance problem is formally stated for vehicles navigating with limited inertial sensors.

5.1.1 Motivating example

The observability-based guidance problem was inspired by the first unmanned flight across the Atlantic by the *Aerosonde* [99]. The *Aerosonde* was able to cross the Atlantic with limited sensor information and no communication with a ground station for the majority of the flight. An on-board GPS unit was used to measure inertial position and velocity during the flight and a pitot probe measured airspeed, however, no compass was installed due to payload restrictions. The standard method of wind calculation through vector subtraction, $\mathbf{V}_w = \mathbf{V}_g - \mathbf{V}_a$, was therefore not possible due to unknown heading information. The *Aerosonde* instead used ingenuitive flight path planning to sample the wind at different headings. The aircraft made 90-degree turns in flight to obtain ground speed measurements at different headings, which allowed the wind vector to be triangulated as depicted in Fig. 5.1. Note that if the planned trajectory is a straight, constant speed path, then the measured ground velocity vectors will be identical at every point, therefore the wind velocity vector cannot be determined using straight flight paths.

The *Aerosonde* problem demonstrates the inherit coupling between sensing and actuation in nonlinear systems — the system observability is dependent upon the choice of trajectory. Observability-based guidance considers the question: what is the *most informative* way to move the vehicle? This problem can be formally stated using the observability measures developed in Chapter 2.

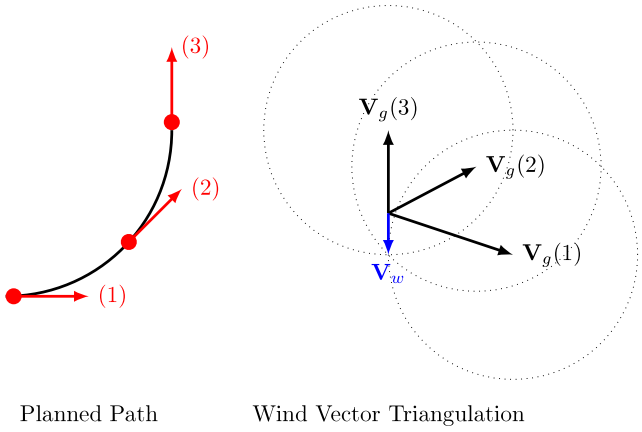

Figure 5.1: Wind estimation technique performed by the *Aerosonde*. On the left is a planned trajectory and three points where the ground velocity vector, $\mathbf{V}_g$, is measured. On the right is the measured ground velocities and circles indicating the measured scalar airspeed. The wind velocity vector, $\mathbf{V}_w$, is triangulated in this way.

5.1.2 Formal statement

Let the vehicle dynamics be given in the control-affine form (2.1) with states $\mathbf{x}$, measurements $\mathbf{y}$, and inputs $\mathbf{u}$. Let $(\mathbf{x}^0(t), \mathbf{u}^0(t))$ be the unknown trajectory that should be generated to optimize an observability measure. In terms of the observability Gramian, the observability-based guidance problem is formally given by the finite time horizon optimization problem

$$\begin{aligned}
\min_{\mathbf{x}^0(t),\mathbf{u}^0(t)} \quad & J[W(t_f)] \\
\text{subject to} \quad & \dot{\mathbf{x}}^0 = \mathbf{f}_0(\mathbf{x}^0) + \sum_{i=1}^{m} \mathbf{f}_i(\mathbf{x}^0)\mathbf{u}^0 \\
& \mathbf{y} = \mathbf{h}(\mathbf{x}^0) \\
& \dot{\Phi} = A(\mathbf{x}^0(t), \mathbf{u}^0(t))\Phi \\
& \dot{W} = \Phi^T C^T(\mathbf{x}^0(t)) C(\mathbf{x}^0(t))\Phi \\
& \Phi(0) = I, \quad W(0) = 0,
\end{aligned} \tag{5.1}$$

where $J[\cdot]$ is a convex measure of the observability Gramian W (*e.g.*, the condition number) and t_f is the fixed time horizon.

Unlike the optimal sensor placement problem (3.2), it is difficult to develop any general solution techniques for the observability-based guidance problem (5.1). This is primarily due to the fact that the observability Gramian is not an affine function of the trajectory $\mathbf{x}^0(t)$, therefore, the observability cost $J[W(t_f)]$ is a non-convex, non-differentiable function of the vehicle trajectory. For particular sets of dynamics, however, the observability Gramian can be written in closed-form as a function of the linearization trajectory.

In this chapter, the constant-speed kinematic model of robot motion is employed

$$\frac{\mathrm{d}}{\mathrm{d}t}\begin{bmatrix} x_N \\ y_E \\ \theta \end{bmatrix} = \begin{bmatrix} V\cos\theta \\ V\sin\theta \\ 0 \end{bmatrix} + \begin{bmatrix} 0 \\ 0 \\ 1 \end{bmatrix}\omega, \tag{5.2}$$

where x_N and y_E are the north and east positions of the vehicle in the plane, θ is the inertial orientation of the vehicle relative to the north direction, ω is the turning rate control input, and V is the known vehicle speed. Using this motion model, a number of analytical solutions to (5.1) can be computed for various sensor sets. The optimal trajectories are derived by considering the geometric properties of the observability Gramian. By specifying the trajectory geometry (*e.g.*, the trajectory centroid or inertia), the eigenvalues of the observability Gramian can be controlled. This process of geometry-based trajectory optimization is described in the following sections for a number of navigation scenarios.

5.2 Uniform Flow Field Identification

The motivating example of the *Aerosonde* performing wind estimation can be posed as an observability-based guidance problem to find the optimal motion strategy to

get the most information about the unknown wind speed and direction. The unicycle motion model (5.2) is modified to include constant (unknown) winds, W_x and W_y, and measurement of inertial position to obtain

$$\frac{\mathrm{d}}{\mathrm{d}t}\begin{bmatrix} x_N \\ y_E \\ \theta \\ W_x \\ W_y \end{bmatrix} = \begin{bmatrix} V\cos\theta + W_x \\ V\sin\theta + W_y \\ 0 \\ 0 \\ 0 \end{bmatrix} + \begin{bmatrix} 0 \\ 0 \\ 1 \\ 0 \\ 0 \end{bmatrix} \omega \tag{5.3}$$
$$\mathbf{y} = \begin{bmatrix} x_N \\ y_E \end{bmatrix},$$

where the vehicle speed V is the flow-relative speed.

5.2.1 Observability analysis

The observability of system (5.3) is analyzed to determine the necessary control inputs to enable observability of wind speed and direction. The results of this analysis are summarized in the following theorem.

Theorem 2 (Wind Observability)**.** *System (5.3) is observable with non-zero heading rate input, and unobservable without heading rate input.*

Proof. For (5.3), the nonlinear observability matrix is given by

$$d\mathcal{O} = \frac{\partial}{\partial \mathbf{x}}\begin{bmatrix} \mathbf{h} \\ L_{\mathbf{f}_0}\mathbf{h} \\ L_{\mathbf{f}_1}L_{\mathbf{f}_0}\mathbf{h} \end{bmatrix} = \begin{bmatrix} 1 & 0 & 0 & 0 & 0 \\ 0 & 1 & 0 & 0 & 0 \\ 0 & 0 & -V\sin\theta & 1 & 0 \\ 0 & 0 & V\cos\theta & 0 & 1 \\ 0 & 0 & -V\cos\theta & 0 & 0 \\ 0 & 0 & -V\sin\theta & 0 & 0 \end{bmatrix}, \tag{5.4}$$

which is full rank for any value of θ. Therefore the system is everywhere locally observable if non-zero turn rate is applied. Note that higher-order Lie derivatives with respect to the drift vector field, $L^k_{\mathbf{f}_0}\mathbf{h}$, are zero for $k > 1$. Therefore, if zero control input is used, the nonlinear observability matrix $d\mathcal{O}$ consists of only the first four rows of (5.4), which drops the rank to four. This finding agrees with the geometric arguments shown in Fig. 5.1, where a straight path (*i.e.*, no control input) yields dependent velocity measurements and an unobservable wind vector, but a curved path (*i.e.*, nonzero control input) allows the wind vector to be observed. □

5.2.2 Geometric interpretation of the observability Gramian

Knowing that turning motions are required for observability of (5.3), an analytical solution to the observability-based guidance problem (5.1) can be derived using the observability Gramian condition number as the objective to minimize. Let $u^0(t) = \omega(t)$ be an arbitrary control input sequence. The dynamics (5.3) linearized about this trajectory gives

$$A(\mathbf{x}^0(t)) = \begin{bmatrix} 0 & 0 & -V\sin(\theta^0(t)) & 1 & 0 \\ 0 & 0 & V\cos(\theta^0(t)) & 0 & 1 \\ 0 & 0 & 0 & 0 & 0 \\ 0 & 0 & 0 & 0 & 0 \\ 0 & 0 & 0 & 0 & 0 \end{bmatrix} \tag{5.5}$$

$$C = \begin{bmatrix} 1 & 0 & 0 & 0 & 0 \\ 0 & 1 & 0 & 0 & 0 \end{bmatrix}.$$

For every τ and t, $A(t)$ and $\int_\tau^t A(\sigma)\mathrm{d}\sigma$ commute, therefore, the state transition matrix can be written as

$$\Phi(t) = I + \int_0^t A(\sigma)\mathrm{d}\sigma. \tag{5.6}$$

Although $\Phi(t)$ cannot be integrated for arbitrary $\theta^0(\sigma)$, note that the (1,3) entry

of $\Phi(t)$ is simply equal to the negative of the east component of the dead-reckoning trajectory in the wind-free frame, which is denoted z_2. Similarly, $\Phi_{2,3}(t)$ is equal to the north component of the trajectory, denoted z_1. The observability Gramian can be assembled as

$$W(t_f) = \int_0^{t_f} \begin{bmatrix} 1 & 0 & -z_2 & t & 0 \\ 0 & 1 & z_1 & 0 & t \\ -z_2 & z_1 & z_1^2 + z_2^2 & -tz_2 & tz_1 \\ t & 0 & -tz_2 & t^2 & 0 \\ 0 & t & tz_1 & 0 & t^2 \end{bmatrix} \mathrm{d}t, \tag{5.7}$$

where the time dependence of $z(t)$ is dropped for compactness.

Each of the entries in $W(t_f)$ represent interesting geometric properties of the trajectory in the wind-free frame. Specifically, $\int_0^{t_f} z_i(t)\mathrm{d}t = t_f \bar{z}_i$, where $\bar{z}_i$, $i \in \{1, 2\}$, is the trajectory centroid in the z_i direction, $\int_0^{t_f} z_1(t)^2 + z_2(t)^2 \mathrm{d}t = I_z$ is the polar inertia of the trajectory, and $\int_0^{t_f} t z_i(t)\mathrm{d}t = S_{z_j}$, where S_{z_j}, $j \in \{1, 2\}$ $j \neq i$, is the first moment of the trajectory with mass t about the z_j axis. In terms of these geometric properties, the observability Gramian is

$$W(t_f) = \begin{bmatrix} t_f & 0 & -t_f \bar{z}_2 & \frac{1}{2}t_f^2 & 0 \\ 0 & t_f & t_f \bar{z}_1 & 0 & \frac{1}{2}t_f^2 \\ -t_f \bar{z}_2 & t_f \bar{z}_1 & I_z & -S_{z_1} & S_{z_2} \\ \frac{1}{2}t_f^2 & 0 & -S_{z_1} & \frac{1}{3}t_f^3 & 0 \\ 0 & \frac{1}{2}t_f^2 & S_{z_2} & 0 & \frac{1}{3}t_f^3 \end{bmatrix} \tag{5.8}$$

The trajectory geometric properties in (5.8) cannot all be independently specified. However, note that wind vector magnitude and direction can be determined through simple vector subtraction if all inertial information is known, which leads to the assumption that if all inertial information can be optimally observed, then wind speed

and direction are also optimally observed.

Assumption 1. *Trajectories that optimize the observability of the inertial position and heading also optimize the observability of the wind speed and direction.*

Under this assumption, only the first three rows and columns of (5.8) need be considered, which are denoted $W_{1:3}$. Computing the eigenvalues of $W_{1:3}$ yields

$$\lambda = \begin{bmatrix} t_f \\ \frac{I_z+t_f}{2} + \frac{1}{2}\sqrt{I_z^2 - 2I_z t_f + t_f^2 + 4\bar{z}_1^2 + 4\bar{z}_2^2} \\ \frac{I_z+t_f}{2} - \frac{1}{2}\sqrt{I_z^2 - 2I_z t_f + t_f^2 + 4\bar{z}_1^2 + 4\bar{z}_2^2} \end{bmatrix}. \tag{5.9}$$

This set of eigenvalues has two possible minimum eigenvalues:

$$\lambda_{\min} = \min\left\{ t_f, \frac{I_z + t_f}{2} - \frac{1}{2}\sqrt{I_z^2 - 2I_z t_f + t_f^2 + 4\bar{z}_1^2 + 4\bar{z}_2^2} \right\}. \tag{5.10}$$

Because t_f will always increase with the estimation time horizon, only the second possibility is of interest. The minimum eigenvalue will achieve a maximum when it is stationary with respect to the trajectory variables, $\bar{z}_1$, $\bar{z}_2$, and I_z. Calculating the derivatives with respect to each variable gives:

$$\begin{bmatrix} \frac{\partial}{\partial \bar{z}_1} \\ \frac{\partial}{\partial \bar{z}_2} \\ \frac{\partial}{\partial I_z} \end{bmatrix} \lambda_{\min} = \begin{bmatrix} \frac{-2\bar{z}_1}{\sqrt{I_z^2 - 2I_z t_f + t_f^2 + 4\bar{z}_1^2 + 4\bar{z}_2^2}} \\ \frac{-2\bar{z}_2}{\sqrt{I_z^2 - 2I_z t_f + t_f^2 + 4\bar{z}_1^2 + 4\bar{z}_2^2}} \\ \frac{1}{2} + \frac{t_f - I_z}{2\sqrt{I_z^2 - 2I_z t_f + t_f^2 + 4\bar{z}_1^2 + 4\bar{z}_2^2}} \end{bmatrix}. \tag{5.11}$$

The critical point of (5.9) where the derivative vanishes occurs when $\bar{z}_1 = \bar{z}_2 = 0$. Therefore, the trajectory that maximizes the minimum eigenvalue of $W_{1:3}$ is symmetric about the starting point of the trajectory in the (z_1, z_2) plane. Substituting $\bar{z}_1 = \bar{z}_2 =$

0 into (5.9) yields the optimal eigenvalues

$$\lambda^* = \begin{bmatrix} t_f & t_f & I_z \end{bmatrix}^T. \tag{5.12}$$

Because I_z is a free parameter in the problem, it can be selected to minimize the condition number of $W_{1:3}$, which yields $I_z = t_f$.

5.2.3 Optimal trajectory

Having solved for the geometric characteristics of the optimal trajectory, the optimal control inputs can be derived.

Theorem 3 (Optimal Wind Identification Trajectory)**.** *The control input:*

$$u^*(t) = \begin{cases} \frac{4\pi}{t_f} & t < t_f/2 \\ -\frac{4\pi}{t_f} & t \geq t_f/2 \end{cases} \tag{5.13}$$

will produce a trajectory that optimizes the observability of wind speed and direction for system (5.3).

Proof. The control inputs yield a trajectory in the (z_1, z_2) plane:

$$z_1^*(t) = \frac{V t_f}{4\pi} \sin\left(\frac{4\pi t}{t_f}\right)$$
$$z_2^*(t) = \begin{cases} \frac{V t_f}{4\pi}\left(1 - \cos\left(\frac{4\pi t}{t_f}\right)\right) & t < t_f/2 \\ \frac{V t_f}{4\pi}\left(\cos\left(\frac{4\pi t}{t_f}\right) - 1\right) & t \geq t_f/2 \end{cases},$$

which has a centroid of $\bar{z}_1^* = \bar{z}_2^* = 0$. Therefore it is a stationary point of (5.9), and the minimum eigenvalue of $W_{1:3}$ is maximized. Furthermore, if the estimation time horizon is selected to be $t_f = \frac{2\sqrt{2}\pi}{V}$, then the trajectory polar moment of inertia is given by $I_z^* = \int_0^{t_f} (z_1^*(t)^2 + z_2^*(t)^2) = \frac{2\sqrt{2}\pi}{V}$, and the optimal eigenvalues (5.12) are all

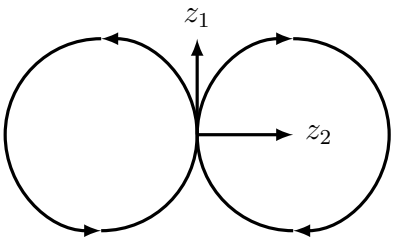

Figure 5.2: Optimal figure-eight trajectory for identification of a uniform flow field.

equal to $\frac{2\sqrt{2}\pi}{V}$. Therefore, the condition number of $W_{1:3}$ is one, and the heading angle can be computed with arbitrary accuracy. Finally, under Assumption 1, the wind speed and direction observability are maximized. □

The optimal trajectory takes the form of a "figure-eight" in the (z_1, z_2) plane, as depicted in Fig. 5.2. If the estimation time horizon is selected as $t_f = \frac{2\sqrt{2}\pi}{V}$, then the optimal control magnitude is $\omega = \sqrt{2}V$, which yields a turning radius of $r = \frac{1}{\sqrt{2}}$. If this value of ω is greater than the maximum allowable control input, then the optimal input consists of bang-bang controls (switching between maximum and minimum magnitudes). The bang-bang control scheme still maximizes the minimum eigenvalue of $W_{1:3}$, and the condition number of $W_{1:3}$ is equal to $\frac{8\pi^2}{V^2 t_f^2}$ for $\frac{4\pi}{t_f} = \omega \leq \sqrt{2}V$, which approaches 1 as t_f approaches $\frac{2\sqrt{2}\pi}{V}$.

The optimal figure-eight trajectory pictured in Fig. 5.2 shows the vehicle starting with a north heading. However, the optimal trajectory is invariant under rotation and reflection, which indicates that the optimal control input (5.13) generates an observability-optimal trajectory independent of the initial vehicle orientation. Furthermore, the optimal trajectory can be shown to be the time-optimal solution to the observability-based guidance problem, generating an observability-optimal solution with minimum path length [58].

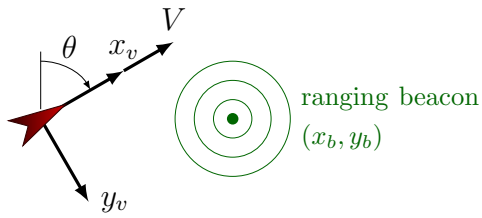

Figure 5.3: Beacon position described in the vehicle-fixed frame.

5.3 Range-only Localization

In range-only localization, the vehicle has range measurements to a static beacon with known position. It is also assumed that the vehicle has inertial orientation measurements (*e.g.*, from a compass). Because the vehicle heading, θ, is measured directly, the vehicle dynamics (5.2) are rewritten as beacon position dynamics in a vehicle-centric frame with turn rate input to get

$$\begin{aligned} \frac{\mathrm{d}}{\mathrm{d}t}\begin{bmatrix} x_b \\ y_b \end{bmatrix} &= \begin{bmatrix} -V \\ 0 \end{bmatrix} + \begin{bmatrix} y_b \\ -x_b \end{bmatrix} \omega \\ y &= \frac{1}{2}(x_b^2 + y_b^2), \end{aligned} \tag{5.14}$$

where (x_b, y_b) is the position of the beacon in the vehicle-fixed frame, as depicted in Fig. 5.3.

5.3.1 Observability analysis

Nonlinear observability analysis is applied to the unicycle dynamics with range-only measurements (5.14). The nonlinear observability matrix is given by

$$\mathrm{d}\mathcal{O} = \frac{\partial}{\partial \mathbf{x}}\begin{bmatrix} \mathbf{h} \\ L_{\mathbf{f}_0}\mathbf{h} \end{bmatrix} = \begin{bmatrix} x_b & y_b \\ -V & 0 \end{bmatrix}, \tag{5.15}$$

which is full rank as long as $Vy_b \neq 0$. As a note, the Lie derivative with respect to the control vector field, $L_{\mathbf{f}_1}\mathbf{h}$, is identically zero, therefore turning input does not alter system observability. The observability matrix drops rank under two conditions: if $V \neq 0$ (*i.e* the vehicle is not moving) or if $y_b = 0$ (*i.e.*, the vehicle heading is aligned with the beacon). The first case ($V = 0$) causes the system to be unobservable because a single range measurement does not uniquely localize the vehicle. The second case ($y_b = 0$) causes $\mathrm{d}\mathcal{O}$ to drop rank because the system evolves on a lower-dimensional manifold when the beacon is aligned with the vehicle heading. In this scenario, the lower-dimensional dynamics are given by

$$\begin{aligned} \dot{x}_b &= \pm V \\ y &= \frac{1}{2}x_b^2, \end{aligned} \tag{5.16}$$

where the sign of V is determined by the vehicle heading. These lower-dimensional dynamics are still locally observable, therefore, system (5.14) is everywhere locally observable if the vehicle is moving with non-zero speed.

Although the system is locally observable during straight-path motions, the observability matrix is poorly conditioned when the vehicle heading is nearly aligned with the landmark due to the symmetry in the range-only navigation problem, as depicted in Fig. 5.4. Straight paths are indistinguishable from a path mirrored about the landmark, and the close proximity of two indistinguishable paths results in an ill-conditioned estimation problem.

5.3.2 Optimal trajectory

Similar to the procedure employed for flow field identification in Section 5.2, the observability Gramian for range-only localization can be computed in closed-form as a function of the vehicle trajectory. Linearizing system (5.14) about an arbitrary

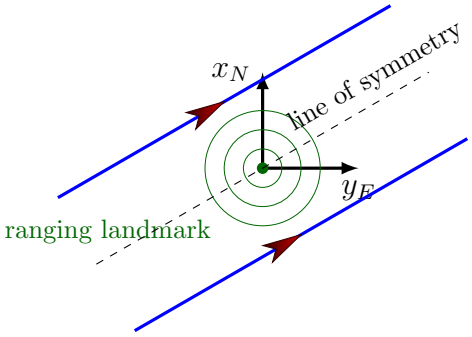

Figure 5.4: The symmetry in the range-only navigation problem causes straight line paths to be indistinguishable from their mirrored transformation about a parallel line through the landmark.

input $u^0(t) = \omega(t)$ and state trajectory $(x_b^0(t), y_b^0(t))$ results in the LTV system

$$\begin{aligned} \frac{\mathrm{d}}{\mathrm{d}t}\begin{bmatrix}\tilde{x}_b \\ \tilde{y}_b\end{bmatrix} &= \begin{bmatrix} 0 & u^0(t) \\ -u^0(t) & 0 \end{bmatrix}\begin{bmatrix}\tilde{x}_b \\ \tilde{y}_b\end{bmatrix} \\ \tilde{y} &= \begin{bmatrix} x_b^0(t) & y_b^0(t)\end{bmatrix}\begin{bmatrix}\tilde{x}_b \\ \tilde{y}_b\end{bmatrix}. \end{aligned} \tag{5.17}$$

The corresponding state transition matrix is given by

$$\Phi(t) = \begin{bmatrix} \cos\theta^0(t) & \sin\theta^0(t) \\ -\sin\theta^0(t) & \cos\theta^0(t) \end{bmatrix}, \tag{5.18}$$

where $\theta^0(t)$ is the vehicle heading over the linearization trajectory. Computing the observability Gramian as a function of the linearization trajectory gives

$$W(t_f) = \int_0^{t_f} \begin{bmatrix} x_N^2(t) & x_N(t)y_E(t) \\ x_N(t)y_E(t) & y_E^2(t) \end{bmatrix} \mathrm{d}t, \tag{5.19}$$

where $(x_N(t), y_E(t))$ is the nominal trajectory of the vehicle relative to the beacon in the inertial frame. Therefore, the observability Gramian is an explicit function of the inertial vehicle trajectory, which can be computed to optimize the eigenvalues of the observability Gramian.

Theorem 4 (Optimal Range-Only Localization Trajectory)**.** *A circular trajectory centered at the beacon with radius* ρ

$$\begin{bmatrix} x_N(t) \\ y_E(t) \end{bmatrix} = \begin{bmatrix} \rho\cos(2\pi t/t_f) \\ \rho\sin(2\pi t/t_f) \end{bmatrix} \qquad t \in \begin{bmatrix} 0 & t_f \end{bmatrix}$$

will minimize the condition number of the observability Gramian for the range-only localization system (5.14).

Proof. The trajectory gives the observability Gramian

$$W(t_f) = \begin{bmatrix} t_f\rho^2/(2\pi) & 0 \\ 0 & t_f\rho^2/(2\pi) \end{bmatrix}$$

which has a condition number of one, and maximizes the observability of the inertial position given range measurements to a single beacon. □

The optimal trajectory is a somewhat unintuitive result. A circular trajectory centered at the ranging beacon will yield constant measurements, which would seem to provide poor information about the vehicle position. However, with knowledge of the circular trajectory, the vehicle position can be uniquely determined with the radius of the circle (range measurement) and the vehicle heading.

5.4 Bearing-only Localization

Similar to the case of range-only localization presented in Section 5.3, the bearing-only localization problem assumes bearing measurements to a static beacon and inertial

orientation measurements. Using the beacon dynamics in the vehicle-centric frame (see Fig. 5.3), the bearing-only localization dynamics are given by

$$\begin{gathered}\frac{\mathrm{d}}{\mathrm{d}t}\begin{bmatrix} x_b \\ y_b \end{bmatrix} = \begin{bmatrix} -V \\ 0 \end{bmatrix} + \begin{bmatrix} y_b \\ -x_b \end{bmatrix} \omega \\ y = \tan^{-1}(y_b/x_b),\end{gathered} \tag{5.20}$$

where (x_b, y_b) is the position of the beacon in the vehicle-fixed frame, as depicted in Fig. 5.3.

5.4.1 Observability analysis

Nonlinear observability analysis is applied to the unicycle dynamics with bearing-only measurements (5.20). The nonlinear observability matrix is given by

$$\mathrm{d}\mathcal{O} = \frac{\partial}{\partial \mathbf{x}}\begin{bmatrix} \mathbf{h} \\ L_{\mathbf{f}_0}\mathbf{h} \end{bmatrix} = \frac{1}{x_b^2 + y_b^2}\begin{bmatrix} -y_b & x_b \\ \frac{-V x_b y_b}{x_b^2+y_b^2} & \frac{V(x_b^2-y_b^2)}{x_b^2+y_b^2} \end{bmatrix}, \tag{5.21}$$

which has the determinant

$$\det(\mathrm{d}\mathcal{O}) = \frac{V y_b}{(x_b^2 + y_b^2)^2}. \tag{5.22}$$

Therefore, the observability matrix is full rank if $V \neq 0$ (*i.e.*, the vehicle is moving) and $y_b \neq 0$ (*i.e.*, the beacon is not aligned with the vehicle heading). As a note, the Lie derivative with respect to the control vector field, $L_{\mathbf{f}_1}\mathbf{h}$, is equal to -1, which contains no state information and does not increase the span of $\mathcal{O}$. Thus, turn rate input does not alter the observability of system (5.20). Just as in the range-only case, vehicle position is unobservable using bearing measurements if the vehicle is not moving ($V = 0$). When the beacon position is aligned with the vehicle heading

($y_b = 0$), the vehicle dynamics evolve on a a lower-dimensional manifold given by

$$\begin{aligned} \dot{x}_b &= \pm V \\ y &= 0, \end{aligned} \tag{5.23}$$

which are unobservable. Thus, inertial position is observable using bearing measurements to a static beacon if the vehicle is moving with non-zero speed and the beacon position is not aligned with the vehicle heading.

5.4.2 Optimal trajectory

The observability-optimal trajectory is derived by again considering the linearization of the nonlinear dynamics (5.20) about an arbitrary trajectory $(\mathbf{x}^0(t), \mathbf{u}^0(t))$. Let $u^0(t) = \omega(t)$ and $(x_b^0(t), y_b^0(t))$ be the linearization input and state trajectory, then the linearized dynamics are given by (dropping the $(\cdot)^0$ nomenclature for clarity)

$$\begin{aligned} \frac{\mathrm{d}}{\mathrm{d}t}\begin{bmatrix} \tilde{x}_b \\ \tilde{y}_b \end{bmatrix} &= \begin{bmatrix} 0 & u(t) \\ -u(t) & 0 \end{bmatrix}\begin{bmatrix} \tilde{x}_b \\ \tilde{y}_b \end{bmatrix} \\ \tilde{y} &= \frac{1}{x_b^2(t) + y_b^2(t)}\begin{bmatrix} -y_b(t) & x_b(t) \end{bmatrix}\begin{bmatrix} \tilde{x}_b \\ \tilde{y}_b \end{bmatrix}. \end{aligned} \tag{5.24}$$

The corresponding state transition matrix is equivalent to the range measurement case, given by

$$\Phi(t) = \begin{bmatrix} \cos\theta^0(t) & \sin\theta^0(t) \\ -\sin\theta^0(t) & \cos\theta^0(t) \end{bmatrix}, \tag{5.25}$$

where $\theta^0(t)$ is the vehicle heading over the linearization trajectory. Computing the observability Gramian in terms of the linearization trajectory yields the expression

$$W(t_f) = \int_0^{t_f} \frac{1}{(x_N^2 + y_E^2)^2}\begin{bmatrix} y_E^2(t) & -x_N(t)y_E(t) \\ -x_N(t)y_E(t) & x_N^2(t) \end{bmatrix}\mathrm{d}t, \tag{5.26}$$

where $(x_N(t), y_E(t))$ is the vehicle linearization trajectory relative to the beacon in the inertial frame. The form of the observability Gramian for bearing measurements is very similar to the form for range measurements (5.19). As a consequence, the observability-optimal trajectory takes the form of a circle, which is proven in the following theorem.

Theorem 5 (Optimal Bearing-Only Localization Trajectory)**.** *A circular trajectory centered at the beacon with radius* ρ

$$\begin{bmatrix} x_N(t) \\ y_E(t) \end{bmatrix} = \begin{bmatrix} \rho\cos(2\pi t/t_f) \\ \rho\sin(2\pi t/t_f) \end{bmatrix} \qquad t \in \begin{bmatrix} 0 & t_f \end{bmatrix}$$

will minimize the condition number of the observability Gramian for the bearing-only localization system (5.20).

Proof. The trajectory gives the observability Gramian

$$W(t_f) = \begin{bmatrix} t_f/(2\pi\rho^2) & 0 \\ 0 & t_f/(2\pi\rho^2) \end{bmatrix}$$

which has a condition number of one, and maximizes the observability of the inertial position given bearing measurements to a single beacon. □

Interestingly, the optimal trajectory is identical to the optimal range-only localization trajectory provided in Theorem 4. Because the range and bearing measurements are complementary, sampling one measurement along the circular trajectory enables optimal observability of the other state. Although the trajectory produces observability Gramians with unity condition number for both sensing modalities, the eigenvalues of the two Gramians have different relationships with the radius ρ of the circular trajectory. The eigenvalues of the observability Gramian for range-only localization are proportional to ρ^2, while the eigenvalues for bearing-only localization are *inversely*

proportional to ρ^2. Thus, to increase the volume of the observation ellipsoid, larger radius trajectories should be used in range-only localization, while smaller radius trajectories should be used in bearing-only localization.

5.5 Generalization to Higher-Dimensional Nonholonomic Systems

The results of the previous sections considered the unicycle model for a nonholonomic vehicle, using the geometry of the linearization trajectories to compute observability measures. Interestingly, the observability-based trajectory generation generalizes to higher-dimensional nonholonomic systems [100]. In this section, the unicycle model of robotic motion (which is a first-order nonholonomic system with three states) is generalized to more general first-order nonholonomic systems in canonical form,

$$\begin{aligned} \dot{\mathbf{x}} &= \mathbf{u} \\ \dot{z}_{ij} &= x_i u_j - x_j u_i \quad \forall\, i,j \in \{1,2,\ldots,m\},\ i > j, \end{aligned} \tag{5.27}$$

where $\mathbf{x} \in \mathbb{R}^m$ ($m \geq 2$) are the holonomic states, $\mathbf{z} \in \mathbb{R}^{m(m-1)/2}$ are the nonholonomic states, and $\mathbf{u} \in \mathbb{R}^m$ are the controls.

This type of system was studied in the context of geometric and optimal control by Brockett [101] and later by Murray and Sastry [102]. This class of systems has practical importance for several reasons. First, these systems exhibit fundamental challenges due to the nonholonomic constraints which form the most basic, but interesting nonlinearity. Second, many systems of engineering interest are diffeomorphic to the nonholonomic integrator (*e.g.*, the unicycle model just studied, or robotic grasping models). Finally, the properties of the nonholonomic integrator give insight into systems with higher complexity.

5.5.1 Observability analysis

The class of systems described by (5.27) are first-order Lie bracket controllable, meaning that the control Lie algebra constructed by the control vector fields and their first-order Lie brackets is full rank. Because the Lie brackets are necessary to guarantee full rank of the control Lie algebra, switching or area-generating controls must be used to steer the system from an initial configuration to an arbitrary final configuration. These systems also have interesting observability characteristics. Consider the case when system (5.27) has an output function $\mathbf{y} = \mathbf{z}$. Taking Lie derivatives of the output, we see that $L_{\mathbf{f}_i} z_{ij} = -x_j$ and $L_{\mathbf{f}_j} z_{ij} = x_i$, therefore x_i and x_j are observable with measurements of z_{ij} and use of the controls u_i and u_j. This result leads to the following theorems.

Theorem 6 (Canonical Form Observability)**.** *First-order nonholonomic systems in canonical form (5.27) are observable if and only if measurements of the nonholonomic states* $\mathbf{z}$ *are available.*

Proof. If all nonholonomic states are measured, then the observability Lie algebra is $\mathcal{O} = \text{span}\{z_{ij}, -x_j, x_i\}\ \forall\ i, j \in \{1, 2, \ldots, m\},\ i > j$, and $\text{rank}(d\mathcal{O}) = m(m+1)/2 = \dim(\mathbf{x}) + \dim(\mathbf{z})$, therefore the system is observable if all $\mathbf{z}$ states are measured and control actuation is utilized. Now, assume that one nonholonomic state z_{kl} is not measured. Because z_{kl} does not appear in the control vector fields, it will not be observable, and $\text{rank}(d\mathcal{O}) \leq m(m+1)/2 - 1$, thus the system will be unobservable. □

Theorem 7 (Actuation Required for Observability)**.** *System (5.27) with output* $\mathbf{y} = \mathbf{z}$ *is observable if and only if actuation in at least two control channels is utilized.*

Proof. The Lie derivative of one output with respect to a control vector field is

$$L_{\mathbf{f}_k} z_{ij} = \begin{cases} -x_j & k = i \\ x_i & k = j \\ 0 & \text{otherwise.} \end{cases}$$

Because all outputs $z_{ij}\ \forall\ i, j \in \{1, 2, \ldots, m\},\ i > j$ are measured, the span of the Lie derivative of all outputs with respect to a control vector field is $\text{span}\{L_{\mathbf{f}_i}\mathbf{z}\} = \text{span}\{x_j\}\ \forall\ j \neq i$, which spans all $\mathbf{x}$ states except x_i. Therefore, any two control vector fields $\mathbf{f}_k$ and $\mathbf{f}_l$, $k \neq l$, have Lie derivatives that span all $\mathbf{x}$ states, and the system is observable with a minimum of two control inputs. □

Corollary 1. *If all* $\mathbf{z}$ *states are measured and one* x_i *state is measured, then actuation in* u_i *will give an observable system.*

5.5.2 Optimal trajectory

The first-order nonholonomic system in canonical form (5.27) can be rewritten as a bilinear system without loss of generality to facilitate the observability-based trajectory optimization process:

$$\begin{aligned} \dot{\mathbf{x}} &= \mathbf{u} \\ \dot{\mathbf{z}} &= F(\mathbf{u})\mathbf{x} \\ \mathbf{y} &= \mathbf{z}. \end{aligned} \tag{5.28}$$

The matrix $F(\mathbf{u}) \in \mathbb{R}^{m(m-1)/2 \times m}$ consists of $m - 1$ blocks,

$$F(\mathbf{u}) = \begin{bmatrix} F_1(\mathbf{u})^T & F_2(\mathbf{u})^T & \ldots & F_{m-1}(\mathbf{u})^T \end{bmatrix}^T, \tag{5.29}$$

where each block $F_i(\mathbf{u}) \in \mathbb{R}^{(m-i)\times m}$ is given by

$$F_i(\mathbf{u}) = \begin{bmatrix} \mathbf{0}_{(i-1)} & u_{i+1} & -u_i & 0 & \dots & 0 \\ \mathbf{0}_{(i-1)} & u_{i+2} & 0 & -u_i & \dots & 0 \\ \vdots & \vdots & \vdots & \vdots & \ddots & \vdots \\ \mathbf{0}_{(i-1)} & u_m & 0 & 0 & \dots & -u_i \end{bmatrix}, \tag{5.30}$$

and $\mathbf{0}_{(i-1)}$ is a row vector of zeros of length $(i-1)$. As an example, when the length of $\mathbf{u}$ is three, $F(\mathbf{u})$ is given by

$$F(\mathbf{u}) = \begin{bmatrix} u_2 & -u_1 & 0 \\ u_3 & 0 & -u_1 \\ 0 & u_3 & -u_2 \end{bmatrix}. \tag{5.31}$$

Because the nonholonomic states $\mathbf{z}$ are directly measured, the goal of the trajectory optimization is to optimize the observability Gramian associated with the holonomic states $\mathbf{x}$. Integrating to determine the output at time t gives

$$\begin{aligned} \mathbf{y}(t) &= \mathbf{z}_0 + \int_0^t F(\mathbf{u}(\tau))\mathbf{x}(\tau)\mathrm{d}\tau \\ &= \mathbf{z}_0 + \int_0^t F(\mathbf{u}(\tau_1)) \left(\mathbf{x}_0 + \int_0^{\tau_1} \mathbf{u}(\tau_2)\mathrm{d}\tau_2 \right) \mathrm{d}\tau_1. \end{aligned} \tag{5.32}$$

Now, collect the terms influenced by the unknown initial condition of the holonomic states, and define a new output

$$\begin{aligned} \eta &= \mathbf{y} - \left[\mathbf{z}_0 + \int_0^t F(\mathbf{u}(\tau_1)) \left(\int_0^{\tau_1} \mathbf{u}(\tau_2)\mathrm{d}\tau_2 \right) \mathrm{d}\tau_1 \right] \\ &= \int_0^t F(\mathbf{u}(\tau_1))\mathrm{d}\tau_1\mathbf{x}_0 = F\left(\int_0^t \mathbf{u}(\tau_1)\mathrm{d}\tau_1 \right) \mathbf{x}_0. \end{aligned} \tag{5.33}$$

For notational simplicity, define $\xi(t) = \int_0^t \mathbf{u}(\tau_1)\mathrm{d}\tau_1$. The output energy associated with holonomic states is now

$$\begin{aligned} \|\eta(t)\| &= \mathbf{x}_0^T \int_0^{t_f} F(\xi(t))^T F(\xi(t))\mathrm{d}t\mathbf{x}_0 \\ &= \mathbf{x}_0^T W_{\mathbf{x}}(0, t_f)\mathbf{x}_0, \end{aligned} \tag{5.34}$$

where $W_{\mathbf{x}}(0, t_f)$ is the observability Gramian associated with the holonomic states. Expanding the terms inside the integral gives

$$\left(F(\xi)^T F(\xi)\right)_{ij} = \begin{cases} -\xi_i \xi_j & i \neq j \\ \sum\limits_{l \neq i} \xi_l^2 & i = j \end{cases}. \tag{5.35}$$

Based on the form of (5.35), the observability-optimal trajectory is computed using the following theorem.

Theorem 8 (Optimal Nonholonomic Integrator Trajectory)**.** *Cyclic controls of the form*

$$u_j^\star(t) = \frac{2\pi j A_j}{t_f} \cos(2\pi j t/t_f),$$

and corresponding state trajectories

$$\xi_j^\star(t) = A_j \sin(2\pi j t/t_f) \quad \forall\, j \in \{1, 2, \ldots, m\}$$

allow placement of the observability Gramian eigenvalues over the time horizon t_f for first order nonholonomic systems in canonical form (5.27) with output $\mathbf{y} = \mathbf{z}$.

Proof. First, note that $\int_0^{t_f} \xi_i^\star(t)\xi_j^\star(t)\mathrm{d}t = 0$ and $\int_0^{t_f} \xi_i^\star(t)^2\mathrm{d}t = A_i^2 t_f/2$. Substituting

the optimal trajectory into (5.34), the ij entry of the observability Gramian is

$$(W_{\mathbf{x}}(0,t_f))_{ij} = \begin{cases} 0 & i \neq j \\ \sum_{l \neq i} A_l^2 t_f/2 & i = j \end{cases}.$$

Therefore, the observability Gramian is diagonalized, and the eigenvalues of $W_{\mathbf{x}}(0,t_f)$ can be placed using appropriate amplitudes A_j. □

Remark 1. *Note that the choice of integer j in the sinusoidal frequency is arbitrary. The integer j is used as the integer frequency multiplier for state ξ_j for convenience only, but any integer can be used such that no ξ_i and ξ_j have the same frequency.*

The desired observability Gramian eigenvalues form a set of equations that can be solved for the optimal state trajectory amplitudes. Extracting the diagonal of $W_{\mathbf{x}}(0,t_f)$ yields

$$\frac{t_f}{2}\left(\mathbf{1}\mathbf{1}^T - I\right)\mathbf{A}^2 = \lambda, \tag{5.36}$$

where $\mathbf{1}$ is a column vector of ones, $\mathbf{A}^2$ is a column vector of the amplitudes squared, and λ is a column vector of desired observability Gramian eigenvalues with λ_i representing the eigenvalue associated with the x_i state. Showing that $(\mathbf{1}\mathbf{1}^T - I)$ is a full-rank matrix is straightforward, therefore the solution for $\mathbf{A}^2$ always exists and is unique. Given a set of desired eigenvalues λ, the amplitudes $\mathbf{A}^2$ can be solved for explicitly. Subtracting the first equation of (5.36) from the remaining equations yields

$$A_i^2 = A_1^2 + \frac{2}{t_f}(\lambda_1 - \lambda_i) \quad \forall\, i \in \{2,3,\ldots,m\}. \tag{5.37}$$

Substituting these expressions back into the first equation and solving for A_1^2 and A_i^2 gives

$$A_i^2 = \frac{2}{t_f}\left(-\lambda_i + \frac{1}{(m-1)}\sum_{j=1}^{m}\lambda_j\right) \quad \forall\, i. \tag{5.38}$$

For this solution to be feasible the squared amplitudes must be positive, $A_i^2 \geq 0$, thus

$$0 < \lambda_i \leq \frac{1}{(m-2)} \sum_{j \neq i} \lambda_j \tag{5.39}$$

for a feasible solution. The constraint imposed by (5.39) essentially limits the spread of the eigenvalues of $W_{\mathbf{x}}(0, t_f)$. The case when all λ_i are equivalent (*i.e.*, a condition number of $\kappa(W_{\mathbf{x}}(0, t_f)) = 1$) is always a feasible. The feasible set of eigenvalues is the interior of a cone in the positive orthant with the vertex at the origin. When $m = 2$, the constraint (5.39) does not limit the choice of λ, and the feasible set is the entire positive orthant. When $m > 2$, the feasible space is enclosed by m hyperplanes passing through the origin with equations $-\lambda_i + 1/(m-2) \sum_{j \neq i} \lambda_j = 0$. As m increases, the cone becomes smaller, and in the limit $m \to \infty$, the cone reduces to the line of all λ_i equivalent. Practically speaking, the constraint (5.39) does not impose undesirable limitations on the choice of λ because a condition number of one is desirable and always feasible. Therefore, the observability Gramian eigenvalues can be nearly arbitrarily placed to control the estimation uncertainty.

As an example, consider calculation of the optimal trajectory for the case when $m = 3$. Suppose that observability Gramian eigenvalues of $\lambda = \begin{bmatrix} 50 & 50 & 50 \end{bmatrix}^T$ are desired over a time horizon of $t_f = 2$. Then using (5.38), the state trajectory amplitudes are

$$A_i = \sqrt{\left(-50 + \frac{1}{2}(150) \right)} = 5, \tag{5.40}$$

which results in an observability Gramian of $W_{\mathbf{x}}(0, 2) = \text{diag} \left\{ \begin{bmatrix} 50 & 50 & 50 \end{bmatrix} \right\}$. Note that the negative square root could also be chosen for the amplitude A_i (*i.e.*, -5) without loss of optimality. The resulting state trajectory would simply be mirrored in the i^{th} axis direction. The optimal trajectory traces a figure-eight in the state space, as shown in Fig. 5.5. It is shown here with the origin of the trajectory at the origin of the state space, but the optimal trajectory is translationally invariant, so

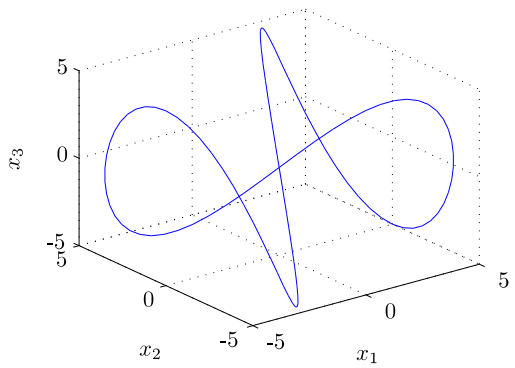

Figure 5.5: Observability-based guidance trajectory for a first-order nonholonomic system with three controls.

the initial position is arbitrary.

If, for example, estimates of x_1 are the most important, then the first eigenvalue of $W_{\mathbf{x}}(0, t_f)$ can be increased to *e.g.*, $\lambda = \begin{bmatrix} 75 & 50 & 50 \end{bmatrix}^T$ which yields state amplitudes of $\mathbf{A} = \begin{bmatrix} \sqrt{12.5} & \sqrt{37.5} & \sqrt{37.5} \end{bmatrix}^T$. To reduce the covariance of an estimate of state x_i, the control amplitude on u_i is decreased while the amplitudes on all other control channels are increased. This behavior is intuitive, because the output energy due to x_i is dependent on all control inputs except u_i.

5.6 Simulation Results

The observability-based trajectories generated in the previous sections were designed to optimize observability of vehicle states, as measured by the observability Gramian condition number and minimum eigenvalue. As demonstrated in Chapter 2, these measures of observability are closely related to estimation performance. The observability-based guidance trajectories are now demonstrated in simulation to improve estimation performance, enabling tuning of the estimation error and uncertainty via manipulation of the observability Gramian eigenvalues.

Simulations were performed in MATLAB using the `ode45` integration routine to in-

tegrate the unicycle dynamics (5.2). A discrete-time unscented Kalman filter (UKF) [27] was used to estimate system states from measurements. Two measures of estimation performance were tracked — the convergence time of the estimator, t_c, and the average steady-state estimation covariance, $\bar{\sigma}$. The convergence time is measured by

$$t_c = \arg\min\{\|\hat{\mathbf{x}}(t) - \mathbf{x}(t)\| \leq 0.05\|\hat{\mathbf{x}}(0) - \mathbf{x}(0)\|,\ \forall\ t \geq t_c\}, \tag{5.41}$$

which is the 5% settling time of the estimator dynamics. The average steady-state estimation covariance is computed as the average estimation covariance over the interval $t \geq t_c$. These two measures provided a means of comparison between estimation performance during different vehicle trajectories.

5.6.1 Wind estimation performance

Wind estimation was performed in simulation using the (unknown) wind speeds $W_x = 0.25$ m/s and $W_y = -0.15m/s$, with a vehicle flow-relative speed of $V = 1$ m/s. The vehicle position was initialized to the origin with an initial orientation $\theta = 30$ deg. Initial conditions for the state estimate were set to zero for all states. Estimation performance was compared for three different trajectories — the optimal figure-eight trajectory defined by Theorem 3, a suboptimal trajectory defined by $u(t) = \frac{4\pi}{t_f} sin(4\pi t/t_f)$, and an unobservable straight-line trajectory. The simulation results for these three trajectories are shown in Fig. 5.6. The optimal trajectory provides 47% faster convergence of the UKF and 7% lower steady-state estimation covariance compared to the suboptimal trajectory.

5.6.2 Range and bearing estimation performance

The range-only and bearing-only navigation problems were simulated using the optimal circular trajectory defined in Theorems 4 and 5. As a comparison, straight-line trajectories were also simulated. The navigation beacon was placed at the origin of

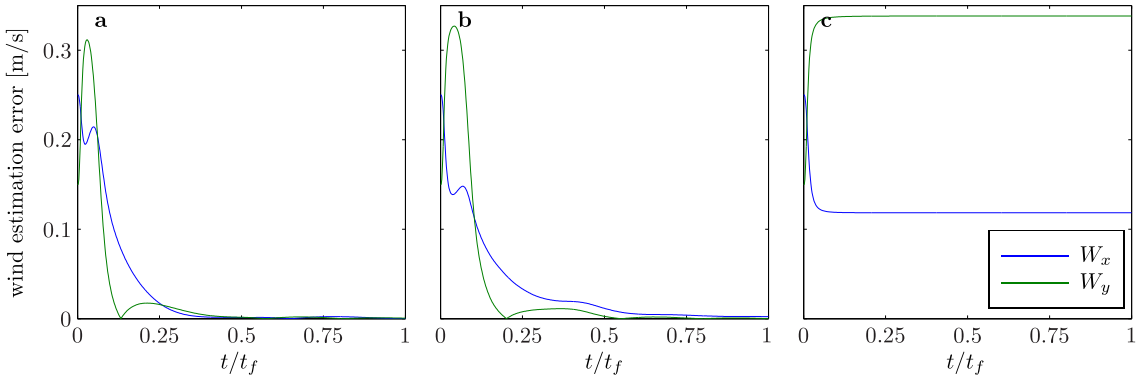

Figure 5.6: Wind estimation results for (a) the observability-optimal trajectory, (b) a suboptimal trajectory, and (c) an unobservable straight-line trajectory. The optimal trajectory provides faster estimator convergence and lower steady-state covariance when compared to a sub-optimal trajectory. As proven in Theorem 2, the straight-line trajectory results in unobservable wind speed.

the inertial reference frame, and the vehicle was initialized to $(x_N, y_E) = (0, 1)$ m with and initial heading of $\theta = 0$ deg. Vehicle speed was set to $V = 1$ m/s and the vehicle followed a circular trajectory with radius $\rho = 1$ m. Estimation results are shown in Fig. 5.7 and 5.8 for navigation using range and bearing measurements, respectively. In the case of range-only measurements, the optimal trajectory provides much faster convergence than the straight-line trajectory, which does not reach the 5% convergence boundary before the end of the simulation. The straight-line trajectory produces a slow eigenvalue in the estimator dynamics, which causes the estimate of y_b to converge very slowly. The bearing-only guidance trajectories produce similar results, with 61% faster convergence time and 50% lower steady-state covariance for the optimal circular trajectory.

Because the range-only navigation problem exhibits a symmetry (see Fig. 5.4), straight-line paths that are nearly aligned with the beacon are difficult to observe. This geometric observation is supported by the structure of the observability Gramian for range-only navigation (5.19), which becomes singular when the beacon is aligned

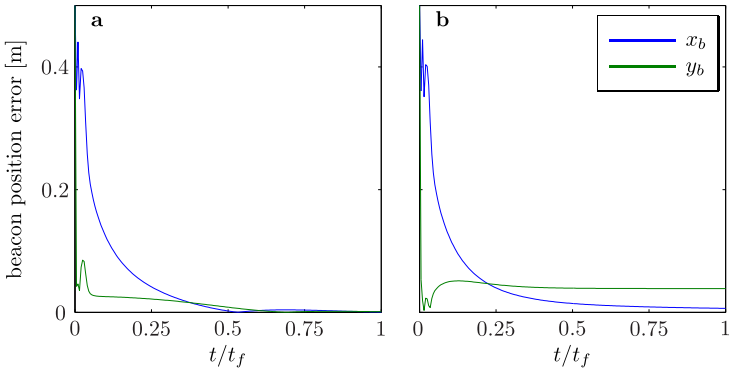

Figure 5.7: Comparison of range-only navigation estimation results for (a) the observability-optimal circular trajectory and (b) a suboptimal straight-line trajectory.

with the trajectory. A simulation study was performed to better examine the effect of the symmetry on the estimation problem. Straight-line trajectories were simulated with varying initial distance from the line of symmetry, as pictured in Fig. 5.9.

The steady-state covariance for range-only and bearing-only navigation was computed for the parameter δ varying between 0.01 and 0.5, as shown in Fig, 5.10. Estimation covariance for range-only navigation shows a monotonic decrease with distance from the line of symmetry, which is consistent with the variation in the observability Gramian eigenvalues as a function of distance from the beacon.

Conversely, the estimation covariance for bearing-only navigation shows a non-monotonic relationship with the distance from the line of symmetry. Navigation with bearing-only measurements does not exhibit the same symmetry as navigation with range-only measurements, however, the vehicle position is unobservable with bearing-only measurements if the beacon is aligned with the vehicle trajectory. The estimation covariance for bearing-only navigation increases with distance from the beacon, which is consistent with the variation in the observability Gramian eigenvalues. The covariance also increases very near the beacon due to the unobservability when the beacon

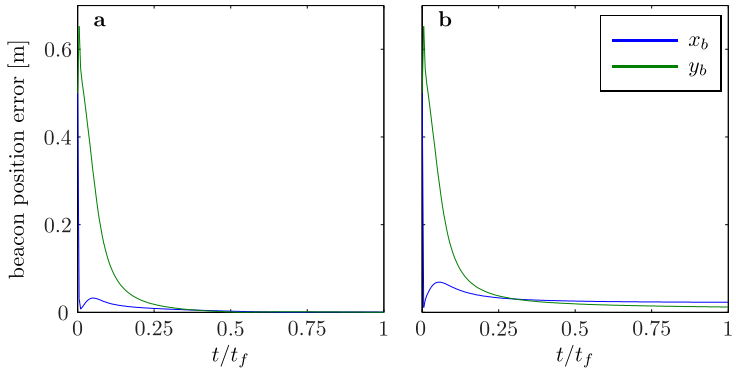

Figure 5.8: Comparison of bearing-only navigation estimation results for (a) the observability-optimal circular trajectory and (b) a suboptimal straight-line trajectory.

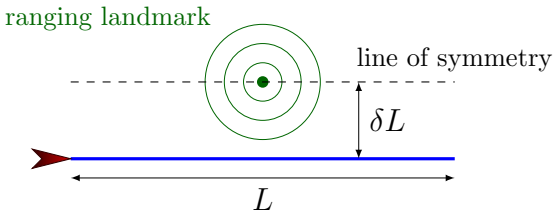

Figure 5.9: Straight-line trajectories were simulated to determine the effect of navigational symmetry on the estimation performance. Initial positions for the vehicle were controlled by the parameter δ to vary the distance from the line of symmetry.

is aligned with the vehicle path. The results of the symmetry study indicate that estimation covariance can be significantly reduced (*e.g.*, more than 60% reduction for $\delta = 0.5$ compared to $\delta = 0.01$) for range-only navigation by steering the vehicle along paths that pass further from the line of symmetry.

5.6.3 Nonholonomic integrator estimation performance

The simulation study concludes with evaluation of estimation performance for optimal trajectories of a higher-dimensional nonholonomic system. Because the structure

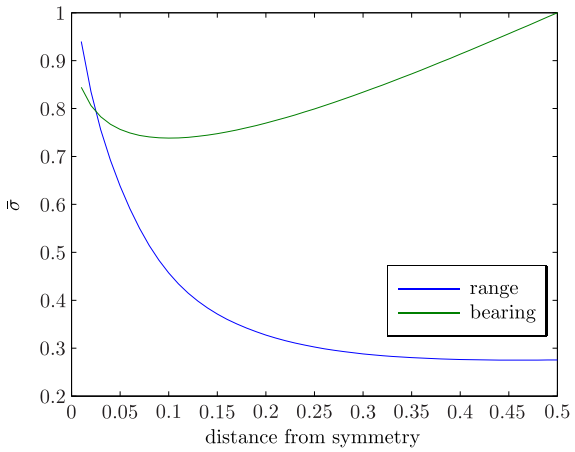

Figure 5.10: Variation in steady-state estimation covariance (normalized by the maximum covariance) as a function of distance from the line of symmetry for range-only and bearing-only measurements.

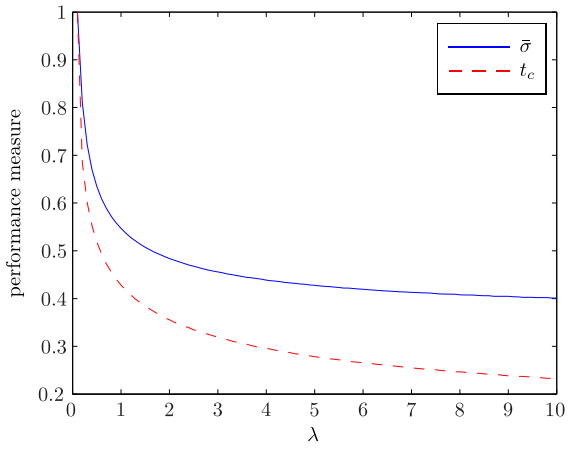

Figure 5.11: Variation in steady-state estimation covariance (normalized by the maximum covariance) and estimation convergence time (normalized by the maximum time) as a function of the prescribed observability Gramian eigenvalues.

of the nonholonomic integrator permits almost arbitrary placement of observability Gramian eigenvalues by the trajectories defined in Theorem 8, the direct effect of

observability Gramian eigenvalues on estimation performance could be determined. The nonholonomic integrator dynamics (5.27) were integrated for $m = 2$ controls for observability-optimal trajectories with different prescribed eigenvalues. The optimal trajectories were computed according to Theorem 8 for eigenvalues prescribed to be all equivalent (*i.e.*, condition number of one) and magnitude ranging from 0.1 to 10. The resulting estimation covariances and estimator convergence times are shown in Fig. 5.11. The results confirm that the estimation performance can be directly controlled via manipulation of the observability Gramian eigenvalues.

Chapter 6

ROBOTIC NAVIGATION WITH LIMITED SENSORS: OBSERVABILITY-BASED GUIDANCE ALGORITHMS

In Chapter 5, trajectories were derived that optimize measures of observability for robotic navigation with limited inertial sensors. These trajectories were shown to improve estimator performance through simulation, allowing vehicle position and orientation to be estimated more quickly and with lower uncertainty. Although the observability-optimal trajectories provide superior localization accuracy, they are designed with localization as the only objective and do not incorporate higher-level mission objectives, such as waypoint following or sensor coverage.

In this chapter, observability-based guidance for range-only and bearing-only navigation is extended to include waypoint following through initial and final constraints on the vehicle position in the observability-based guidance problem. An observability-based cost function is developed using the determinant of the inverse of the nonlinear observability matrix, and a guidance framework is presented that enables path planning between waypoints using an explicit tradeoff between path observability and path length. The algorithm development begins with system analysis in Section 6.1, followed by presentation of the guidance algorithm in Section 6.2. The guidance algorithm is evaluated in simulation in Section 6.3 and in experiment on an underwater robotic testbed in Section 6.4.

6.1 System Analysis

In this section, the vehicle and landmark dynamics are developed, and the observability of landmarks is analyzed. A measure of landmark observability is developed

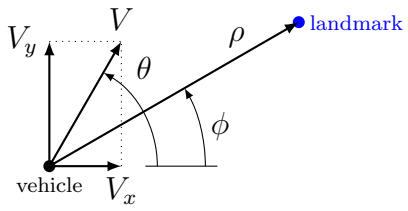

Figure 6.1: Relative position dynamics of a static landmark.

based upon the determinant of the observability matrix, which is used in the following sections to derive observability-based guidance strategies.

6.1.1 System Model

The navigational landmark in the environment is modeled as a static point landmark, with the position of the landmark relative to the vehicle described by the range and bearing to the landmark: $\mathbf{x} = \begin{bmatrix} \rho & \phi \end{bmatrix}^T$. Guidance for the vehicle will be derived by considering the vehicle as a particle, where the vehicle can travel in any direction θ with speed $V \in [0, V_{\max}]$. Although the model utilized for path planning assumes a holonomic vehicle, the observability analysis is valid for a nonholonomic vehicle as long as the vehicle has measurement of inertial heading. Under these assumptions, the dynamics of the landmark relative to the vehicle can be written as

$$\begin{aligned} \frac{\mathrm{d}}{\mathrm{d}t} \begin{bmatrix} \rho \\ \phi \end{bmatrix} &= \begin{bmatrix} -V \cos(\theta - \phi) \\ -V \sin(\theta - \phi) / \rho \end{bmatrix} \\ &= \begin{bmatrix} -\cos\phi & -\sin\phi \\ \frac{1}{\rho}\sin\phi & -\frac{1}{\rho}\cos\phi \end{bmatrix} \begin{bmatrix} V_x \\ V_y \end{bmatrix}. \end{aligned} \tag{6.1}$$

A diagram of the dynamics (6.1) is shown in Fig. 6.1.

Although the observability of range-only and bearing-only navigation was established in Chapter 5, the analysis is repeated here on the range/bearing form of the

dynamics (6.1) to compute the nonlinear observability matrix that will be used in the observability-based cost function.

6.1.2 Observability with Bearing-Only Measurements

Applying the observability test to the landmark dynamics (6.1) with bearing measurement

$$y = \phi \tag{6.2}$$

yields the observability matrix

$$\mathrm{d}\mathbf{Y}_\phi = \begin{bmatrix} 0 & 1 \\ V\sin(\theta-\phi)/\rho^2 & V\cos(\theta-\phi)/\rho \end{bmatrix}, \tag{6.3}$$

with corresponding determinant

$$|\mathrm{d}\mathbf{Y}_\phi| = -V\sin(\theta-\phi)/\rho^2, \tag{6.4}$$

which is nonzero for $V \neq 0$ and $\theta \neq \phi + k\pi$, $k \in \mathbb{Z}$. Therefore, the range and bearing to the landmark is locally observable if the vehicle is moving with nonzero speed and the heading of the vehicle θ is not aligned with the bearing to the landmark ϕ (see Fig. 6.1).

The determinant (6.4) can be maximized (or minimized) for a given state $\mathbf{x}$ by moving the vehicle with heading $\theta^\star = \phi \pm \pi/2$ and speed $V^\star = V_{\max}$. In the presence of a static landmark, implementation of this greedy-optimal policy results in a circular orbit about the landmark, which is equivalent to the optimal trajectory based on the observability Gramian eigenvalues developed in Section 5.4. In the following sections, this measure of observability will be used to derive guidance policies for waypoint following using a single landmark for navigation.

6.1.3 Observability with Range-Only Measurements

Applying the nonlinear observability test to the landmark dynamics (6.1) with range measurement

$$y = \rho \tag{6.5}$$

yields the observability matrix

$$\mathrm{d}\mathbf{Y}_\rho = \begin{bmatrix} 1 & 0 \\ 0 & -V\sin(\theta - \phi) \end{bmatrix}. \tag{6.6}$$

Just as in the bearing case, the observability matrix drops rank when the vehicle heading is aligned with the landmark. The rank drop results from the system dynamics evolving on a lower dimensional manifold when the vehicle heading is aligned with (moving directly towards or away from) the landmark,

$$\begin{aligned} \dot{\rho} &= \pm V \\ \phi &= 0, \end{aligned} \tag{6.7}$$

where the sign of V is determined by the heading of the vehicle. This lower-dimensional system is still locally observable with range-only measurements (but not with bearing-only measurements), therefore the landmark system is always locally observable with range-only measurements.

Interestingly, the determinant of the observability matrix for range-only measurements,

$$|\mathrm{d}\mathbf{Y}_\rho| = -V\sin(\theta - \phi), \tag{6.8}$$

has a very similar form to the bearing-only case (6.4). The greedy-optimal strategy to maximize the determinant again yields $\theta^\star = \phi \pm \pi/2$ and $V^\star = V_{\max}$, which results in a circular trajectory centered at the landmark. Again, this greedy-optimal trajectory matches the optimal trajectory based upon the observability Gramian eigen-

values derived in Section 5.3. Using this similarity, a single framework for deriving observability-based guidance policies is proposed for range-only and bearing-only navigation.

6.2 Observability-Based Guidance for Single Landmark Navigation

The determinant of the observability matrices for bearing measurements (6.4) and range measurements (6.8) are now used as guides to determine a waypoint guidance policy while using a single landmark for navigation. The goal of the guidance policy is to steer the vehicle from an initial point $\mathbf{r}_0$ to a final point $\mathbf{r}_f$ while optimizing landmark observability and maintaining the landmark in the field-of-view of a sensor. Additionally, an algorithm is desired that allows balancing of observability objectives and the trajectory length. Because the determinant is optimized when the vehicle heading is perpendicular to the bearing to the landmark, a lateral facing sensor with field-of-view α is assumed.

6.2.1 Observability Cost Function for Bearing Measurements

The guidance policy is derived by considering the vehicle path in the landmark-centric frame, as shown in Fig. 6.2. The vehicle path is parameterized by the angle $\gamma \in [0, \gamma_f]$, where γ_f is the interior angle between $\mathbf{r}_0$ and $\mathbf{r}_f$. The guidance trajectory is designed by choosing $\rho(\gamma)$ and $\beta(\gamma)$ such that the observability-based cost function is optimized. Let $u = \rho \tan \beta$, then the vehicle path can be described by

$$\frac{\mathrm{d}\rho}{\mathrm{d}\gamma} = u. \tag{6.9}$$

Landmark observability is incorporated into the path planning problem by minimizing the determinant of $\mathrm{d}\mathbf{Y}^{-1}$, which is chosen due to its relation to the volume of the estimation uncertainty ellipsoid (see Chapter 2). For bearing-only measurements,

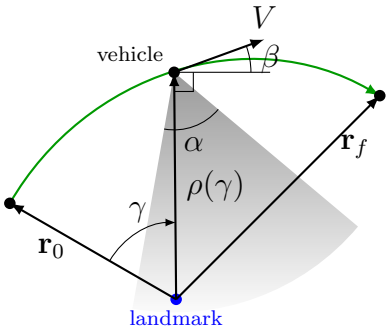

Figure 6.2: Vehicle path planning relative to a static landmark with sensor field-of-view constraints.

the observability-based cost function is formulated in terms of the path angle β,

$$\begin{aligned} |\mathrm{d}\mathbf{Y}_{\phi}^{-1}| &= -\rho^2 \csc(\theta - \phi)/V \\ &= \rho^2 \sec(\theta - \phi + \pi/2)/V \\ &= \rho^2 \sec(\beta)/V. \end{aligned} \tag{6.10}$$

It is immediately apparent that the optimal trajectory requires $V^\star = V_{\max}$, thus the vehicle path can be chosen to minimize the unobservability measure $d_\phi = \rho^2 \sec\beta$. Using trigonometric identities, the unobservability measure is rewritten in terms of the path variables ρ and u,

$$\begin{aligned} u^2 &= \rho^2 \tan^2(\beta) \\ &= \rho^2 \left(\sec^2(\beta) - 1\right) \\ \Rightarrow \sec\beta &= \frac{1}{\rho}\left(u^2 + \rho^2\right)^{\frac{1}{2}} \\ \Rightarrow d_\phi(\rho, u) &= \rho^2 \sec\beta = \rho\left(\rho^2 + u^2\right)^{\frac{1}{2}}. \end{aligned} \tag{6.11}$$

Vehicle guidance is desired that maximizes range and bearing observability while

minimizing path length, where path length in the landmark-centric frame is given by

$$L(\rho, u) = \int_0^{\gamma_f} \left(\rho^2 + u^2\right)^{\frac{1}{2}} \mathrm{d}\gamma. \tag{6.12}$$

This multi-objective problem is formed as a weighted optimization problem with the objective

$$\begin{aligned} J_\phi(\rho, u) &= \int_0^{\gamma_f} \left(L(\rho, u) + w d_\phi(\rho, u)\right) \mathrm{d}\gamma \\ &= \int_0^{\gamma_f} \left(1 + w\rho\right) \left(\rho^2 + u^2\right)^{\frac{1}{2}} \mathrm{d}\gamma, \end{aligned} \tag{6.13}$$

where $w \geq 0$ is the tuning weight. The tuning weight can be interpreted as follows. When $w = 0$, the objective is to minimize the path length without regard to path observability. For $w \to \infty$, the objective is to maximize range and bearing observability without regard to path length. The tuning weight can thus be used to make a tradeoff between observability and path length.

Theorem 9. *The bearing cost function (6.13) is a convex function of ρ and u for path angle $|\beta| < \tan^{-1}(\sqrt{2})$.*

Proof. First note that $L(\rho, u)$ is a convex function and a weighted sum of convex functions is also convex. Therefore, it must be shown that $d_\phi(\rho, u)$ is convex for $|\beta| < \tan^{-1}(\sqrt{2})$. Computing the Hessian of d_ϕ yields

$$\begin{aligned} H_\phi &= \begin{bmatrix} \frac{\partial^2}{\partial \rho^2} & \frac{\partial^2}{\partial \rho \partial u} \\ \frac{\partial^2}{\partial u \partial \rho} & \frac{\partial^2}{\partial u^2} \end{bmatrix} d_\phi(\rho, u) \\ &= \left(\rho^2 + u^2\right)^{-\frac{3}{2}} \begin{bmatrix} 2\rho^3 + 3\rho u^2 & u^3 \\ u^3 & \rho^3 \end{bmatrix}. \end{aligned} \tag{6.14}$$

Because $\rho > 0$, the first minor of H_ϕ is positive. The second minor is the determinant, given by

$$|H_\phi| = \frac{3\rho^2}{\rho^2 + u^2} - 1, \tag{6.15}$$

which is positive for

$$\frac{u^2}{\rho^2} < 2 \;\Leftrightarrow\; \tan^2(\beta) < 2 \;\Leftrightarrow\; |\beta| < \tan^{-1}(\sqrt{2}). \tag{6.16}$$

Therefore, if $|\beta| < \tan^{-1}(\sqrt{2})$, then H_ϕ is positive definite, and d_ϕ is a convex function on the domain $|u| < \sqrt{2}\rho$. □

The restriction on the path angle is equivalent to a field-of-view constraint on the sensor. For $|\beta| < \tan^{-1}(\sqrt{2})$, the equivalent sensor field-of-view is $\alpha \approx 109$ deg. Thus, if the sensor field-of-view is less than 109 deg, then the domain constraint is already satisfied. If the sensor field-of-view is greater than 109 deg, then the domain constraint limits the amount that the observability-based path can deviate from the minimum length path. As it will be shown in the simulation results, however, the larger path deviations have diminishing returns on the observability measure and the domain constraint does not limit performance in practice. In exchange for a restricted solution domain, we gain guaranteed convergence and optimality for the convex cost function.

6.2.2 Observability Cost Function for Range Measurements

Observability using range measurements is incorporated into the path planning framework using the same methods employed for bearing measurements. The unobservability measure for range measurements is given by

$$d_\rho(\rho, u) = \sec\beta = \frac{1}{\rho}\left(\rho^2 + u^2\right)^{\frac{1}{2}}. \tag{6.17}$$

Theorem 10. *The range unobservability measure $d_\rho(\rho, u)$ is a quasi-convex function of ρ and u for $\rho > 0$.*

Proof. Quasi-convexity is proven by examining the second-order conditions for quasi-convexity. The gradient of the expression is given by

$$\begin{bmatrix} \frac{\partial}{\partial \rho} \\ \frac{\partial}{\partial u} \end{bmatrix} f(\rho, u) = \left(\rho^2 + u^2\right)^{-\frac{1}{2}} \begin{bmatrix} -\frac{u^2}{\rho} \\ u \end{bmatrix}, \tag{6.18}$$

which is zero for $u = 0$ on the domain $\rho > 0$. Therefore, by the second-order conditions for quasi-convexity [29], the Hessian must be positive semidefinite for $u = 0$, and must have at least one positive eigenvalue when $u \neq 0$. The first-order minor of the Hessian is given by

$$\frac{\partial^2}{\partial \rho^2} f(\rho, u) = \frac{u^2 \left(3\rho^2 + 2u^2\right)}{\rho^3 \left(\rho^2 + u^2\right)^{\frac{3}{2}}} \geq 0, \tag{6.19}$$

and the determinant of the Hessian is

$$|H_\rho| = -\frac{u^2}{\rho^4(\rho^2 + u^2)} \leq 0. \tag{6.20}$$

Thus, the Hessian has one positive and one negative eigenvalue when $u \neq 0$. When $u = 0$, the Hessian is

$$H_\rho\big|_{u=0} = \begin{bmatrix} 0 & 0 \\ 0 & 1/\rho^2 \end{bmatrix}, \tag{6.21}$$

which is positive semi-definite for $\rho > 0$. Therefore, the range unobservability measure, $d_\rho(\rho, u)$ is quasi-convex in ρ and u for $\rho > 0$. □

Although the quasi-convex guidance problem can be solved via sequential convex optimization and a line search, we propose a convex relaxation to the range unobservability measure that allows an approximate solution to be more readily obtained.

Consider the relaxation of $d_\rho(\rho, u)$ given by

$$\tilde{d}_\rho(u) = d_\rho(\bar{\rho}, u) = \left(1 + \frac{u^2}{\bar{\rho}^2}\right)^{\frac{1}{2}}, \tag{6.22}$$

where $\bar{\rho}$ is the average of the initial and final conditions on the range, $\bar{\rho} = \frac{1}{2}(\rho_0 + \rho_f)$. If the variation in the range over the length of the trajectory is small, these two objectives will result in similar optimal trajectories. In some scenarios, these two objectives will produce equivalent trajectories.

Theorem 11. *The solution to the observability-based guidance problem*

$$\begin{aligned} \min_{\rho(\gamma), u(\gamma)} \quad & \int_0^{\gamma_f} d_\rho(\rho, u) \mathrm{d}\gamma \\ \text{subject to} \quad & \frac{\mathrm{d}\rho}{\mathrm{d}\gamma} = u \\ & \rho(0) = \rho(\gamma_f) = \rho_0 \end{aligned} \tag{6.23}$$

is equivalent to the solution of the problem when the objective, $d_\rho(\rho, u)$, is replaced by the relaxed objective, $\tilde{d}_\rho(u)$.

Proof. The proof is done by showing that the optimal trajectory, $\rho^\star(\gamma) = \rho_0$ and $u^\star(\gamma) = 0$ satisfy the first-order necessary conditions for a minimum of both problems (see [103]). The Hamiltonians for each problem are given by

$$\begin{aligned} H(\rho, u) &= d_\rho(\rho, u) + \lambda u \\ \tilde{H}(u) &= \tilde{d}_\rho(u) + \tilde{\lambda} u. \end{aligned} \tag{6.24}$$

The stationarity conditions for the two problems are

$$\begin{aligned} \frac{\partial}{\partial u} H(\rho, u) &= \frac{u}{\rho^2} \left(1 + \frac{u^2}{\rho^2}\right)^{-\frac{1}{2}} + \lambda = 0 \\ \frac{\partial}{\partial u} \tilde{H}(u) &= \frac{u}{\bar{\rho}^2} \left(1 + \frac{u^2}{\bar{\rho}^2}\right)^{-\frac{1}{2}} + \tilde{\lambda} = 0, \end{aligned} \tag{6.25}$$

which are both satisfied by the optimal trajectory $(\rho^\star, u^\star)$ and $\lambda^\star = \tilde{\lambda}^\star = 0$. The costate dynamics are given by

$$\begin{aligned} \frac{\mathrm{d}\lambda}{\mathrm{d}\gamma} &= -\frac{\partial}{\partial \rho} H(\rho, u) = \frac{u^2}{\rho^3} \left(1 + \frac{u^2}{\rho^2}\right)^{-\frac{1}{2}} \\ \frac{\mathrm{d}\tilde{\lambda}}{\mathrm{d}\gamma} &= -\frac{\partial}{\partial \rho} \tilde{H}(u) = 0, \end{aligned} \tag{6.26}$$

which are satisfied by the optimal trajectory $(\rho^\star, u^\star)$ and $\lambda^\star = \tilde{\lambda}^\star = 0$. Therefore, the two solutions are equivalent in the case when the initial and final ranges are equal. □

The condition $\rho_0 = \rho_f$ implies that the landmark is on the separating hyperplane between the two waypoints. The two objectives will not produce equivalent solutions for every landmark position, but numerical studies have shown that the relaxed objective produces very similar trajectories over a large range of landmark positions. The unobservability measure, $d_\rho(\rho, u)$, was evaluated for optimal trajectories generated by both the relaxed and quasi-convex optimization problems for varying landmark position. Landmark position was varied using the parameters δ and ζ, as shown in Fig. 6.3. The percentage increase in observability measure due to the relaxed objective is shown in Fig. 6.4, with the thick line indicating the 5% contour. The majority of landmark positions result in minimal change in the unobservability measure, with the exception of areas very near the waypoints.

These results motivate the use of the relaxed objective to reduce computational requirements. Combining the unobservability measure with the path length measure

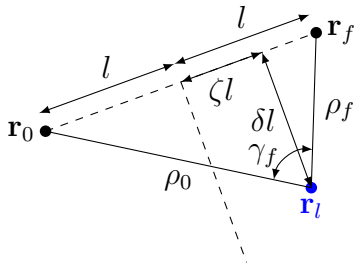

Figure 6.3: Geometry of landmark positions relative to waypoints.

using a tuning weight yields the observability-based cost function for range measurements

$$\begin{aligned} J_\rho(\rho, u) &= \int_0^{\gamma_f} \Big(L(\rho, u) + w\tilde{d}_\rho(u) \Big) \, \mathrm{d}\gamma \\ &= \int_0^{\gamma_f} \left[\left(\rho^2 + u^2\right)^{\frac{1}{2}} + w \left(1 + \frac{u^2}{\bar{\rho}^2} \right)^{\frac{1}{2}} \right] \mathrm{d}\gamma. \end{aligned} \tag{6.27}$$

The tuning weight w has the same interpretation as in the bearing measurement case, where $w = 0$ yields the shortest path problem and $w \to \infty$ yields the observability-optimal path problem.

6.2.3 Assembled Observability-Based Optimization Problem

Sensor field-of-view constraints are incorporated into the optimization problem by considering the geometry of the problem shown in Fig. 6.2. To maintain the landmark in the sensor field-of-view, the path angle β must satisfy

$$\begin{aligned} & |\beta| \leq \alpha/2 \\ \Leftrightarrow \; & |\tan\beta| \leq \tan(\alpha/2) \\ \Leftrightarrow \; & |u| \leq \rho \tan(\alpha/2), \end{aligned} \tag{6.28}$$

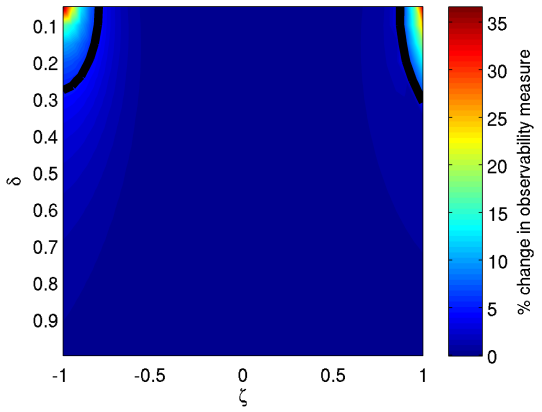

Figure 6.4: Change in unobservability measure due to the use of a relaxed convex objective for varying landmark position. The relaxed objective generates trajectories with equivalent unobservability measures along the separating hyperplane ($\zeta = 0$), and minimal increase in the unobservability measure for landmark positions not near the waypoints. The thick line shows the 5% contour, indicating that the relaxed objective is valid for the majority of landmark positions.

where the monotonicity of tan and the positivity of ρ are used to transform the angle constraint into linear inequality constraints in ρ and u.

Assembling the cost functions (6.27) and (6.13) with the path dynamics (6.9) and field-of-view constraint (6.28) yields an observability-based optimization problem for single landmark navigation,

$$\begin{aligned} \min_{\rho(\gamma),u(\gamma)} \quad & J(\rho,u) \\ \text{subject to} \quad & \frac{\mathrm{d}\rho}{\mathrm{d}\gamma} = u \\ & \rho(0) = \rho_0 \\ & \rho(\gamma_f) = \rho_f \\ & |u| \leq \rho \tan\left(\alpha/2\right), \end{aligned} \tag{6.29}$$

where the objective $J(\rho,u)$ is replaced by $J_\rho(\rho,u)$ for the range-only guidance problem

and $J_\phi(\rho, u)$ for the bearing-only guidance problem. The optimization problem (6.29) is a convex problem in the variables ρ and u and can be solved given problem data ρ_0, ρ_f, α, and w using angular discretization of γ and efficient interior-point methods [29].

6.3 Simulation Results

Simulation studies were performed to evaluate the effectiveness of the observability-based guidance. Performance was evaluated in simulation in MATLAB using the interior point method of the optimization toolbox to solve the path planning problem (6.29).

6.3.1 Trajectory Tracking Controller Design

A controller was designed to allow the vehicle to track the observability-based guidance trajectories. A model predictive control (MPC) scheme is used to compute the control input. The advantage of the MPC method is that it converts the solution of an optimization problem into a feedback control law. The optimization problem (6.29) is discretized into N equal angular segments of size $\Delta\gamma$. At each step of the control law, the estimated vehicle position is updated using the latest range or bearing measurement. Then, the trajectory is re-planned by solving the discretized optimization problem (6.29). Finally, the first control action in the trajectory is taken and the vehicle moves towards the goal for one time step. This procedure is repeated until the vehicle reaches the goal position as detailed in Algorithm 2.

The estimated range and bearing are obtained using an extended Kalman filter (EKF) according to the continuous-discrete formulation presented in [27]. The continuous time dynamics model is given by (6.1) and time-discretized measurements of the range ρ or bearing ϕ are used to update the filter. The dynamics linearization performed at each step of the EKF is found by linearization of the nonlinear dynamics

Algorithm 2 Observability-Based MPC Guidance Law

Require: Landmark position, $\mathbf{r}_l$
Require: Estimated initial position, $\hat{\mathbf{r}}_0$
Require: Desired final position, $\mathbf{r}_f$
Require: Sensor field of view angle, α
Require: Number of trajectory time discretizations, N
Require: Observability tuning weight, w
  $\hat{\rho} \leftarrow \|\mathbf{r}_l - \hat{\mathbf{r}}_0\|$
  $\hat{\phi} \leftarrow \angle(\mathbf{r}_l - \hat{\mathbf{r}}_0)$
  $\rho_f \leftarrow \|\mathbf{r}_l - \mathbf{r}_f\|$
  $\phi_f \leftarrow \angle(\mathbf{r}_l - \mathbf{r}_f)$
  while $N > 0$ **do**
    Propagate and update $\hat{\rho}$ and $\hat{\phi}$
    $\gamma_f \leftarrow \hat{\phi} - \phi_f$
    Solve problem (6.29) using $\hat{\rho}$ as an initial range
    $\theta \leftarrow \tan^{-1}(u(0)/\rho(0)) + \hat{\phi} + \pi/2$
    $\mathbf{V} \leftarrow V_{\max} \begin{bmatrix} \cos\theta \\ \sin\theta \end{bmatrix}$
    Apply control $\mathbf{V}$ for $\Delta t = (\rho(0)^2 + u(0)^2)^{\frac{1}{2}} \frac{\Delta\gamma}{V_{\max}}$
    $N \leftarrow N - 1$
  end while

model (6.1),

$$F(\hat{\mathbf{x}}) = \begin{bmatrix} 0 & -V\sin(\theta - \hat{\phi}) \\ \frac{V}{\hat{\rho}^2}\sin(\theta - \hat{\phi}) & \frac{V}{\hat{\rho}}\cos(\theta - \hat{\phi}) \end{bmatrix}. \tag{6.30}$$

6.3.2 Pareto Optimality

The Pareto optimality curve was explored for the range-only and bearing-only guidance policies. Each policy was simulated in closed-loop with an EKF providing range and bearing estimates to the MPC Algorithm 2. The simulation used $N = 20$ time steps, and the dynamics (6.1) were integrated at each time step using the `ode45` solver. The Pareto optimality curve was obtained by simulating the closed-loop system for varying values of the weight w, which controls the tradeoff between path length and the unobservability measure. Because it was hypothesized that decreasing the un-

observability measure directly decreases estimation error, the tradeoff between path length and estimation error was measured to obtain the Pareto curve. Estimation error was measured by the root mean square (RMS) error between the true trajectories and estimated trajectories. The estimation error for each simulation is normalized by the estimation error for the shortest path trajectory for the given waypoints and landmark.

The Pareto curve was obtained for a scenario where the landmark was positioned along the separating hyperplane between the two waypoints. This scenario provides the most freedom in path planning because the sensor field-of-view constraint is the least limiting. The landmark position was chosen such that a straight trajectory from initial position to final position would maintain the landmark in the field of view. In this scenario, the vehicle started at $\mathbf{r}_0 = \begin{bmatrix} 0 & 0 \end{bmatrix}^T$ with a desired waypoint at $\mathbf{r}_f = \begin{bmatrix} 10 & 0 \end{bmatrix}^T$ and the landmark located at $\mathbf{r}_l = \begin{bmatrix} 5 & -5 \end{bmatrix}^T$. The sensor field-of-view angle was set to $\alpha = 109$ deg.

The Pareto curve for range-only measurements is shown on the left side of Fig. 6.5. The closed-loop system was simulated for 17 different weights ranging from 0 to 2 to generate the results. The tradeoff curve shows that relatively small deviations in path length can yield large improvements in estimator performance (*e.g.*, 10% increase in path length decreases the estimation error by more than 30%).

The Pareto curve for bearing-only measurements is shown on the right side of Fig. 6.5. The closed-loop system was simulated for 21 different weights ranging from 0 to 10 to generate the results. The tradeoff curve shows again that very small deviations in path length improve estimator performance substantially (*e.g.*, 5% increase in path length decreases the estimation error by more than 30%). The planned trajectories that generated the tradeoff curves are shown in Fig. 6.6. The observability-based trajectories for range and bearing measurements exhibit a symmetry, where the range trajectories form as arcs with minimum path angle β, while the bearing trajectories curve towards the landmark to minimize range. In both cases, the choice of $w = 0$

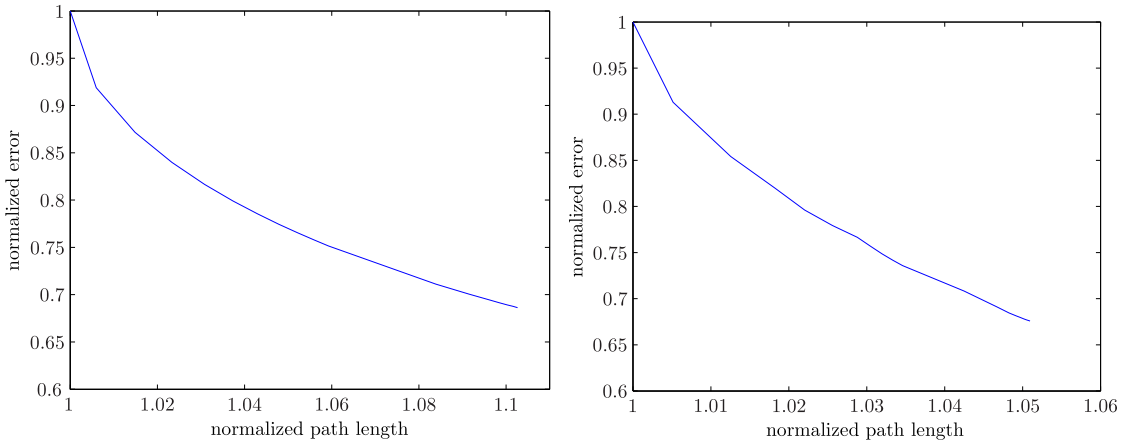

Figure 6.5: Pareto optimality curve for observability-based guidance with range-only measurements (left) and bearing-only measurements (right). The error and path length are normalized by the error and path length of the shortest trajectory.

yields the minimum length path to the desired location, and larger values of w increase the deviation from the minimum length path to improve observability.

6.3.3 Effect of landmark location on estimator performance

The estimation performance was measured for different landmark positions relative to the waypoints to identify how the impact of observability-based guidance varies with relative landmark positions. Landmark position was varied between the start and end waypoints using the parameters δ and ζ as shown in Fig. 6.3.

For each tested landmark position, closed-loop simulations were evaluated using the shortest planned path ($w = 0$) and the observability-optimal path ($w = 10,000$). The normalized estimation error was computed to measure the estimator improvement afforded by the observability-based guidance. Normalized error for variations in landmark position with range-only measurements is shown in Fig. 6.7 and with bearing-only measurements is shown in Fig. 6.8.

Estimator performance for range-only navigation shows that the largest decrease

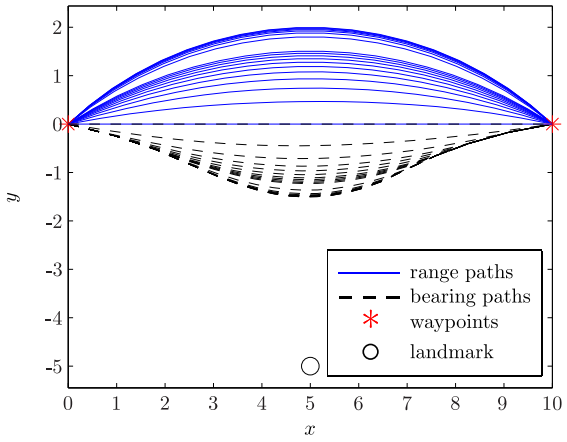

Figure 6.6: Observability-based guidance trajectories for bearing-only and range-only measurements that were used to generate the Pareto optimality curves. The observability-based trajectories for range-only measurements form into an arc, while the trajectories for bearing-only measurements curve towards the landmark.

in error compared to following the shortest path occurs when the landmark is located near the starting waypoint ($\zeta < 0$ and $\delta < 0.5$). In this region, the estimation error can be reduced by more than half by using the observability-based guidance scheme proposed here. This performance increase is attributed to the fact that following the shortest path results in large path angles β and, therefore, large values of the unobservability index d_ρ. The observability-based guidance produces the minimum unobservability index and, thus, gives a significant improvement in estimator performance. The opposite effect is observed when the landmark is near the final waypoint ($\zeta > 0$ and $\delta < 0.2$). In this region, the shortest path and the observability-optimal path are very similar when they approach the final waypoint and, thus, have similar unobservability indices and estimator performance. When the landmark is distant ($\delta \to \infty$) the difference between the shortest path and the observability-optimal arc path is minimal, resulting in little difference in estimator performance. From the results of Fig. 6.7, it is shown that for $\delta > 2$, which is equivalent to a landmark position

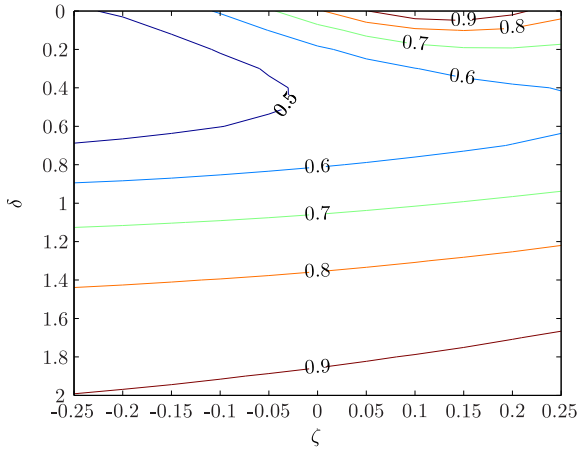

Figure 6.7: Normalized estimation error variation for range-only measurements as a function of the landmark position. As the landmark moves closer to the waypoints, the observability-based guidance yields a larger improvement in estimator performance. When the landmark is distant ($\delta \to \infty$), the observability-optimal trajectory does not differ much from the shortest-path trajectory and, therefore, does not produce significantly better estimator performance.

further away than the distance between the waypoints, the performance improvement afforded by the observability-based guidance is less than 10%. When the landmark is distant, therefore, using the proposed scheme over shortest-path waypoint following may not be warranted because the two methods generate very similar trajectories.

Results for bearing-only navigation in Fig. 6.8 exhibit a similar pattern to the range-only estimator performance results. When the landmark is near the line between the waypoints ($\delta = 0$), the observability-based guidance produces the largest reduction in estimation error compared to the baseline shortest path guidance (greater than 70% decrease in error). This is due to the fact that the observability-based guidance produces a trajectory that passes very near the landmark, resulting in a small unobservability index d_ϕ and optimal estimation performance. As the landmark moves further away ($\delta \to \infty$), the observability improvement afforded by the proposed guidance scheme is minimal and results in small improvements in estimator performance.

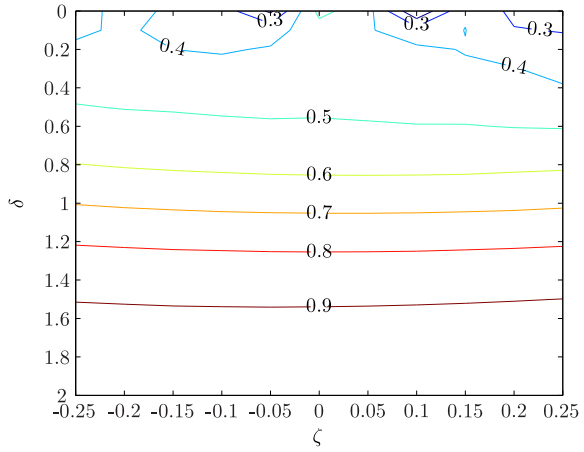

Figure 6.8: Normalized estimation error variation for bearing-only measurements as a function of the landmark position. The largest improvement in estimator performance is observed near $\delta = 0$, where the observability-based guidance yields a significant change in the planned path. When the landmark is distant ($\delta \to \infty$), the observability-optimal trajectory does not differ much from the shortest-path trajectory and, therefore, does not produce significantly better estimator performance.

The results of this study reveal regions where the observability-based guidance is most useful. For range-only navigation, this region is approximately $\delta \leq 2$, and for bearing-only navigation, this region is approximately $\delta \leq 1.5$. In these regions, the proposed guidance yields at least 10% decrease in estimation error.

6.4 Experimental Results

Experiments were performed in a controlled underwater environment to validate the observability-based guidance for range-only and bearing-only navigation. This section details the robotic testbed used in the experiments and includes a discussion of the experimental results.

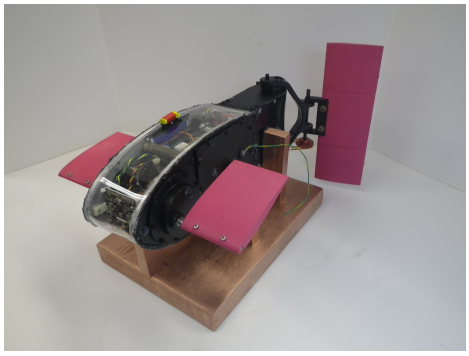

Figure 6.9: The robotic fish testbed uses a dual-link tail for propulsion and steering, and pectoral fins for depth control.

6.4.1 Robotic Fish Testbed

The robotic fish testbed used in these experiments is an autonomous fin-actuated underwater vehicle, pictured in Fig. 6.9. This vehicle utilizes a dual-link tail for propulsion and steering, and a pair of independently-controlled pectoral fins for depth control. The robotic fish is equipped with a pressure sensor for depth measurement, an inertial measurement unit for inertial orientation and angular rate measurement, and a CMUcam4 in the nose of the fish for vision processing. A calibrated underwater camera system is used to track vehicle position in an $8 \times 20 \times 8$ ft water tank ($w \times l \times d$). The vehicle's position and velocity is communicated to the vehicle at a rate of approximately 5 Hz over a low-frequency radio.

For the purpose of the range-only navigation experiments, the position transmitted to the vehicle was translated to a range from a simulated ranging beacon at a predefined location. In an open water experiment, the camera system would be replaced by an acoustic ranging beacon, but due to the size and acoustic reflectivity of the test tank, acoustic localization was unavailable. Bearing measurements are made using the color tracking capability of the CMUcam4 and a brightly-colored landmark placed in the test tank. An angled mirror at the front of the vehicle allows the cam-

era to obtain a lateral field-of-view, and a pinhole camera model transforms measured color centroids to a bearing to the landmark.

The robotic fish houses a single board computer with 1.3 GHz processor running Ubuntu Linux. Communication, guidance, control, and estimation applications are written in `C++` with the aid of the Robot Operating System (ROS) for inter-process communication. The observability-based guidance is computed on-board using the `C` API for the nonlinear programming feature of the `mosek` optimizer [104]. A typical optimization solution with $N = 12$ waypoints is obtained in 40 ms on the single board computer. Although the solution time is more than fast enough to run in real time, the guidance trajectories were computed once at the beginning of each experiment, rather than iteratively as in the MPC Algorithm 2. A proportional heading controller was used to follow the waypoints generated from the guidance solution. The EKF used for estimating range and bearing to the landmark utilized the armadillo linear algebra library. Estimates from the EKF were propagated and updated at a rate of 5 Hz using a fourth-order Runge-Kutta integration.

6.4.2 Bearing-Only Navigation Results

Bearing-only navigation experiments were conducted to explore the effect that sensor field-of-view has on the observability-based path planning. The camera on board the robotic fish is the CMUcam4, which has a 50 degree field-of-view. Because the field-of-view is fairly narrow, the freedom in path planning is limited and the difference between shortest path guidance and observability-optimal guidance is minimal. The path planning problem (6.29) constrains the path to allow the landmark to remain in the sensor field-of-view at all times. This constraint was relaxed to allow the vehicle to deviate further from the shortest path to obtain a better observing position relative to the landmark, while sacrificing some measurements *en route*. The field-of-view constraint was varied from the minimum, 50 deg, to the maximum, 109 deg, seeking to answer the question: when it comes to landmark measurements, is quality better

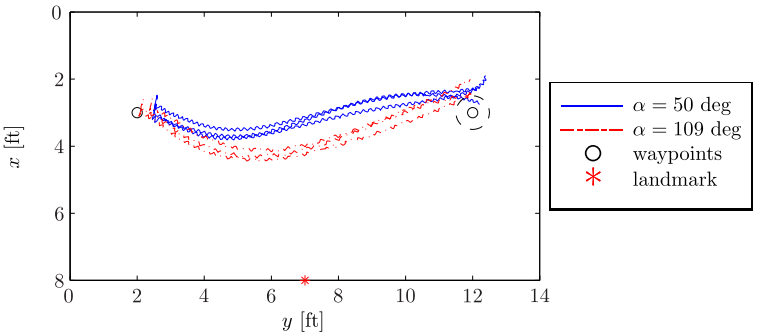

Figure 6.10: Trajectories followed by the robotic fish testbed during bearing-only navigation experiments. The trajectories were generated using two different field-of-view values α, with three trials for each field-of-view. Deviations between trajectories generated from the same field-of-view were due to estimation errors and are representative of the vehicle's ability to track a trajectory. The oscillations in the trajectories are due to the fish's oscillatory swimming motion, coupled with the forward location of the camera where lateral motion is the maximum.

than quantity?

Two sets of bearing-only navigation experiments were performed using two field-of-view values in the optimization problem: the true sensor field-of-view, 50 deg, and the maximum sensor field-of-view, 109 deg. The observability-optimal trajectory was computed and followed by the vehicle for each field-of-view using $N = 12$ waypoints and an observability weight of $w = 100$. Each trial was executed three times for a total of six experiments.

The trajectories for the two field-of-view values are shown in Fig. 6.10. The first set of shorter trajectories correspond to the true sensor field-of-view. During the first set of experiments, the vehicle maintained the landmark in view for 77% of the time on average. Although the trajectory is planned to keep the landmark in view at all times, the oscillation of the fish motion ($\sim$3 deg amplitude), combined with estimation and tracking error cause the landmark to move out of view at times. The second set of experiments (the longer trajectories) correspond to the maximum field-of-view of

109 deg. The relaxed field-of-view constraint allowed the vehicle to move closer to the landmark for better observation. During these experiments, the landmark was in view 47% of the time on average. Despite fewer measurements being available, the relaxed field-of-view constraint produced 8% lower RMS range and bearing estimation error on average when compared to the baseline field-of-view of 50 deg.

6.4.3 Range-Only Navigation Results

Range-only navigation experiments were conducted to demonstrate the tradeoff between path observability and path length, similar to the Pareto-optimality simulation studies detailed in Section 6.3. Initial and final waypoints were designed such that the landmark was located on the mean plane between the waypoints ($\zeta = 0$), and the landmark was nearby ($\delta = 0.4$). Observability-based guidance was used to compute trajectories for six different weights w, ranging from 0 (shortest path) to 10 (observability-optimal), for $N = 12$ waypoints. Because the range sensing does not have a field-of-view, field-of-view constraints in the optimization problem were omitted (*i.e.*, $\alpha = 180$ deg). Each trial began with the vehicle placed at the starting waypoint. The vehicle was commanded to perform the observability-based guidance, at which point the optimal trajectory was computed and the vehicle began following the trajectory using a proportional heading controller. The trial ended when the vehicle reached a circular manifold around the final waypoint (radius 0.5 ft in these trials). Each trial was performed three times.

The 18 trajectories generated by the vehicle are shown in Fig. 6.11, where the six groups of trajectories delineate the six observability weights used in the trajectory optimization. Qualitatively, the trajectories with higher observability weight (the longer, more arc-like trajectories) are more repeatable and coalesce near the final waypoint, indicating superior estimation performance and, thus, better trajectory tracking. These observations are supported by the estimation error computed for each trial. The RMS error between the EKF estimates of range and bearing and the

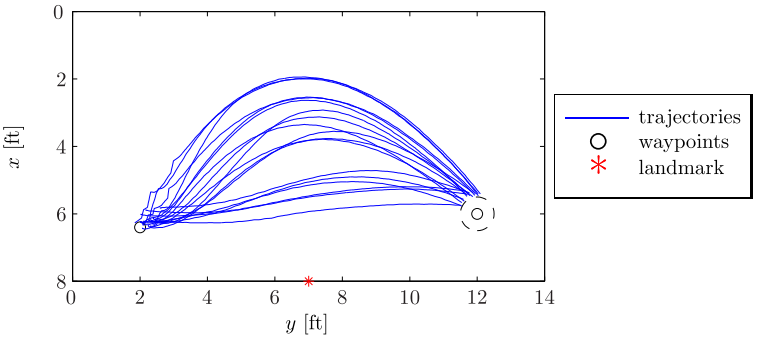

Figure 6.11: Trajectories followed by the robotic fish testbed during range-only navigation experiments. The trajectories were generated using six different observability weights w, with three trials for each weight. Deviations between trajectories generated from the same weight were due to estimation errors and are representative of the vehicle's ability to track a trajectory.

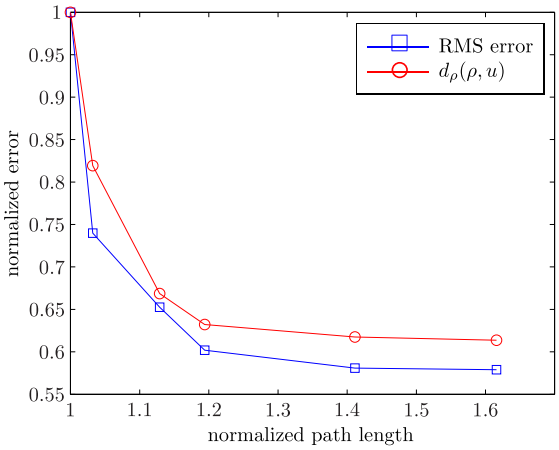

Figure 6.12: Normalized RMS error and unobservability measures for range-only navigation experiments as a function of path length. As the observability weight is increased (increased path length), the RMS error is decreased. The RMS error shows a strong correlation to the unobservability measure.

range and bearing measured by the camera tracking system was computed for each trial. The three trials for each observability weight were averaged and normalized by

the averaged RMS error for the shortest trajectories. The unobservability measure for each trajectory was computed and averaged for the three trials. A comparison of the RMS error and unobservability measures, normalized by the shortest path error and unobservability measure, is shown in Fig. 6.12. The RMS error for the observability-optimal path ($w = 10$) is 58% of the RMS error for the straight path, which corresponds well to the simulation studies for a landmark placed at $\zeta = 0$ and $\delta = 0.4$ (see Fig. 6.7). The RMS error shows a strong correlation to the unobservability measure, validating the observability-based guidance as a method for controlling estimation error.

Chapter 7

CONCLUSION

This dissertation developed an observability-based approach to the analysis and design of motion planning and sensor placement for nonlinear systems. Several measures of observability were employed as metrics for trajectory or sensor fitness, of which the observability Gramian proved to be particularly useful. Although the observability Gramian is a measure of observability for linear systems, simulations and experiments demonstrated that the Gramian can provide valid and meaningful measures of observability for nonlinear systems about a nominal trajectory.

One of the main contributions of this thesis is a sensor placement algorithm that incorporates nonlinear dynamics, nonlinear measurement models, and heterogeneous sensor types. By leveraging methods from mixed integer programming and convex optimization, solution methods were proposed that allow the algorithms to scale more favorably to larger problems. In particular, the ℓ_1-regularization technique allowed the sensor placement problem to be posed as a semidefinite program, which scales well with system size (number of states) and number of sensors. Because the observability Gramian can be approximated numerically using the empirical observability Gramian, the sensor placement algorithm can be applied using only a simulation of a nonlinear system as input data, with no analytical model required.

The sensor placement procedure was extended to a sensor data compression algorithm, which finds a temporal filter that compresses sensor data such that the amount of information in the filtered signal is maximized. The data compression problem was posed as a convex optimization problem with an ℓ_1-bound on the compression filter, which promotes a sparse filter solution. By applying the sensor placement and

compression algorithms, the spatial and temporal distribution of information in a process can be identified, and the most informative measurements can be selected. The sensor compression algorithm has interesting implications for distributed sensing applications, where data compression can be used to minimize communication between sensor nodes and minimize computation when sensor data are fused between multiple nodes. Additionally, the data compression has an analogous role in neural filtering in biological systems, where filtering on individual sensors reduces the amount of data passed to a central processing unit.

The utility of the sensor placement and compression algorithms is their broad applicability. Because these algorithms were designed for a nonlinear system defined by a general, control-affine ordinary differential equation, they can be applied in a wide variety of areas. One interesting application is in the study of biological systems, where distributed sensing is prevalent. A detailed example application was provided in a study of the gyroscopic sensing capabilities in insect wings. The sensor placement strategy revealed how the heterogeneity of campaniform sensilla might be distributed along the wing of the hawkmoth to optimally detect inertial rotation rates. Comparison to biological data indicated that the algorithm predicted areas where sensors are clustered on the wing, indicating that these clusters of sensors may serve as good encoders of gyroscopic information.

The second main contribution of this thesis is an observability-based guidance framework for vehicles navigating with limited inertial information. The observability-based guidance problem was solved analytically for vehicles navigating with range-only or bearing-only measurements to a static landmark, showing that a circular trajectory centered at the landmark minimized the observability Gramian condition number. The guidance problem was also solved analytically for navigation in currents and extended to higher-dimensional nonholonomic systems. These observability-based trajectories provided superior estimation performance in simulation when compared to suboptimal trajectories, indicating that the observability Gramian measure

captures the nonlinear dynamics. An example application of this guidance framework is motion planning for single range-aided navigation of an underwater vehicle. In this scenario, the vehicle can perform the optimal circle maneuver to obtain an accurate localization, after which, the vehicle can perform its mission with reduced localization uncertainty (*e.g.*, follow a sensor coverage trajectory).

The observability-based guidance framework was extended to an algorithmic guidance strategy for range-only and bearing-only navigation. These algorithms allow vehicle path planning and observability to be considered *simultaneously*, therefore, trajectories can be computed that explicitly tradeoff observability measures with mission parameters (*e.g.*, path length). The guidance algorithms were tested in simulation to explore the effect of landmark location on estimation performance. Experiments with a robotic fish testbed validated the usefulness of the algorithms, demonstrating that the observability tuning weight can be used to directly control localization uncertainty. Because the guidance is computed using convex optimization, the algorithm is amenable to implementation on robotic platforms with limited processing power. In the robotic experiments presented here, the typical guidance trajectory was computed in approximately 40 ms, which is fast enough for implementation on many robotic platforms.

The research presented in this thesis provides several interesting avenues for future work. One intriguing research area is in the application of the sensor compression algorithm to natural and engineered systems. Because biological systems often use massively distributed sensing, the neural filtering component of the sensing provides a sort of distributed computation that reduces the amount of computation required by a central unit. By pairing the tools developed here with a neurological study, the benefits of neural compression may be better characterized from a systems-theoretic perspective. In the context of sensor networks, the sensor compression algorithm may allow for the design of distributed estimation with limited communication, where only the most important bits of information are exchanged between sensor nodes.

The observability-based guidance algorithms for range-only and bearing-only navigation were developed for waypoint following, but can be extended to plan higher-level trajectories such as search patterns. Given a radius of region to search, the vehicle path can be planned in the landmark-centric frame with multiple revolutions about the landmark ($\gamma_f > 2\pi$). Constraints on the search pattern parameters (*e.g.*, pitch between consecutive passes) can easily be integrated into the optimization problem. For range-only navigation, a spiral-like trajectory centered at the landmark will likely produce good observability characteristics while covering a circular search region. These guidance algorithms will provide an integrated trajectory planner that simultaneously accounts for high-level mission tasks and localization accuracy.

Another potential extension of the observability-based guidance is path planning with multiple landmarks present. One simple solution to this scenario is to select a single key landmark for navigation that provides the best observability characteristics and use the existing framework to plan a trajectory relative to the single landmark. The results of the landmark position study (see Figs. 6.7 and 6.8) can be used to select a key landmark that provides good performance. When landmarks are sparsely distributed, selecting a single landmark for navigation will likely be advantageous. However, when landmarks are densely distributed, selecting a single landmark may not provide optimal observability.

Finally, because the guidance algorithms can be used to replan the trajectory as the mission progresses, the framework lends itself well to dynamically selecting optimization parameters. For example, the observability tuning weight w could be dynamically selecting based upon feedback of estimator performance, such as the covariance matrix. When the covariance is high, a large weight should be chosen to maneuver to improve observability and thus reduce the estimation uncertainty. When the covariance is low, a smaller weight should be chosen to minimize path length.

BIBLIOGRAPHY

[1] B. J. Guerreiro, P. Batista, C. Silvestre, and P. Oliveira, "Sensor-based simultaneous localization and mapping – part I: GAS robocentric filter," in *American Control Conference*, 2012.

[2] ——, "Sensor-based simultaneous localization and mapping – part II: Online inertial map and trajectory estimation," in *American Control Conference*, 2012.

[3] M. Bryson and S. Sukkarieh, "An information-theoretic approach to autonomous navigation and guidance of an uninhabited aerial vehicle in unknown environments," in *Intelligent Robots and Systems*, 2005.

[4] ——, "Observability analysis and active control for airborne SLAM," *IEEE Transactions on Aerospace and Electronic Systems*, vol. 44, no. 1, pp. 261–280, Jan 2008.

[5] A. Gadre, "Observability analysis in navigation systems with an underwater vehicle application," Ph.D. dissertation, Virginia Polytechnic Institute and State University, 2007.

[6] P. Batista, C. Silvestre, and P. Oliveira, "Single range aided navigation and source localization: Observability and filter design," *Systems & Control Letters*, vol. 60, no. 8, pp. 665–673, Aug. 2011.

[7] W. P. Chan, F. Prete, and M. H. Dickinson, "Visual input to the efferent control system of a fly's "gyroscope"," *Science*, vol. 280, pp. 289–292, 1998.

[8] D. Kleinfeld, E. Ahissar, and M. E. Diamond, "Active sensation: insights from the rodent vibrissa sensorimotor system," *Current Opinion in Neurobiology*, vol. 16, no. 4, pp. 435–444, August 2006.

[9] R. B. Towal and M. J. Z. Hartmann, "Principles and applications of active tactile sensing strategies in the rat vibrissal system," in *IEEE SENSORS Conference*, 2010.

[10] K. Kral, "Behaviouralanalytical studies of the role of head movements in depth perception in insects, birds and mammals," *Behavioural Processes*, vol. 64, pp. 1–12, 2003.

[11] R. Necker, "Head-bobbing of walking birds," *Journal of Comparative Physiology A*, vol. 193, pp. 1177–1183, 2007.

[12] B. J. Frost, "The optokinetic basis of head-bobbing in the pigeon," *Journal of Experimental Biology*, vol. 74, pp. 187–195, 1978.

[13] T. Dekker and R. T. Cardé, "Moment-to-moment flight manoeuvres of the female yellow fever mosquito (*Aedes aegypti L.*) in response to plumes of carbon dioxide and human skin odour," *Journal of Experimental Biology*, vol. 214, pp. 3480–3494, October 2011.

[14] T. Lochmatter and A. Martinoli, "Theoretical analysis of three bio-inspired plume tracking algorithms," in *International Conference on Robotics and Automation*, 2009.

[15] J. P. Dyhr, K. A. Morgansen, T. L. Daniel, and N. J. Cowan, "Flexible strategies for flight control: an active role for the abdomen," *Journal of Experimental Biology*, vol. 216, pp. 1523–1536, 2013.

[16] B. T. Hinson, E. Rombokas, J. P. Dyhr, T. L. Daniel, and K. A. Morgansen, "Sensing from control: airframe deformation for simultaneous actuation and state estimation," in *Conference on Decision and Control*, 2013.

[17] G. W. van der Linden, A. Emami-Naeini, R. L. Kosut, H. Sedarat, and J. P. Lynch, "Optimal sensor placement for health monitoring of civil structures," in *American Control Conference*, 2011.

[18] M. Weickgenannt, S. Neuhaeuser, B. Henke, W. Sobek, and O. Sawodny, "Optimal sensor placement for state estimation of flexible shell structures," in *International Conference on Fluid Power and Mechatronics*, 2011.

[19] M. R. Safizadeh and I. Z. M. Darus, "Optimal location of sensor for active vibration control of flexible square plate," in *International Conference on Information Science, Signal Processing and Their Applications*, 2010.

[20] K.-S. Cho, J.-R. Shin, and S. H. Hyun, "Optimal placement of phasor measurement units with gps receiver," in *IEEE Power Engineering Society Winter Meeting*, 2001.

[21] D. Dua, S. Dambhare, R. K. Gajbhiye, and S. A. Soman, "Optimal multistage scheduling of PMU placement: An ILP approach," *IEEE Transactions on Power Delivery*, vol. 23, no. 4, pp. 1812 – 1820, October 2008.

[22] A. Krause, A. Singh, and C. Guestrin, "Near-optimal sensor placements in gaussian process: Theory, efficient algorithms, and empirical studies," *Journal of Machine Learning Research*, vol. 9, pp. 235–284, 2008.

[23] C. C. Castello, J. Fan, A. Davari, and R.-X. Chen, "Optimal sensor placement strategy for environmental monitoring using wireless sensor networks," in *Southeastern Symposium on System Theory*, 2010.

[24] J. Perez-Ramirez, D. K. Borah, and D. G. Voelz, "Optimal 3D landmark placements for vehicle localization using heterogeneous sensors," *IEEE Transactions on Vehicular Technology*, vol. 62, no. 7, pp. 2987–2999, 2013.

[25] D. Moreno-Salinas, A. M. Pascoal, and J. Aranda, "Optimal sensor placement for underwater positioning with uncertainty in the target location," in *International Conference on Robotics and Automation*, 2011.

[26] J. T. Isaacs, D. J. Klein, and J. P. Hespanha, "Optimal sensor placement for time difference of arrival localization," in *Conference on Decision and Control*, 2009.

[27] J. L. Crassidis and J. L. Junkins, *Optimal Estimation of Dynamic Systems*. Chapman & Hall, 2004.

[28] F. Pukelsheim, *Optimal Design of Experiments*. John Wiley & Sons, 1993.

[29] S. Boyd and L. Vandenberghe, *Convex Optimization*. Cambridge University Press, 2004.

[30] K. Yu, J. Bi, and V. Tresp, "Active learning via transductive experimental design," in *International Conference on Machine Learning*, 2006.

[31] D. Georges, "The use of observability and controllability gramians or functions for optimal sensor and actuator location in finite-dimensional systems," in *Conference on Decision and Control*, 1995.

[32] F. W. J. van den Berg, H. C. J. Hoefsloot, H. F. M. Boelens, and A. K. Smilde, "Selection of optimal sensor position in a tubular reactor using robust degree of observability criteria," *Chemical Engineering Science*, vol. 55, pp. 827–837, 2000.

[33] A. V. Wouwer, N. Point, S. Porteman, and M. Remy, "An approach to the selection of optimal sensor locations in distributed parameter systems," *Journal of Process Control*, vol. 10, no. 4, pp. 291–300, August 2000.

[34] S. Lall and J. E. Marsden, "A subspace approach to balanced truncation for model reduction of nonlinear control systems," *International Journal on Robust and Nonlinear Control*, vol. 12, pp. 519–535, 2002.

[35] J. Hahn and T. F. Edgar, "An improced method for nonlinear model reduction using balancing of empirical gramians," *Computers & Chemical Engineering*, vol. 26, pp. 1379–1397, 2002.

[36] A. K. Singh and J. Hahn, "On the use of empirical gramians for controllability and observability analysis," in *American Control Conference*, 2005.

[37] A. J. Krener and K. Ide, "Measures of unobservability," in *Conference on Decision and Control*, 2009.

[38] A. K. Singh and J. Hahn, "Determining optimal sensor locations for state and parameter estimation for stable nonlinear systems," *Industrial & Engineering Chemistry Research*, vol. 44, no. 15, pp. 5645–5659, 2005.

[39] M. Serpas, G. Hackebeil, C. Laird, and J. Hahn, "Sensor location for nonlinear dynamic systems via observability analysis and MAX-DET optimization," *Computers & Chemical Engineering*, vol. 48, pp. 105–112, 2013.

[40] L. DeVries and D. A. Paley, "Observability-based optimization for flow sensing and control of an underwater vehicle in a uniform flowfield," in *American Control Conference*, 2013.

[41] J. Berry, W. E. Hart, C. A. Phillips, J. G. Uber, and J.-P. Watson, "Sensor placement in municipal water networks with temporal integer programming models," *Journal of Water Resources Planning and Management*, vol. 132, pp. 218–224, 2006.

[42] J.-P. Watson, R. Murray, and W. E. Hart, "Formulation and optimization for drinking water contamination warning systems," *Journal of Infrastructure Systems*, vol. 15, pp. 330–339, 2009.

[43] S. Joshi and S. Boyd, "Sensor selection via convex optimization," *IEEE Transactions on Signal Processing*, vol. 57, pp. 451–462, 2009.

[44] J. M. Passerieux and D. V. Cappel, "Optimal observer maneuver for bearings-only tracking," *IEEE Transactions on Aerospace and Electronic Systems*, vol. 34, pp. 777–788, 1998.

[45] S. Martínez and F. Bullo, "Optimal sensor placement and motion coordination for target tracking," *Automatica*, vol. 42, no. 4, pp. 661–668, 2006.

[46] K. Zhou and S. I. Roumeliotis, "Optimal motion strategies for range-only constrained multisensor target tracking," *IEEE Transactions on Robotics*, vol. 24, no. 5, pp. 1168–1185, October 2008.

[47] T. L. Song, "Observability of target tracking with bearings-only measurements," *IEEE Transactions on Aerospace and Electronic Systems*, vol. 32, no. 4, pp. 1468–1472, October 1996.

[48] P. Ögren, E. Fiorelli, and N. E. Leonard, "Cooperative control of mobile sensor networks," *IEEE Transactions on Automatic Control*, vol. 49, no. 8, pp. 1292–1302, Aug. 2004.

[49] S. Liu and M. Krstic, "Stochastic source seeking for nonholonomic unicycle," *Automatica*, vol. 46, pp. 1443–1453, 2010.

[50] N. E. Leonard, D. A. Paley, F. Lekien, R. Sepulchre, D. M. Fratantoni, and R. E. Davis, "Collective motion, sensor networks, and ocean sampling," *Proceedings of the IEEE*, vol. 95, pp. 48–74, 2007.

[51] D. O. Popa, A. C. Sanderson, V. Hombal, R. J. Komerska, S. S. Mupparapu, D. R. Blidberg, and S. G. Chappel, "Optimal sampling using singular value decomposition of the parameter variance space," in *Intelligent Robots and Systems*, 2005.

[52] N. K. Yilmaz, C. Evangelinos, P. F. J. Lermusiaux, and N. M. Patrikalakis, "Path planning of AUVs for adaptive sampling using MILP," *IEEE Journal of Oceanic Engineering*, vol. 33, no. 4, pp. 522–537, Oct. 2008.

[53] D. S. Levine, "Inromation-rich path planning under general constraints using rapidly-exploring random trees," Master's thesis, Massachusetts Institute of Technology, 2010.

[54] G. A. Hollinger and G. S. Sukhatme, "Sampling-based robotic information gathering algorithms," *International Journal of Robotics Research*, vol. 33, pp. 1271–1287, 2014.

[55] M. Gautier and W. Khalil, "Exciting trajectories for the identification of base inertial parameters of robots," in *Conference on Decision and Control*, 1991.

[56] G. Venture, K. Ayusawa, and Y. Nakamura, "A numerical method for choosing motions with optimal excitation properties for identification of biped dynamics - an application to human," in *International Conference on Robotics and Automation*, 2009.

[57] F. Arrichiello, G. Antonelli, A. P. Aguiar, and A. Pascoal, "Observability metric for the relative localization of AUVs based on range and depth measurements: theory and experiments," in *IEEE/RSJ International Conference on Intelligent Robots and Systems*, 2011.

[58] B. T. Hinson, M. K. Binder, and K. A. Morgansen, "Path planning to optimize observability in a planar uniform flow field," in *American Control Conference*, 2013.

[59] J. D. Quenzer, "Obserservability based path planning in range-only localization," Master's thesis, University of Washington, 2013.

[60] H. Yu, R. Sharma, R. W. Beard, and C. N. Taylor, "Observability-based local path planning and collision avoidance for micro air vehicles using bearing-only measurements," in *American Control Conference*, 2011.

[61] M. Anguelova, "Nonlinear obserservability and identifiability: General theory and a case study of a kinetic model for *S. cerevisiae*," Ph.D. dissertation, Chalmers University of Technology and Göteborg University, 2004.

[62] R. Hermann and A. J. Krener, "Nonlinear controllability and observability," *IEEE Transactions on Automatic Control*, vol. 22, no. 5, pp. 728–740, 1977.

[63] E. D. Sontag and Y. Wang, "I/O equations for nonlinear systems and observation spaces," in *Conference on Decision and Control*, 1991.

[64] J. H. Hubbard and B. B. Hubbard, *Vector Calculus, Linear Algebra, and Differential Forms, A Unified Approach.* Prentice Hall, 1999.

[65] C.-T. Chen, *Linear System Theory and Design*, 3rd ed. Oxford University Press, 1999.

[66] G. H. Golub and C. F. V. Loan, *Matrix Computations*, 3rd ed. Baltimore: The Johns Hopkins University Press, 1996.

[67] H. P. Williams, *Model Building in Mathematical Programming.* John Wiley & Sons, 2006.

[68] B. T. Hinson and K. A. Morgansen, "Observability-based optimal sensor placement for flapping airfoil wake estimation," *AIAA Journal of Guidance, Control, and Dynamics*, vol. 37, no. 5, pp. 1477–1486, 2014.

[69] G. L. Nemhauser, L. A. Wolsey, and M. L. Fisher, "An analysis of approximations for maximizing submodular set functions," *Mathematical Programming*, vol. 14, pp. 265–294, 1978.

[70] A. Krause and C. Guestrin, "Near-optimal observation selection using submodular functions," in *National Conference on Artificial Intelligence*, 2007.

[71] F. L. Cortesi, T. H. Summers, and J. Lygeros, "Submodularity of energy related controllability metrics," in *IEEE Conference on Decision and Control*, 2014.

[72] Z. Yu, P. Cui, and S. Zhu, "Observability-based beacon configuration optimization for mars entry navigation," *AIAA Journal of Guidance, Control, and Dynamics*, 2014, AIAA Early Edition.

[73] B. H. Dickerson, Z. N. Aldworth, and T. L. Daniel, "Control of moth flight posture is mediated by wing mechanosensory feedback," *Journal of Experimental Biology*, 2014, in press.

[74] S. A. Combes and T. L. Daniel, "Into thin air: contributions of aerodynamic and inertial-elastic forces to wing bending in the hawkmoth *Manduca sexta*," *Journal of Experimental Biology*, vol. 206, pp. 2999–3006, 2003.

[75] A. L. Eberle, B. H. Dickerson, P. G. Reinhall, and T. L. Daniel, "A new twist on gyroscopic sensing: body rotations lead to torsion in flapping, flexible insect wings," *Journal of the Royal Society Interface*, 2014, in review.

[76] M. H. Dickinson and J. Palka, "Pysiological porperties, time of development, and central projection are correlated in the wing mechanoreceptors of *Drosphila*," *Journal of Neuroscience*, vol. 7, no. 12, pp. 4201–4208, 1987.

[77] R. C. Elson, "Flight motor neurone reflexes driven by strain-sensitive wing mechanoreceptors in the locust," *Journal of Comparative Physiology A*, vol. 161, no. 5, pp. 747–760, 1987.

[78] J. W. S. Pringle, "Proprioception in insects ii. the action of the campaniform sensilla on the legs," *Journal of Experimental Biology*, vol. 15, pp. 114–131, 1938.

[79] S. M. Spinola and K. M. Chapman, "Proprioceptive indentation of the campaniform sensilla of cockroach legs," *Journal of Comparative Physiology A*, vol. 96, no. 3, pp. 257–272, 1975.

[80] M. Petyt, *Introduction to Finite Element Vibration Analysis*. Cambridge University Press, 1990.

[81] T. Nakata and H. Liu, "A fluid-structure interaction model of insect flight with flexible wings," *Journal of Computational Physics*, vol. 231, pp. 1822–1847, 2012.

[82] J. Diebel. (2006) Representing attitude: Euler angles, unit quaternions, and rotation vectors.

[83] S. P. Sane and M. H. Dickinson, "The control of flight force by a flapping wing: lift and drag production," *Journal of Experimental Biology*, vol. 204, pp. 2607–2626, 2001.

[84] M. H. Dickinson, F.-O. Lehmann, and S. P. Sane, "Wing rotation and the aerodynamic basis of insect flight," *Science*, vol. 284, no. 5422, pp. 1954–1960, 1999.

[85] S. P. Sane and M. H. Dickinson, "The aerodynamic effects of wing rotation and a revised quasi-steady model of flapping flight," *Journal of Experimental Biology*, vol. 205, pp. 1087–1096, 2002.

[86] S. P. Sane, "The aerodynamics of insect flight," *Journal of Experimental Biology*, vol. 206, pp. 4191–4208, 2003.

[87] T. L. Hedrick and T. L. Daniel, "Flight control in the hawkmoth *Manduca sexta*: the inverse problem of hovering," *Journal of Experimental Biology*, vol. 209, pp. 3114–3130, 2006.

[88] M. Porez, F. Boyer, and A. Belkhiri, "A hybrid dynamic model for bio-inspired robots with soft appendages - application to a bio-inspired flexible flapping-wing micro air vehicle," in *International Conference on Robotics and Automation*, 2014.

[89] A. M. Mountcastle and T. L. Daniel, "Aerodynamic and functional consequences of wing compliance," *Experiments in Fluids*, vol. 46, no. 5, pp. 873–882, 2009.

[90] J. Katz and A. Plotkin, *Low Speed Aerodynamics*. Cambridge University Press, 2001.

[91] A. P. Willmott and C. P. Ellington, "The mechanics of flight in the hawkmoth *Manduca sexta*: I. kinematics of hovering and forward flight," *Journal of Experimental Biology*, vol. 200, pp. 2705–2722, 1997.

[92] S. A. Combes and T. L. Daniel, "Flexural stiffness in insect wings i. scaling and the influence of wing venation," *Journal of Experimental Biology*, vol. 206, pp. 2979–2987, 2003.

[93] T. Nakata and H. Liu, "Aerodynamic performance of a hovering hawkmoth with flexible wings: A computational approach," *Proceedings of the Royal Society B*, vol. 279, pp. 722–731, 2012.

[94] M. H. Dickinson, "Directional sensitivity and mechanical coupling dynamics of campaniform sensilla during chordwise deformations of the fly wing," *Journal of Experimental Biology*, vol. 169, pp. 221–233, 1992.

[95] M. Grant and S. Boyd, "Graph implementations for nonsmooth convex programs," in *Recent Advances in Learning and Control*, ser. Lecture Notes in Control and Information Sciences, V. Blondel, S. Boyd, and H. Kimura, Eds. Springer-Verlag Limited, 2008, pp. 95–110.

[96] ——, "CVX: Matlab software for disciplined convex programming, version 2.0 beta," http://cvxr.com/cvx, Sep. 2012.

[97] M. H. Dickinson, "Comparison of encoding properties of campaniform sensilla on the fly wing," *Journal of Experimental Biology*, vol. 161, pp. 245–261, 1990.

[98] S. P. Sane and M. J. McHenry, "The biomechanics of sensory organs," *Integrative and Comparative Biology*, vol. 49, no. 6, pp. 8–23, 2009.

[99] T. McGeer and J. Vagners, "Historic crossing: an unmanned aircraft's Atlantic flight," *GPS World*, vol. 10, no. 2, pp. 24–30, Feb. 1999.

[100] B. T. Hinson and K. A. Morgansen, "Observability optimization for the nonholonomic integrator," in *American Control Conference*, 2013.

[101] R. W. Brockett, "Control theory and singular riemannian geometry," in *New Directions in Applied Mathematics*, P. J. Hilton and G. S. Young, Eds. Springer, 1981, pp. 11–27.

[102] R. M. Murray and S. S. Sastry, "Nonholonomic motion planning: Steering using sinusoids," *IEEE Transactions on Automatic Control*, vol. 38, no. 5, pp. 700–716, May 1993.

[103] D. E. Kirk, *Optimal Control Theory, An Introduction*. Dover, 2004.

[104] E. D. Andersen and K. D. Andersen, "MOSEK: High performance software for large-scale LP, QP, SOCP, SDP and MIP," www.mosek.com, Mar. 2013, version 7.0.